The Dissertation Committee for Weicheng Lai Certifies that this is the approved version of the following dissertation:

On-Chip Photonic Crystal Waveguide for Chemical and Biological Sensing

Committee:

Ray T. Chen, Supervisor

Paul S. Ho

John X.J. Zhang

Zheng Wang

Guo-Dung Su

Swapnajit Chakravarty

On-Chip Photonic Crystal Waveguide for Chemical and Biological Sensing

by

Weicheng Lai, B.S.; M.S.

Dissertation

Presented to the Faculty of the Graduate School of

The University of Texas at Austin

in Partial Fulfillment

of the Requirements

for the Degree of

Doctor of Philosophy

The University of Texas at Austin

December 2013

Dedicated to my wife and my parents

Acknowledgements

I would like to thank my advisor, Dr. Ray T. Chen, for his continuous support and guidance in my doctoral study. Without his guidance and support, I would not be able to finish my research and study in the University of Texas at Austin smoothly. I always appreciate that he provided the admission for me to his research group and his advice for my research. I am also thankful for my committee members, Dr. Paul S. Ho, Dr. John X.J. Zhang, Dr. Zheng Wang, Dr. Guo-Dung Su, and Dr. Swapnajit Chakravarty for serving on my committee and advice on my dissertation.

I appreciate the help from members of Optical Interconnect Group at the University of Texas at Austin, particularly for the colleagues who joined this group in the same year as me and who work in the sensor projects . I am thankful for their help in cleanroom in Microelectronics Research Center and testing lab, therefore we were able to achieve the goals of our projects. I also want to thank Dr. Swapnajit Chakravarty for the help over the years.

Finally, I would like to express my gratitude to my wife, Hsuan Hua Huang and my parents, Hsing-Hui Lai and Hui-Yu Huang for their love and support throughout my life. Without their love and support, I would not be able to finish my work and be a person who I am now. I will always remember the moments that my family supports me.

Weicheng Lai

The University of Texas at Austin

Austin, TX

On-Chip Photonic Crystal Waveguide for Chemical and Biological Sensing

Weicheng Lai, Ph.D

The University of Texas at Austin, 2013

Supervisor: Ray T. Chen

Photonic crystal waveguide (PCW) based device has been used in many applications in recent years due to its unique slow light effect. In this work, the application of PCW on sensing is presented. First, we present a PCW structure based Infrared (IR) spectroscopy combining with slot structure which has a large electric field enhancement for light-matter interaction for chemical sensing. The slow light effect and the electric field enhancement of our designed structure greatly enhance the absorption factor of chemical analytes by 1000. We then use multimode interference (MMI) optical splitter and Y junction combiner to connect two PCWs to show multiplexed detections of two chemicals on a single chip. Our results show the detection is down to 1 ppb for xylene in water and 100ppm for methane in nitrogen. We also present PCW microcavities structure for biological sensing in our work. Due to its high quality factor and easier immobilization of biomaterials, we are able to use ink jet printing method to bind the biomaterials on top of our chip. We choose linear-type 13 (L13, missing 13 holes) microcavities to do the biosensing for antibodies and cancer cell lysates because of its higher sensitivity combining with slow light effect. Our work achieves the cancer cell lysates detection down to 2 cells/μl., and further applications will be presented in our group in the future.

Table of Contents

List of Tables

List of Figures

Chapter 1: Introduction and Research Goals

Photonic crystal based sensors have been more and more promising in recent years due to its advantages of using optical method and high sensitivity for chemical analytes and biomaterials. In this dissertation, we are presenting several photonic crystal sensors based projects that were done in these four years. The design, fabrication, and experimental results of photonic crystal (PC) slot waveguide for liquid chemical sensing and gaseous chemical sensing are discussed here. In addition, the photonic crystal microcavities structure is also used to discuss about sensing for bio-molecules.

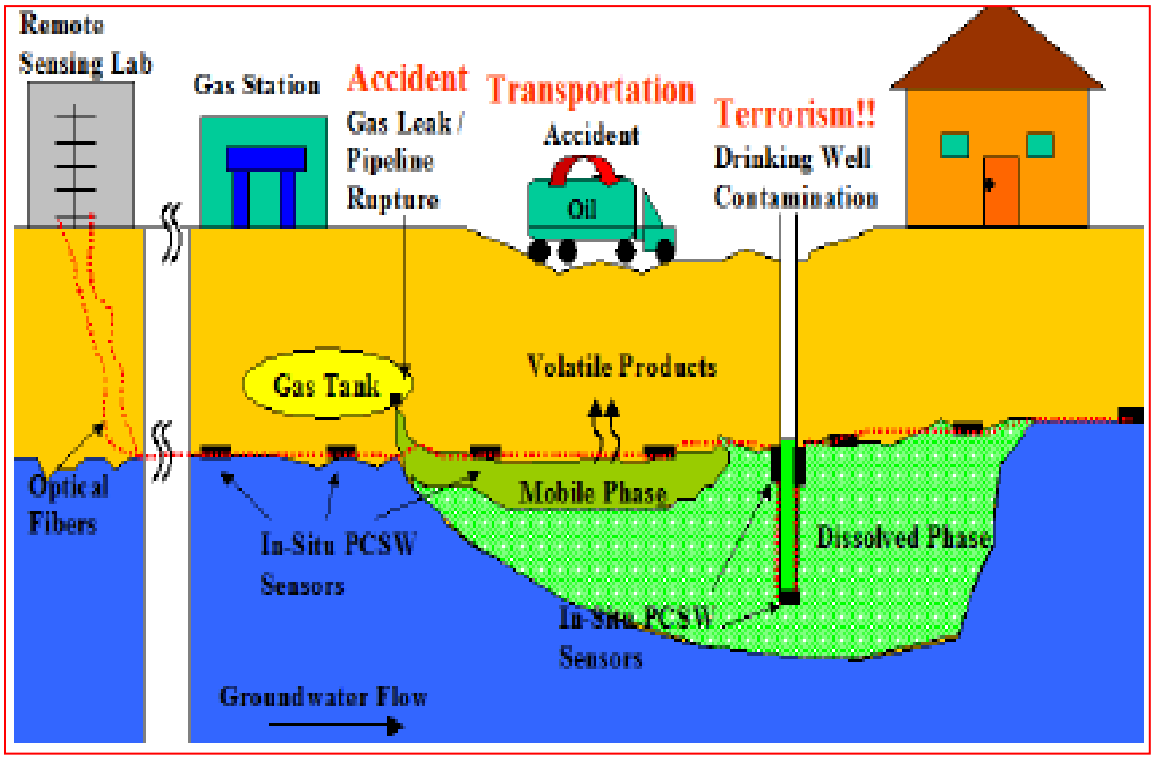

Figure 1.1: Schemetic image of photonic crystal sensor for chemical analytes detection

In Figure 1.1, the schematic image of photonic crystal waveguide (PCW) for chemical sensing is shown. The goal of chemical sensing projects is using a remote controlling PCW sensor by optical fiber to detect the VOCs without exposing the engineers in these toxic environments. The sensors are located near underground water in order to detect the VOCs in water and potential natural gas leakage.

Chapter 2 and 3 will demonstrate the photonic crystal slot waveguide application on the sensing of volatile organic compounds (VOCs) in water and in air which are funded by National Science Foundation (NSF) and Environmental Protection Agency (EPA). We take xylene in water and methane in nitrogen as our VOC detection materials. For these two projects, infrared (IR) absorption spectroscopy is the principle method and it is widely used as a simple and reliable technique for detection and identification of hazardous underground water and greenhouse gases in the atmosphere. IR spectroscopy relies on fundamental molecular vibrations, which makes the technique very attractive for sensing and identification compared to other methods. Various methods such as cavity ring-down spectroscopy (CRDS) [1], tunable diode laser absorption spectroscopy (TDLAS) [2] and Fourier transform infrared spectroscopy [3] that detect gases through spectroscopic signatures are available commercially. Except a handheld TDLAS methane sensor [4], most commercial IR spectrometers are large, heavy table-top instruments consuming few tens to hundreds of Watts of power. Above characteristics make the instruments expensive and unsuitable for portable and distributed sensing applications. Thus, a lab-on-chip IR absorption spectrometer is thus highly desirable.

Our photonic crystal slot waveguide structure combines with electric field enhancement of slot structure and slow light effect of photonic crystal waveguide to efficiently increase light-matter interaction with chemical analytes and also increase the absorption of analytes in water and in air. Thus, by using the successfully demonstrated device structures as in chapter 2 and 3, we further integrate the photonic crystal slot devices with multimode interference (MMI) optical power splitter and optical Y junction combiner to become a 1x2 multiplexed device to detect two different chemicals on a single chip in chapter 4 and this concludes the chemical sensing section of the dissertation.

According to Beer-Lambert law, transmitted intensity I is given by:

$$I = I_0 \exp(-\gamma \alpha L) \quad (1)$$

,where I_0 is the incident intensity, α is the absorption coefficient of the medium, L is the interaction length and γ is the medium-specific absorption factor determined by dispersion enhanced light-matter interaction. In conventional free-space systems, $\gamma = 1$; thus L must be large to achieve a suitable sensitivity of measured I/I_0. Although various complex schemes have been demonstrated to increase absorption path lengths, present state-of-the-art dimensions are still significantly large to be accommodated on a semiconductor chip.

For lab-on-chip systems, L must be small, hence γ must be large. Mortensen et al showed [5] using perturbation theory that

$$\gamma = f \times \frac{c/n}{v_g} \quad (2)$$

,where c is velocity of light in free space, v_g is group velocity in medium of effective index n and f is filling factor denoting relative fraction of optical field residing in analyte medium. Equation 2 shows that slow light propagation (small v_g) significantly enhances absorption. Furthermore, greater the electric field overlap with analyte, greater the effective absorption by the medium. Both conditions of small v_g and high f are fulfilled in a photonic crystal slot waveguide.

Next, we present our photonic crystal structure on biosensing in chapter 5-7. As in Figure 1.2 shows, we intentionally take out three holes on a photonic crystal waveguide to become a linear L3 microcavity. Each microcavity has a specific resonance toward specific wavelength, thus we detect several resonance dips at output spectrum. The goal of our biosensing projects is to investigate the possibility to detect multiple biomaterials on a single biochip. For instance, we use four different L3 microcavities structure in Figure 1.2, thus we are able to detect four different biomaterials if we immobilize four different biomaterials (antibodies, cells, or antigens).

We start with the theoretical and experimental results for the enhancement of slow light effect on photonic crystal microcavities structure devices to further identify the interested resonance mode with higher sensitivity in chapter 5. We analyze whether the different resonance mode with different group index affects biosensitivity, which shows how slow light effect affects the sensitivity to detect biomaterials. With all the details of

the results we got in this chapter, we choose the resonance mode with higher sensitivity and larger slow light effect to do the sensing for biomaterials.

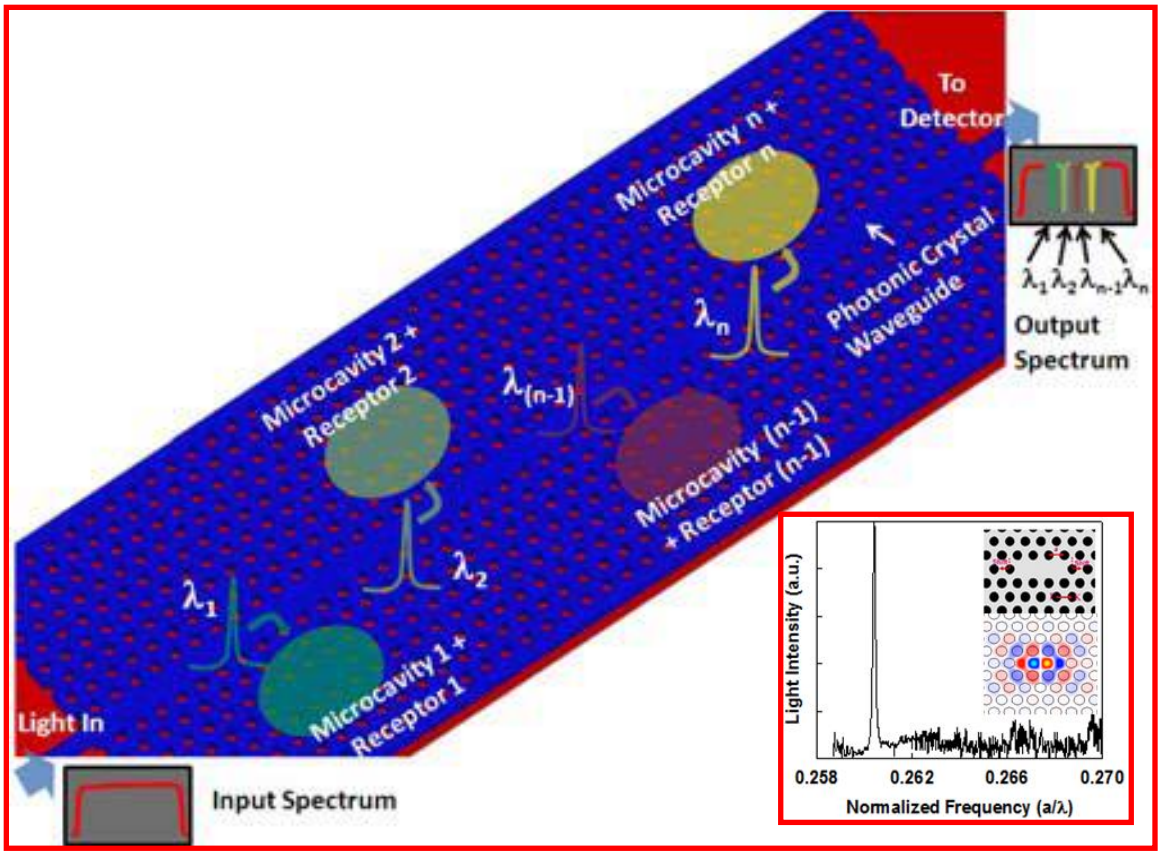

Figure 1.2: Photonic crystal microcavities structure shows four cavities on photonic crystal waveguide. Each microcavity shows specific resonance dip at the output spectrum. Inset shows the resonance of microcavity has a high quality factor.

In chapter 6 and 7, the photonic crystal microcavity structure is presented as a biological sensing structure for antibodies and cancer cells which is funded by National Cancer Institute (NCI). First, we will discuss several linear type (L-type) photonic crystal

microcavity structures dependence on quality factor (Q) and sensitivity for biological sensing. Linear type L13 microcavity structure is chosen to detect the biomolecules and cancer cell lysates due to its higher sensitivity and high quality factor. In chapter 7, we will discuss more about the cancer cell lysate sensing based on L13 type PC microcavity structure described in chapter 6, and then we will discuss the sandwiched assay structure which provides amplified sensing for cancer cell lysates by using L13 PC microcavities. In the last chapter of the dissertation, I will summarize the chemical and biological sensing in our group.

REFERENCES

[1] M.J. Thorpe, K.D. Moll, R.J. Jones, B. Safdi, and J.Ye, Science 311, 1595 (2006) , URL: http://www.tigeroptics.com/

[2] M. Lackner, Rev. in Chem. Engg. 23, 65 (2007).

[3] F. Adler, P. Maslowski, A. Foltynowicz, K.C. Cossel, T.C. Briles, I. Hartl, and J. Ye, Opt. Express 18, 21861 (2010).

[4] URL: http://www.tdlas.com/products/

[5] N.A. Mortensen, S.S. Xiao, Appl. Phys. Lett 90(14), 141108 (2007).

Chapter 2: Photonic Crystal Slot Waveguide for Volatile Organic Compounds in Water: Xylene in Water

2.1 INTRODUCTION

A simple and reliable technique for detection and identification of toxic volatile organic contaminants (VOC) in water is infrared absorption spectroscopy. Infrared spectroscopy relies on fundamental molecular vibrations and does not require costly analyte labeling, which makes the technique very attractive for sensing and identification compared to other methods. Commercial infrared spectrometers are large, heavy and expensive. A lab-on-chip infrared absorption spectrometer is thus highly desirable for portable and distributed sensing applications. In this chapter, we will discuss the application of photonic crystal slot waveguide on xylene in water and the principle is based on Beer-Lambert law and perturbation theory [1].

During the past two decades, photonic crystal devices have attracted significant interest due to their unique dispersive properties that allow control and manipulation of light-matter interactions on length scales of the wavelength of light [2, 3]. Various miniature applications have been demonstrated for light emission [4, 5], cavity quantum electrodynamics [6] and electro-optical modulation [7]. Photonic crystal (PC) devices have shown significant promise in sensing applications due to high sensitivity to refractive index changes of the ambient [8-10]. The change in refractive index of a medium caused by an analyte is however not analyte-specific and is therefore not a unique signature of the analyte. In contrast, absorption spectrum of an analyte is a label-free signature based on analyte-specific molecular vibrations and thus identifies the

analyte uniquely. In this chapter, we demonstrate a PC slot waveguide that enables on-chip optical absorption spectroscopy. We demonstrate near-infrared spectroscopy of xylene in water as a representative contaminant and also due to its environmental and human health significance.

PC waveguides have demonstrated group velocity slow-down factors ~100 [11]. Slot waveguides have also demonstrated significant increase in the electric field intensity in a narrow low index slot in a high index ridge waveguide, by at least a factor of 10. Slow light in PC waveguides coupled with electric field intensity enhancement in a slot in the PC waveguide, can therefore reduce v_g and enhance f, thereby theoretically shrinking the required absorption path length by a factor of 1000, to lab-on-chip scales.

2.2 DEVICE STRUCTURE

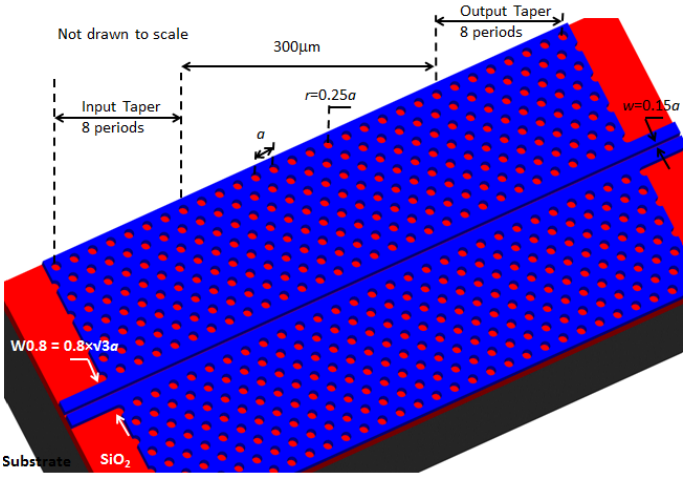

Fig. 2.1(a)

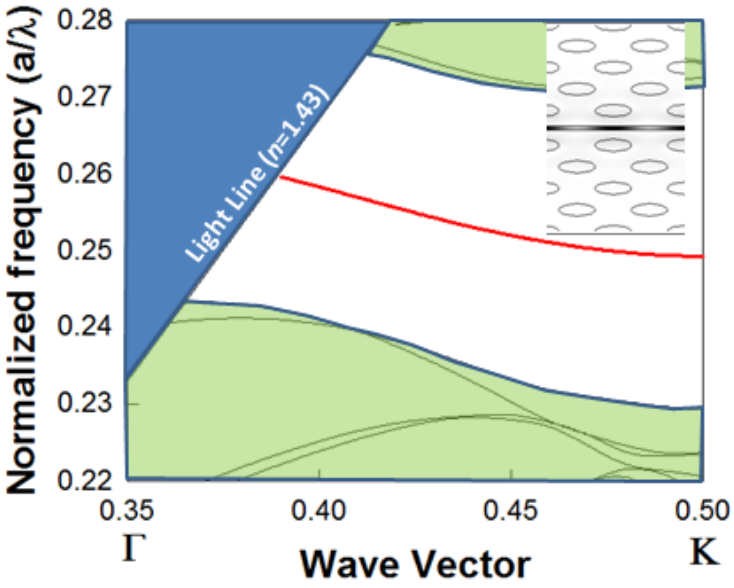

Fig. 2.1(b)

Figure 2.1: (a) Schematic of photonic crystal slot waveguide device showing different regions (b) Dispersion diagram of photonic crystal slot waveguide device coated with PDMS sensing phase. Single mode guided below light line is shown in red and mode profile shown in inset.

Schematic of our silicon PC slot waveguide device is shown in Fig. 2.1(a). The PC waveguide is a W0.8 line defect waveguide with uniform lattice constant a, where W0.8 denotes that width of PC waveguide is $0.8\times \sqrt{3}a$. A slot with width w=0.15a is etched at the center of the PC waveguide. Silicon slab thickness and air hole diameter are h=0.52a and d=0.5a. The device is coated with thin ~8μm film of poly-dimethyl siloxane (PDMS). PDMS is hydrophobic; hence use of PDMS ensures that absorption signatures of xylene are obtained without interference from strong near-infrared absorption of water. PDMS cladding thickness chosen avoids interaction between the guided optical mode in the slot and water ambient. The dispersion relation (photonic band diagram) of defect-guided mode is calculated using three-dimensional (3D) plane-wave expansion method in Fig. 2.1(b). Design parameters of W0.8 PC slot waveguide are chosen to support a single PC waveguide slot guided mode. Mode profile of guided slot mode is shown in the inset. Light is guided into and out of a 300μm long PC slot waveguide by ridge waveguides using PC impedance taper where holes adjacent to PC slot waveguide are shifted in steps by 0.0025a over 16 periods. Impedance taper enables gradual change in group index that allows higher coupling efficiency into slow light guided mode [12].

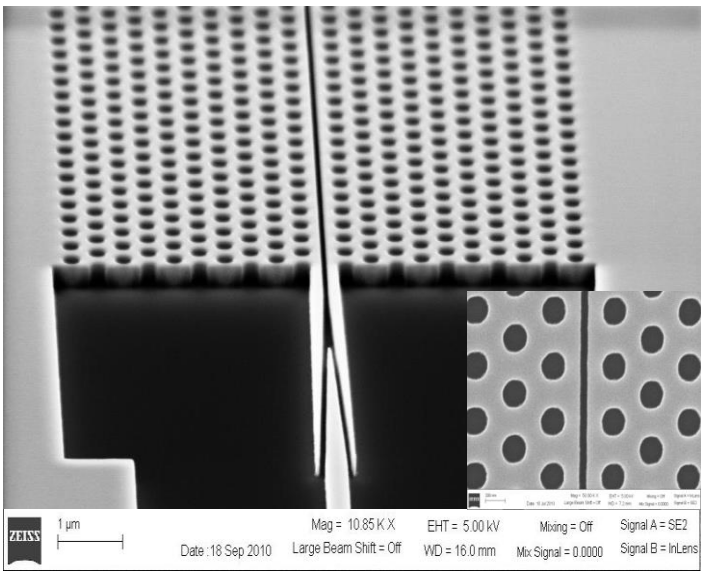

Figure 2.2: Scanning electron micrograph (SEM) image of fabricated W0.8 photonic crystal slot waveguide device, before PDMS deposition, showing input mode converter and etched photonic crystal pattern. Magnified top view of pattern is shown in inset.

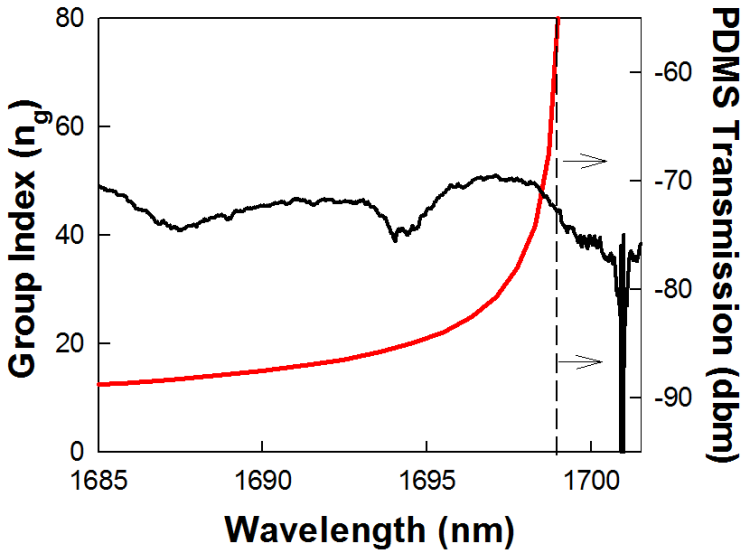

Figure 2.3: (left scale) Group index vs. wavelength (red curve) as designed with band edge at 1698nm (dotted black line). (right scale) Experimental transmission spectrum (black curve) in PDMS infiltrated slotted photonic crystal waveguide (without analyte), showing band edge shifted in fabricated device to 1701nm.

Devices were fabricated on silicon-on-insulator (SOI) wafer with 230nm top silicon layer and 3μm buried oxide as in Figure 2.4. In Figure 2.4(a), 45nm thermal oxide was grown on top of silicon as etch mask for pattern transfer. PC slot waveguides, tapers, and strip waveguides are patterned in one step with e-beam lithography as in Figure 2.4(b) followed by reactive ion etching in Figure 2.4(c-d). Scanning electron micrograph (SEM) of fabricated structure is shown in Fig 2.2. PDMS top cladding was prepared by spinning a 10:1 mixture of Sylgard Elastomer 184 from Dow Corning (refractive index n=1.43) and curing agent, followed by oven-baking. While electric field enhancement by slot is nearly constant across entire bandwidth of guided mode, as observed in the group index simulation in Fig. 2.3, slow light effects exist over a bandwidth ~20nm. To derive maximum slow light enhancement while also taking into account coupling efficiencies from ridge waveguide into slow light mode due to group velocity mismatch and losses that occur at low group velocities, design parameters are chosen so that group index n_g of guided mode is ~40 at individual xylene absorbance maxima in near-infrared. Absorption signature of xylene in near-infrared extends from 1665nm to 1745nm with absorption peaks at 1674nm, 1697nm and 1720nm respectively [13]. Three lattice constants a=455nm, 458nm and 460nm are selected for three devices so that slow light propagation occurs at individual absorbance maxima.

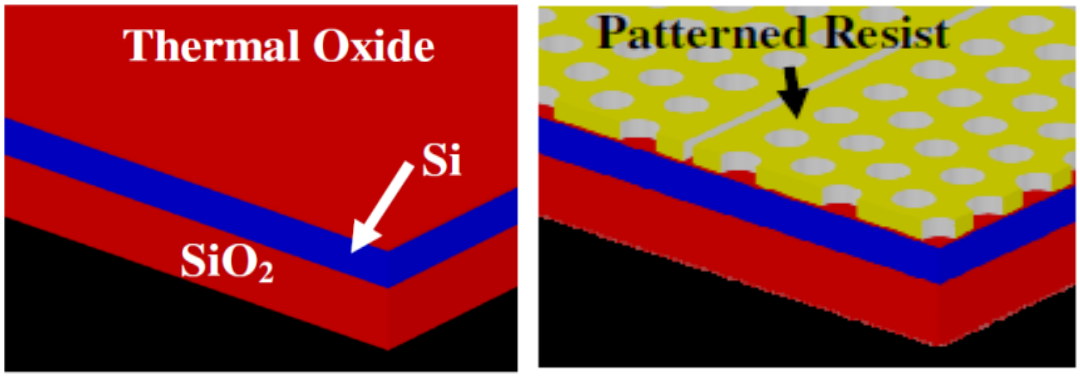

(a) Thermal Oxidation (b) E beam patterned resist

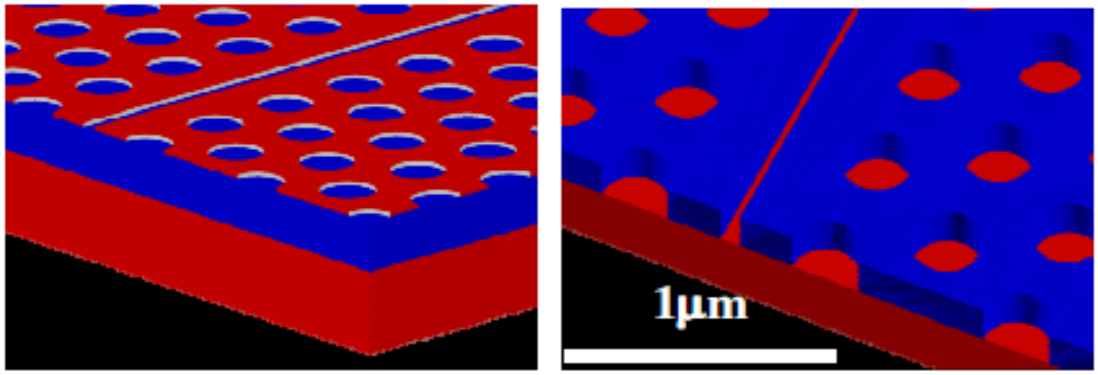

(c) Silicon dioxide etching (d) Transfer pattern to silicon layer

Figure 2.4: (a)-(d) Fabrication steps for PC slot waveguide

2.3 Measurement Results

Devices were tested on a Newport six-axis auto-aligning station in Figure 2.5. Input light from a broadband source (SuperK Versa from NKT Photonics) was TE-polarized and butt-coupled to / from the device with polarization maintaining single mode tapered

lensed fiber with mode field diameter ~3μm. Experimental transmission spectrum through PDMS filled slot in absence of analyte in Figure 2.3 shows that the band edge is red-shifted ~3nm from design (dotted black line). Sample solutions were prepared by transferring 200μl of xylene into a sealed beaker with 200ml of deionized (DI) water, followed by continuous stirring for 12 hrs at room temperature, as described in ref. [14]. Transmitted light was analyzed with an optical spectrum analyzer, in presence and absence of xylene in water.

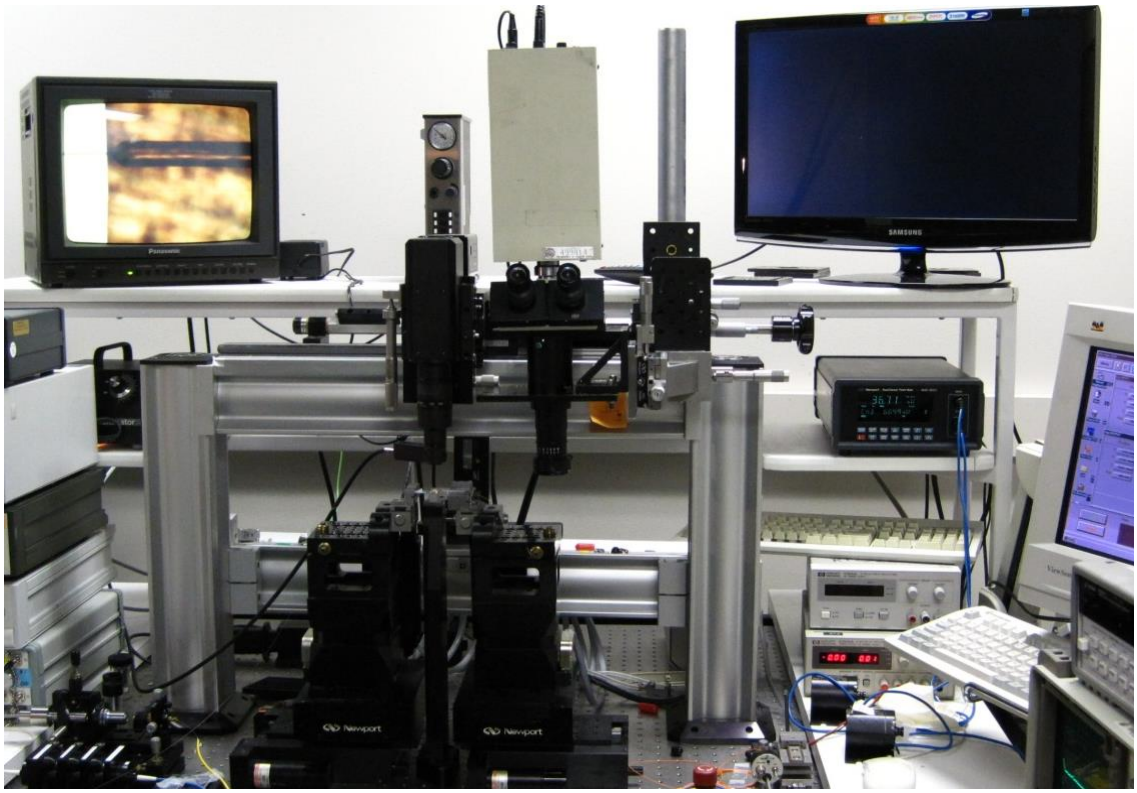

Figure 2.5: Six-axis auto-aligning system for measurement

Since PDMS is very thin, response time is a few seconds. Measurements are performed immediately after analyte introduction. Difference in transmitted intensity

through PDMS clad PC slot waveguide is calculated in presence and absence of xylene and absorbance of xylene determined. Measurements are performed for all three lattice constants. Theoretical spectrum of xylene [13] is shown in Fig. 2.6. The spectrum was divided into 3 sections shown by dotted green lines. Experimentally obtained xylene spectrum is shown for each section, corresponding to individual lattice constants, in insets of Fig. 2.6. Good correspondence is observed between experimentally observed absorption peaks and theoretical spectrum.

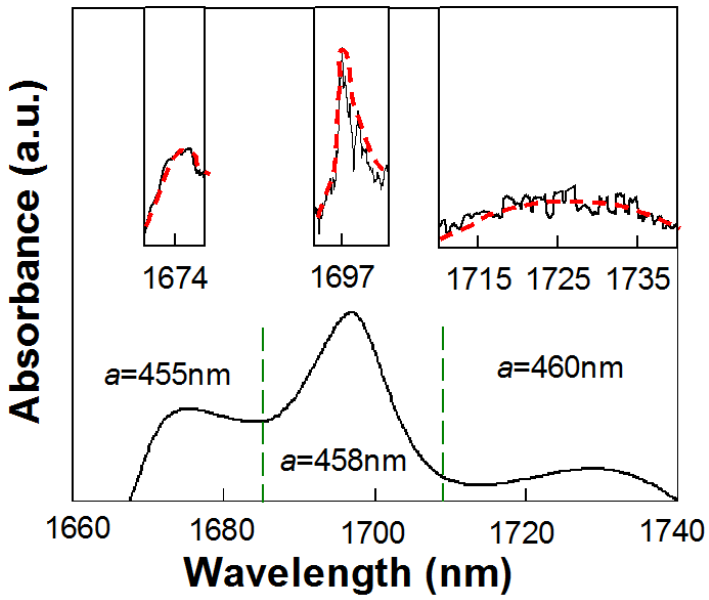

Figure 2.6: Theoretical spectrum of xylene obtained from ref. [13] divided into 3 regions as shown by dotted lines. Experimental transmission spectrum centered on absorbance maxima in each section is plotted in respective insets for 100ppm (v/v) concentration.

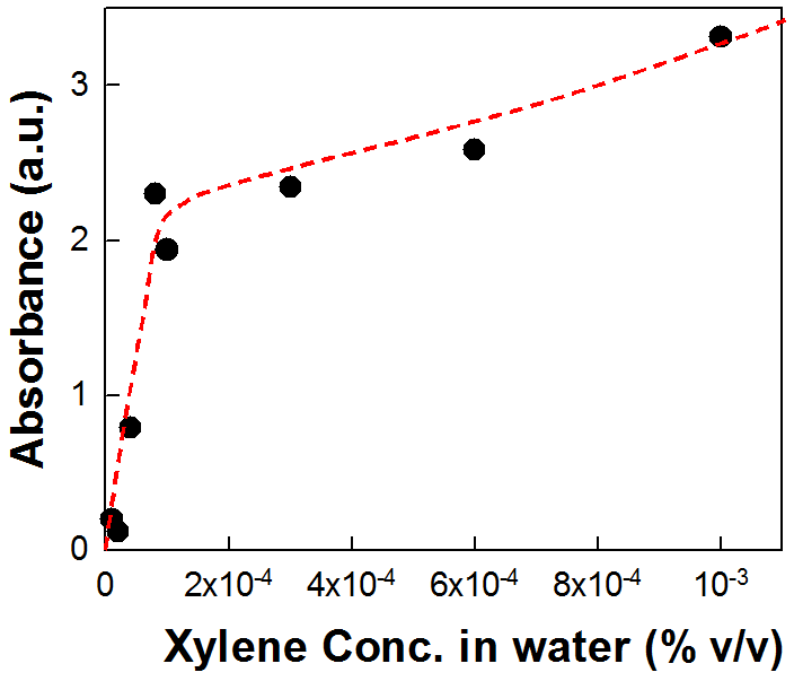

Figure 2.7: Absorbance magnitude vs. xylene concentration in water (%v/v).

To determine detection limit, xylene concentration in DI water was varied from 10^{-5}% or 100ppb (v/v) to 1% by volume. Intensity of the strongest absorbance peak at 1697nm is plotted in Fig. 5 as a function of xylene concentration in water. Fig. 2.7 shows that Beer-Lambert law is followed linearly between 100ppb (v/v) to ~1ppm (v/v); at higher concentrations, absorbance curve deviates from linearity. Detection limit 100ppb (v/v) [~86μg/L] demonstrated in our 300μm long device is lower than near infrared detection limits observed with PDMS disks in water (3mg/L) [14]. The device is more sensitive than methods which require pre-processing for salinity to enhance sensitivity [15]. Our device is more than an order of magnitude smaller in length than PDMS disks above. Detection limit of our device is better than 400μg/L demonstrated with 11meter

optical fibers [16]. Also, response time in our device is a few seconds compared to ~60 minutes [15] due to small PDMS thickness for xylene to diffuse. We believe at the lower end, sensitivity is limited by offset of absorbance peak to ~ n_g=20 due to fabrication errors, as shown in Fig. 2.3. Detection limit can be enhanced by at least a factor of 3 in current devices in near-infrared by better control of fabrication that positions the band edge closer to peak absorbance as designed. It must be noted, in mid- infrared, 20μg/L (v/v) detection limit was demonstrated with 50mm long sample cells [17]. The PC slot waveguide device, based on Maxwell's equations, is readily scalable to mid-infrared. Since xylene has ~2 orders larger absorption cross-section in mid infrared, few hundred ppt detection limits are possible in PC slot waveguide devices on 300μm length scales at longer wavelength.

2.4 SUMMARY

In summary, we demonstrated a 300μm long on-chip silicon PC slot waveguide absorption spectrometer that combines slow light with electric field enhancement to achieve near infrared absorption spectroscopy of xylene in water with detection limit 86μg/L. Remote monitoring is enabled by optical fibers; our device is five times more sensitive for xylene in water than existing state-of-the-art devices in near-infrared on more than an order of magnitude smaller length scale.

2.5 REFERENCES

[1] N.A. Mortensen, S.S. Xiao, Appl. Phys. Lett., 90(14), 141108 (2007).

[2] E. Yablonovitch, Phys. Rev. Lett., 58, 1059 (1987).

[3] S. John, Phys. Rev. Lett., 58, 2486 (1987).

[4] S.Chakravarty, P.Bhattacharya, and Z.Mi, IEEE Photon. Tech. Lett., 18, 2665 (2006).

[5] O. Painter, R.K. Lee, A. Scherer, A. Yariv, J.D. O'Brien, P.D. Dapkus, and I. Kim, Science, 284 (5421), 1819 (1999).

[6] J. Vuckovic, and Y. Yamamoto, Appl. Phys. Lett. ,82 (15), 2374 (2003).

[7] C-Y. Lin, X. Wang, S. Chakravarty, B-S. Lee, W-C. Lai, J. Luo, A. K-Y. Jen, and R.T. Chen, Appl. Phys. Lett., 97, 093304 (2010).

[8] S.Chakravarty, J.Topoľančik, P.Bhattacharya, S.Chakrabarti, Y. Kang, and M.E. Meyerhoff, Opt. Lett., 30, 2578 (2005).

[9] M. Loncar, A. Scherer, and Y.M. Qiu, Appl. Phys. Lett., 82 (26), 4648 (2003).

[10] M.R. Lee, and P.M. Fauchet, Optics Lett., 32 (22), 3284 (2007).

[11] M. Notomi, Phys. Rev. Lett., 87, 253902 (2001).

[12] A. Wang, S. Chakravarty, B-S. Lee, C. Lin, and R.T. Chen, Opt. Lett., 34(20), 3202 (2009).

[13] D.A. Burns, "Handbook of near-infrared analysis," 3rd Edition, Hoboken: Taylor and Francis Ltd (2007).

[14] J.S. Albuquerque, M.F. Pimentel, V.L. Silva, M. Raimundo, J.J.R. Rohwedder, and C. Pasquini, Anal. Chem., 77 (1), 72 (2005).

[15] K.M.G. Lima, I.M. Raimundo, and M.F. Pimentel, Sens. & Act. B-Chem., 125(1), 229 (2007).

[16] J. Burck, S. Roth, K. Kraemer, M. Scholz, N. Klaas, J. Hazard. Mater., 83, 11 (2001)

[17] A.M.F. Silva, M.F. Pimentel, I.M. Raimundo, and Y.M.B. Almeida, Vibration. Spectros., 46 (1), 39 (2008).

Chapter 3: Photonic Crystal Slot Waveguide for Gaseous Volatile Organic Compounds: Methane in Water

3.1 INTRODUCTION

The principle of IR absorption spectroscopy for gaseous volatile organic compounds detection is also based on Beer-Lambert law. According to this law, transmitted intensity I is given by:

$$I = I_0 \times \exp(-\gamma \alpha L) \quad (1)$$

where I_0 is the incident light intensity, α is the absorption coefficient of the analyte medium, L is optical interaction length and γ is the medium-specific absorption factor that is determined by dispersion enhanced light-matter interaction. In conventional free-space systems, $\gamma = 1$; hence L must be large to achieve a suitable sensitivity of measured I/I_0. For lab-on-chip systems, L must be small, hence γ must be large. Using perturbation theory [1], it can be shown that

$$\gamma = f \times \frac{c/n}{v_g} \quad (2)$$

where c is the velocity of light, v_g is the group velocity in the analyte of effective index n and f is the fill factor which denotes the relative fraction of optical field that resides in the analyte. Equation 2 shows that slow light propagation (small v_g) significantly enhances absorption. Furthermore, the greater the electric field overlap with the analyte, the greater

the effective absorption by the medium. Both features of small v_g and high f are satisfied in a photonic crystal slot waveguide. Photonic crystal (PC) devices have unique dispersive properties that allow control and manipulation of light-matter interactions on length scales of the wavelength of light [2]. PC devices have been demonstrated for light emission [3], sensing [4], and electro-optical modulation [5] amongst various applications.

PC waveguides have demonstrated group velocity slow-down factors ~100 [6]. Slot waveguides have also demonstrated significant increase in the electric field intensity in a narrow low index slot in a high index ridge waveguide, by at least a factor of 10 [7]. Slow light in PC waveguides coupled with electric field intensity enhancement in a slot in the PC waveguide, can thus reduce v_g and enhance f, thereby theoretically shrinking absorption path length by a factor of 1000, an order of magnitude greater than ring resonator devices [8]. We previously demonstrated near-IR spectroscopy of xylene in water ambient [9] with a PC slot waveguide. Here, we demonstrate a PC slot waveguide for on-chip near-IR absorption spectroscopy of methane, a typical greenhouse gas.

3.2 DEVICE STRUCTURE

Schematic of our silicon PC slot waveguide device is shown in Figure 3.1(a). The PC waveguide is a W1.3 line defect with uniform lattice constant a, and width $1.3\times \sqrt{3}a$. Device parameters are shown in Figure 3.1(a). Dispersion relation of the defect-guided mode is calculated using three-dimensional plane-wave expansion method in Figure 3.1(b). In contrast to a fragile free-standing silicon platform, we choose a silicon-on-insulator (SOI) platform that provides more mechanical stability. Three modes labeled 1, 2 and 3 are observed in the photonic band gap (PBG). Mode profiles are shown in insets to Figure 3.1(b). Modes 1 and 3 are slot guided modes. However, only mode 3 propagates below the light line for silicon dioxide, without any overlap with modes above the light line. Mode 2 resides primarily in the dielectric and air holes, hence interacts less with analyte filing the slot. Design parameters of W1.3 PC slot waveguide are thus chosen corresponding to Mode 3. Light is guided in and out of PC slot waveguide by ridge waveguides using PC impedance taper for higher coupling efficiency into the slow light mode, where holes adjacent to the PC slot waveguide are shifted in steps by $0.00125\times\sqrt{3}a$ over 16 periods. [10].

(a)

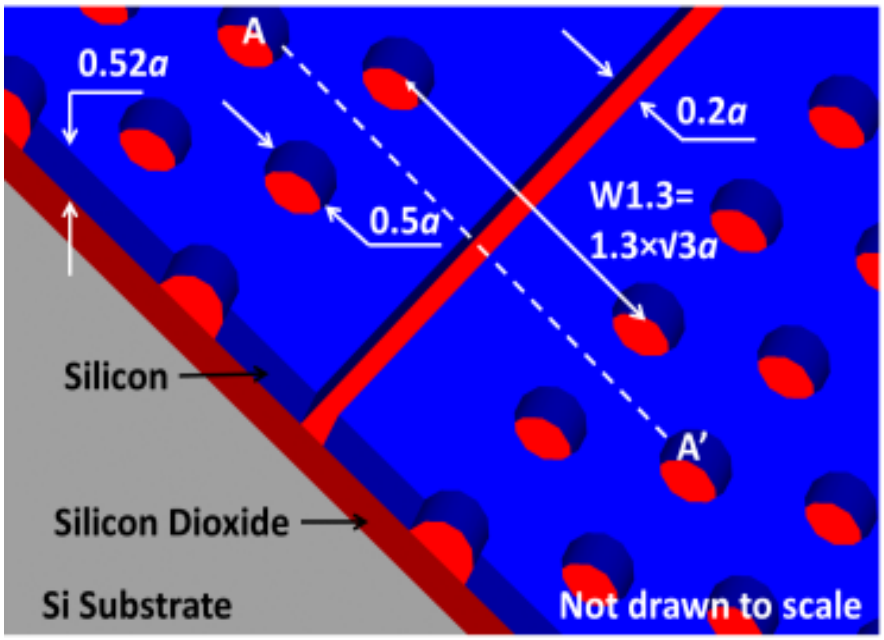

(b)

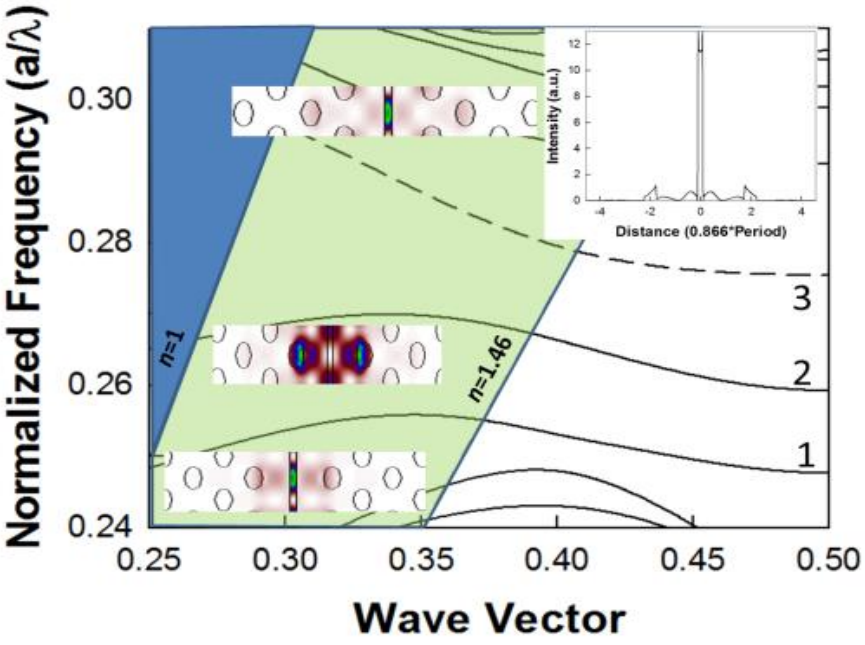

Figure 3.1: (a) Schematic of PC slot waveguide device showing different regions, a denotes lattice constant (b) Dispersion diagram of PC slot waveguide showing different modes. (Insets) show mode profiles of modes 1, 2 and 3 across axis A-A' in (a). Electric field enhancement magnitude as a function of position for mode 3 across axis A-A' is shown.

Device fabrication on SOI wafer follows standard steps described in detail elsewhere [7, 10-11]. Scanning electron micrograph (SEM) of the fabricated structure is shown in Figure 3.2. While electric field enhancement by the slot is nearly constant across entire bandwidth of the guided mode, as observed in the group index simulation in Figure 3.3, slow light effects decrease rapidly from the band edge reaching n_g=30 about 5nm from the band edge.

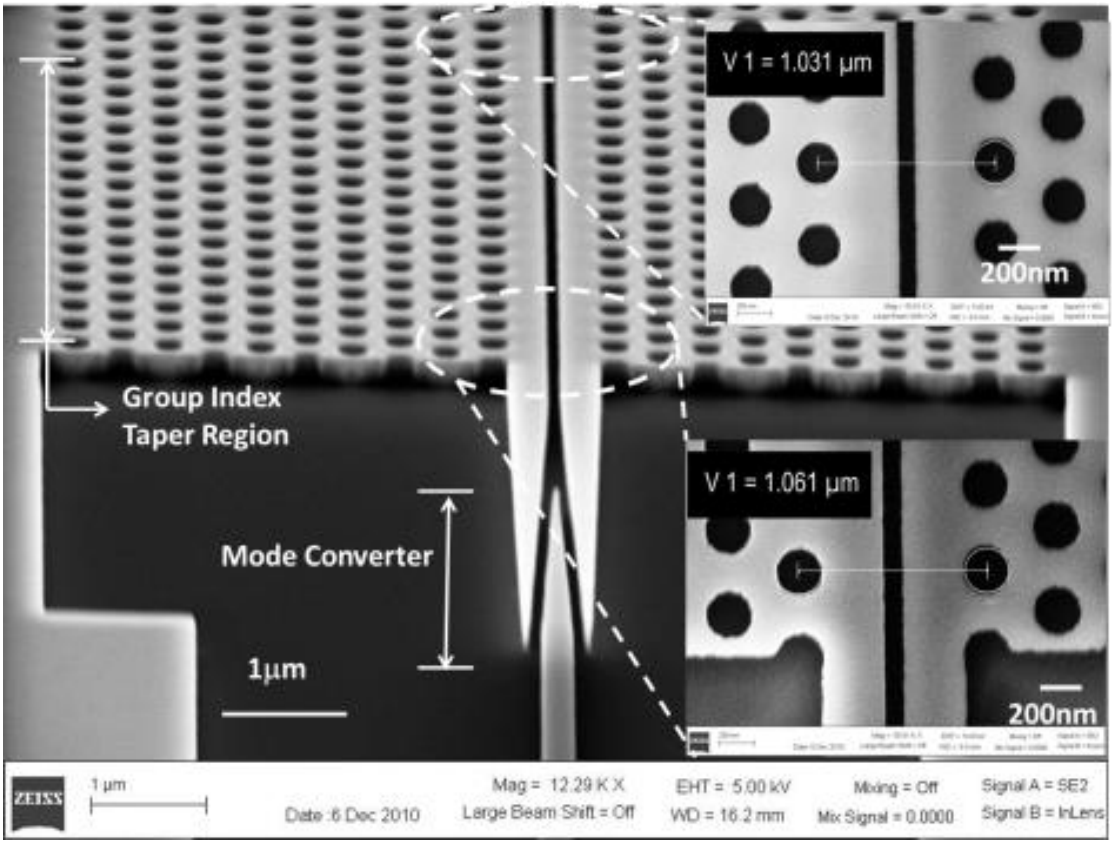

Figure 3.2: SEM image of fabricated W1.3 PC slot waveguide device, showing input mode converter, input group index taper and etched PC pattern. Insets show distance between air holes on two sides of the slot at the beginning and the end of the group index taper.

To derive maximum absorbance enhancement, it is necessary to ensure that slow light effects are maximum at the absorbance peak. Theoretical absorbance spectrum of methane in near-IR show that a broad signature exists between 1665nm and 1668nm with peak at 1665.5nm[11]. It is important to consider propagation losses that occur at low group velocities. Design parameters are chosen so that group index n_g of the guided mode is ~40 at 1665.5nm, corresponding to which the band edge occurs at ~1668.5nm. Input light from a broadband source was TE-polarized and butt-coupled to / from the device with polarization maintaining single mode tapered lensed fiber with mode field diameter ~3μm.

3.3 MEASUREMENT RESULTS

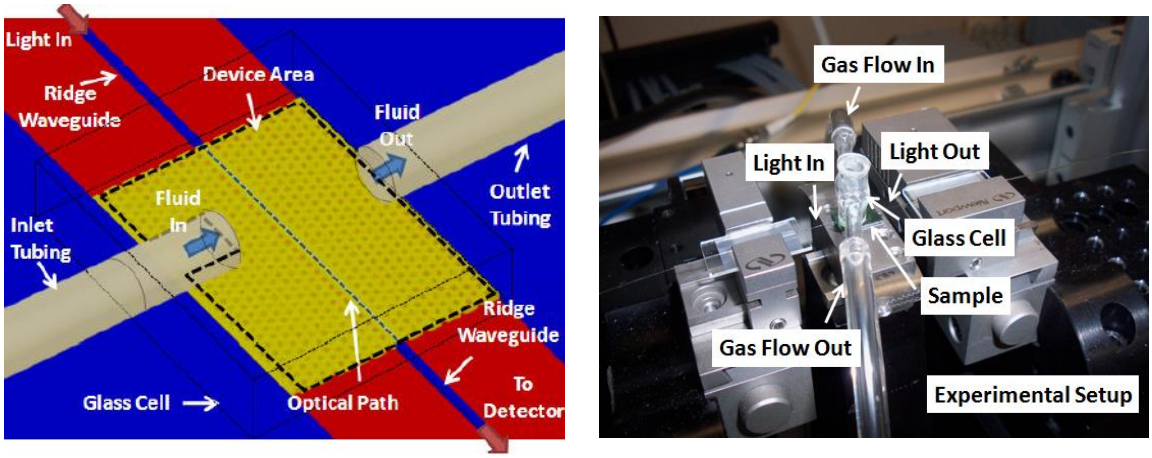

Figure 3.3: (a) Schematic picture of gas flow cell (b) Glass flow cell mounting on top of the device

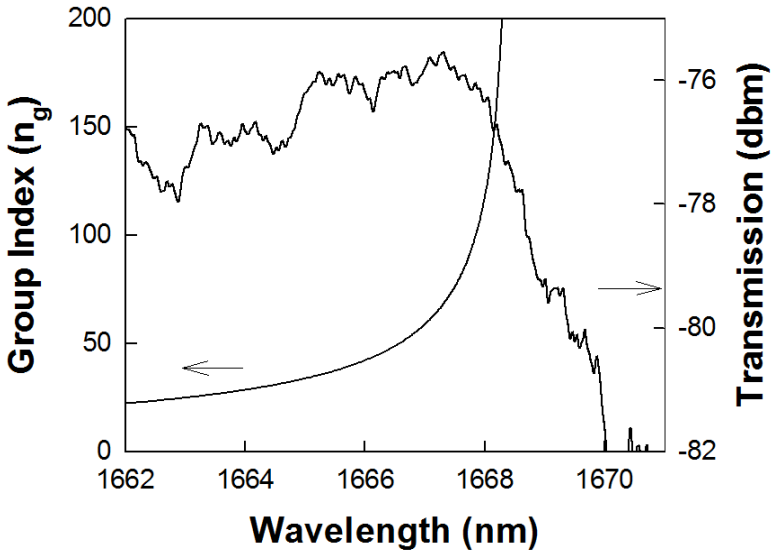

Figure 3.4: (left axis) Group index vs. wavelength as designed in simulations with band edge at ~1668.5nm. (right axis) Experimental transmission spectrum (without analyte), showing band edge shifted in fabricated device to 1670nm.

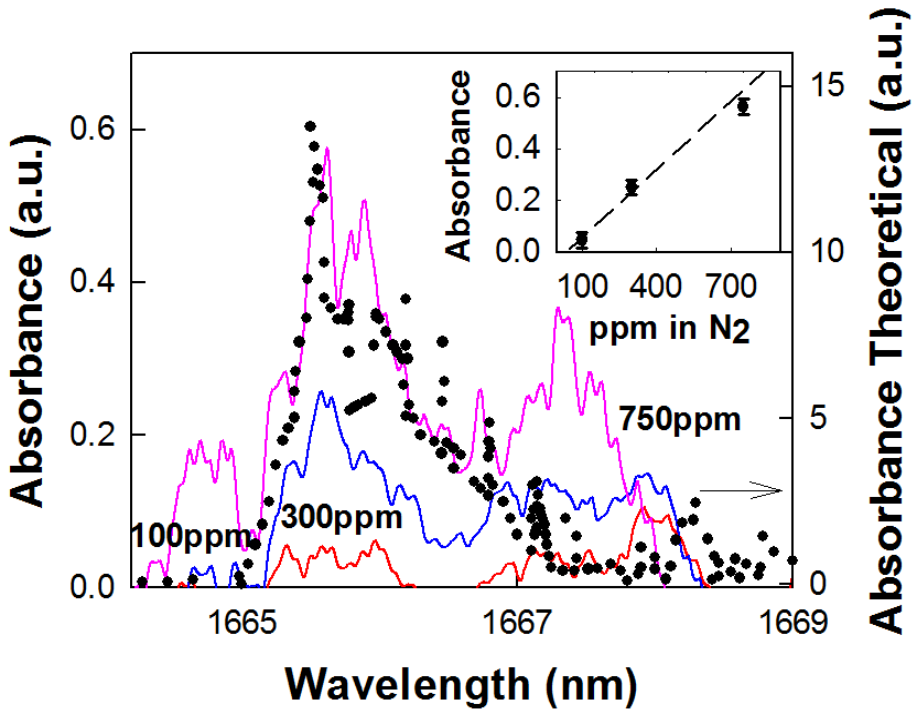

Figure 3.5: (right axis) Theoretical absorbance spectrum of methane obtained from ref. [11] shown by dotted scatter plot. (left axis) Experimental absorbance of methane at various concentrations. The red dashed line is a smoothed trace of the spectrum at 750ppm. (Inset) Peak absorbance magnitude at 1665.5nm versus concentration.

Figure 3.3 shows the experimental setup to detect the gaseous VOCs by using our auto-aligning system. Experimental transmission spectrum in Figure 3.4 shows that the band edge is red-shifted ~1.5nm from design to 1670nm. A mixture of 4% methane (CH_4) in nitrogen (N_2) from Matheson Tri-Gas, was diluted to various concentrations in N_2 using factory calibrated rotameter settings at 20psi pressure. Transmitted light was analyzed with an Ando AQ6317B optical spectrum analyzer with a noise floor -95dbm, in the presence and absence of CH_4 at normal temperature and pressure (NTP). The absorbance of CH_4 is calculated as $\Delta A = A_a - A_{am} = (1/d) \times \ln (P_a/P_{am})$, where P_{am}

and A_{am} denote transmitted power and absorbance respectively in the presence of CH_4, while P_a and A_a denote transmitted power and absorbance respectively in the absence of CH_4, in N_2 ambient.

Response time is determined by the signal integration time of 45seconds. Measurements are performed immediately after gas introduction. Theoretical spectrum of CH_4 [11] is shown in Fig. 4 as a black scatter plot with peak at 1665.5nm. Experimentally obtained CH_4 absorbance spectrum is shown for different concentrations. A peak is observed at 1665.5nm with a broad shoulder around 1667.5nm. Spectra are calculated from experimental transmission spectra for several CH_4 mixing ratios. The absorbance magnitude at 1665.5nm versus concentration is plotted in the inset of Figure 3.5.

As seen in simulations in Figure 3.4, the group index varies rapidly; near the band edge, group index is greater than 100, while ~4.5nm away from the band edge, group index drops to ~30. Higher group index close to the band edge leads to unequal absorbance enhancements; hence the broad shoulder is observed in the experimental absorbance at 1667.5nm. Gas concentrations down to 100ppm (0.2% permissible exposure limit, PEL) were measured, lower than requirements set by Occupational Safety and Health Administration, at 500ppm (or 1% PEL).

The sensitivity of the device is thus a strong function of the position of the band edge and hence fabrication imperfections. The smallest number density of molecules per unit volume that can be determined by absorption spectroscopy [12] is given by

$$N_{\min} = (\frac{dI}{I_0}) / S(\nu)L \qquad (3)$$

where, dI/I_0 is the smallest fractional change in light intensity that can be detected, L is the effective absorption path length and $S(\nu)$ is the absorption cross section of CH_4 at $1.665\mu m = 1.6 \times 10^{-20} cm^2$ [11]. In our measurements, $dI/I_0 \sim 5\times10^{-4}$. From Figure 3.1(b), the slot electric field enhancement factor is ~12; if n_g=100, the expected detection sensitivity from Equation 3 by dividing the number density by the number of molecules per unit volume at NTP is ~40ppm. By comparing the transmission spectrum with simulations, it is estimated that at 1665.5nm, n_g~30 experimentally. Hence less sensitivity is achieved in experiment. By better control on fabrication, the band edge can be shifted closer to the absorbance peak. Since waveguide loss is proportional to group index squared, we believe that the detection sensitivity for methane in near-IR can be increased by at least a factor of 2 with our 300μm long device.

To our knowledge, our device is the only chip integrated device demonstrated for IR absorption spectroscopy of gases compared to other devices that sense refractive index changes only [13-14]. When compared to commercial off-chip handheld TDLAS systems with near-IR sensitivity 1ppm-m [15] or bench-top TDLAS systems with sensitivity 0.1ppm-m, our device has a near-IR sensitivity 0.03ppm-m (100ppm×300μm), consuming less than 20mW power. When combined with wavelength/ frequency modulation [16] in near-IR, further enhancement in sensitivity by more than an order of magnitude is expected. The PC slot waveguide device, based on Maxwell's equations, is also readily scalable to mid-IR. Since methane has ~2 orders larger absorption cross-

section in at 3.3μm [11], high parts per billion (ppb) detection sensitivity can be achieved in PC slot waveguide devices on 300μm length scales in mid-IR with direct absorption spectroscopy, with low ppb sensitivities achieved when combined with wavelength/ frequency modulation. Multiple PC waveguides can be fabricated, each with a different period, to measure absorbance in the corresponding wavelength range, and identifying gases in a mixture uniquely by comparing with known IR absorbance databases.

3.4 SUMMARY

In summary, we demonstrated methane sensing on-chip with a 300μm long silicon PC slot waveguide in this chapter that combines slow light with electric field enhancement to detect by near-IR absorption signatures with measured sensitivity 100ppm. Remote monitoring is enabled by optical fibers.

3.5 REFERENCES

[1] N.A. Mortensen, and S.S. Xiao, Appl. Phys. Lett, 90, 141108 (2007).

[2] E. Yablonovitch, Phys. Rev. Lett. 58, 1059 (1987); S. John, Phys. Rev. Lett., 58, 2486 (1987).

[3] S. Chakravarty, P. Bhattacharya, and Z. Mi, IEEE Photon. Tech. Lett., 18, 2665 (2006).

[4] S.Chakravarty, J.Topoľančik, P.Bhattacharya, S.Chakrabarti, Y. Kang, and M.E. Meyerhoff, Opt. Lett., 30, 2578 (2005).

[5] C-Y. Lin, X. Wang, S. Chakravarty, B-S. Lee, W-C. Lai, J. Luo, A. K-Y. Jen, and R.T. Chen, Appl. Phys. Lett., 97, 093304 (2010).

[6] M. Notomi, Phys. Rev. Lett., 87, 253902 (2001).

[7] X. Chen, W. Jiang, J. Chen, L. Gu, and R.T. Chen, Appl. Phys. Lett., 91, 091111 (2007).

[8] A. Nitkowski, L. Chen, and M. Lipson, Opt. Express., 16, 11930 (2008).

[9] W-C. Lai, S. Chakravarty, X. Wang, C. Lin, and R.T. Chen, Appl. Phys. Lett., 98, 023304 (2011).

[10] X. Wang, S. Chakravarty, B-S. Lee, C. Lin, and R.T. Chen, Opt. Lett., 34, 3202 (2009).

[11] L.S. Rothman et al, Journal of Quantitative Spectroscopy and Radiative Transfer, 110, 533 (2009).

[12] W-B. Yan, Gases and Technology, 1(4), 21 (2002).

[13] J.T. Robinson, L. Chen, and M. Lipson, Opt. Express, 16, 4296 (2008).

[14] N.A. Yebo, P. Lommens, Z. Hens, and R. Baets, Opt. Express, 18, 11859 (2010).

[15] URL: http://www.tdlas.com/products/

[16] A. Karpf, and G.N. Rao, Appl. Optics, 49, 1406 (2010).

Chapter 4: Multiplexed Detection of Xylene and TCE in Water Based on Photonic Crystal Chemical Absorption Spectroscopy

4.1 INTRODUCTION

Infrared (IR) absorption spectroscopy is widely accepted as the ideal technique for chemical sensing due to their unique capability to distinguish analytes of interest based on unique molecular vibration signatures [1, 2]. In these respects, IR spectroscopy has an overwhelming practical advantage over optical methods that depend on sensing changes in refractive index which are not very different when comparing organic substances for instance, volatile organic compounds (VOCs) in water. Commercially available IR spectroscopy systems based on tunable diode laser absorption spectroscopy (TDLAS) [1] or Fourier Transform Infrared Spectroscopy (FTIR) [2] are benchtop systems primarily for measuring gases and are unsuitable for in-situ, continuous, remote monitoring in water ambient.

We have previously demonstrated that in photonic crystal (PC) slot waveguide based on-chip absorption spectroscopy [3, 4] in previous chapters, the optical absorption path length is significantly enhanced compared to free space, thereby leading to enhanced light-matter interaction. As a result, significantly better sensitivities are achieved compared to optical fiber based methods [5, 6]. Using the aforementioned method, we successfully detected xylene directly in water down to concentration of 100ppb (parts per billion) [3] and also detected methane in air down to a concentration of 100ppm (parts per million) [4] with a 300μm long PC slot waveguide. Measurements involved optical

fiber coupled light input and output from the sensing waveguides. Measurements and device packaging considerations are thus obviously simpler than micro-gas chromatography (μGC) based sensors [7, 8] that are limited to compounds that are sufficiently volatile, thermally stable during heating and also volatilizes at temperatures that do not exceed thermal handling capabilities of the column packing. Device packaging is complicated by the need to have heating elements integrated with the chip. Furthermore, in GC and μGC and alternative chip based optical methods for VOC sensing, refractive index changes [9-11] are maximized in a functional polymer for a certain VOC or groups of VOCs. In on-chip absorption spectroscopy, a hydrophobic polymer with optical transparency in the absorbance wavelength range of interest of the VOC is needed. However, a single hydrophobic polymer such as SU-8 or PDMS can be integrated to measure a significant number of VOCs in the near-IR since the VOCs are uniquely identified by their respective unique absorbance signatures in the near-IR.

Gas chromatography (GC) and its corresponding chip-based μGC obviously have the advantage of multiplexed detection. While multiplexing can be achieved by integrating several parallel PC slot waveguides, with an optical fiber array at the input and the output, packaging of commercially available optical fiber arrays would increase complexity and cost. In this chapter, we experimentally demonstrate integrated optics based methodology for the simultaneous multiplexed detection of two VOCs, xylene and TCE with photonic crystal waveguides (PCWs) using a single optical fiber input and output. We also demonstrate that high sensitivities down to 1ppb for xylene and 10ppb for TCE are achieved by using SU-8 as the film for solid phase micro-extraction (SPME)

instead of PDMS (poly-dimethyl siloxane); two orders of magnitude better than our previous demonstration [3] and more than an order of magnitude better than other technologies [7-8, 12-14].

4.2 DEVICE DESIGN STRUCTURE

The device is fabricated in silicon in a silicon-on-insulator (SOI) substrate using standard ebeam lithography and reactive ion etching [3]. The principle of operation of our device is governed by the Beer-Lambert law for optical absorption spectroscopy. According to this law, the transmitted intensity I is given by

$$I = I_0 \exp(-\gamma \alpha L) \tag{1}$$

where I_0 is the incident intensity, γ is the absorption coefficient of the medium, L is the interaction length, and α is the medium-specific absorption factor determined by dispersion enhanced light-matter interaction. For various applications, L must be large to achieve high sensitivity since α =1.

In addition, from perturbation theory,

$$\gamma \propto f \times \frac{c/n}{v_g} \tag{2}$$

where c is the velocity of light in free space, v_g is the group velocity in the medium, and *n* is the refractive index of the medium [15]. *f* denotes the filling factor denoting relative fraction of optical field residing in the analyte medium. Group velocity v_g is inversely proportional to the group index n_g. Hence, theoretically, the optical absorbance by a

waveguide on chip increases in order as follows in silicon: a) ridge waveguides, (n_g~3), b) slotted ridge waveguides (n_g~3, f~10) since the intensity of light in a low-index slot is significantly enhanced compared to ridge waveguides, c) photonic crystal waveguides (PCWs) (n_g~100) [16], and d) slotted photonic crystal waveguide (f~10 and n_g~100 for a combined factor of ~1000).

The multiplexed device comprises two 300μm long PCWs fabricated in the two output arms of a 1×2 multimode interference (MMI) power splitter. In contrast to end-fire coupling used previously, light is coupled into the MMI via an input sub-wavelength grating (SWG) from a single input optical fiber. Our studies indicate that coupling losses are minimized by the use of SWGs [19].At the output of the PCWs, the waveguides are combined with a Y-junction power combiner. At the output, the combined transmission spectra from each PCW are coupled via an output SWG to a single output optical fiber. In Figure 4.1(a), a stitched image of the whole device is shown. Y-junction combiner, PCW and MMI regions are magnified in Figure 4.1(b)-(d) respectively.

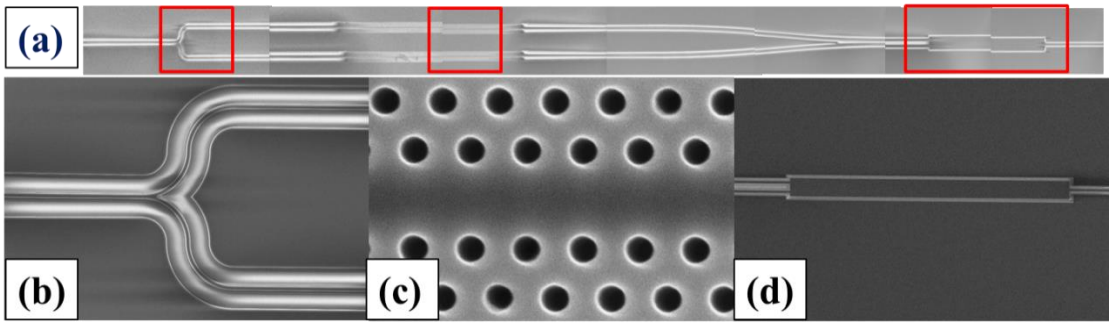

Figure 4.1: (a) Stitched scanning electron microscopy (SEM) images of the full device with three regions (in red lines) magnified in (b)-(d). (b) Y-junction combiner (c) W1line defect Photonic Crystal Waveguide (d) MMI Optical power splitter.

A 2 μm thick SU8 polymer is spun on top of device. Since SU8 is hydrophobic, hence the absorption spectrum of VOCs can be obtained independent of any interference from the strong absorbance signatures of water. In contrast to our previous method using PDMS [3], SU-8 was used since it has low optical absorption loss in the wavelength range of interest between 1.62-1.7μm resulting in high signal-to-noise ratio. All component devices in Figure 4.1 are thus designed and fabricated with a SU8 top cladding.

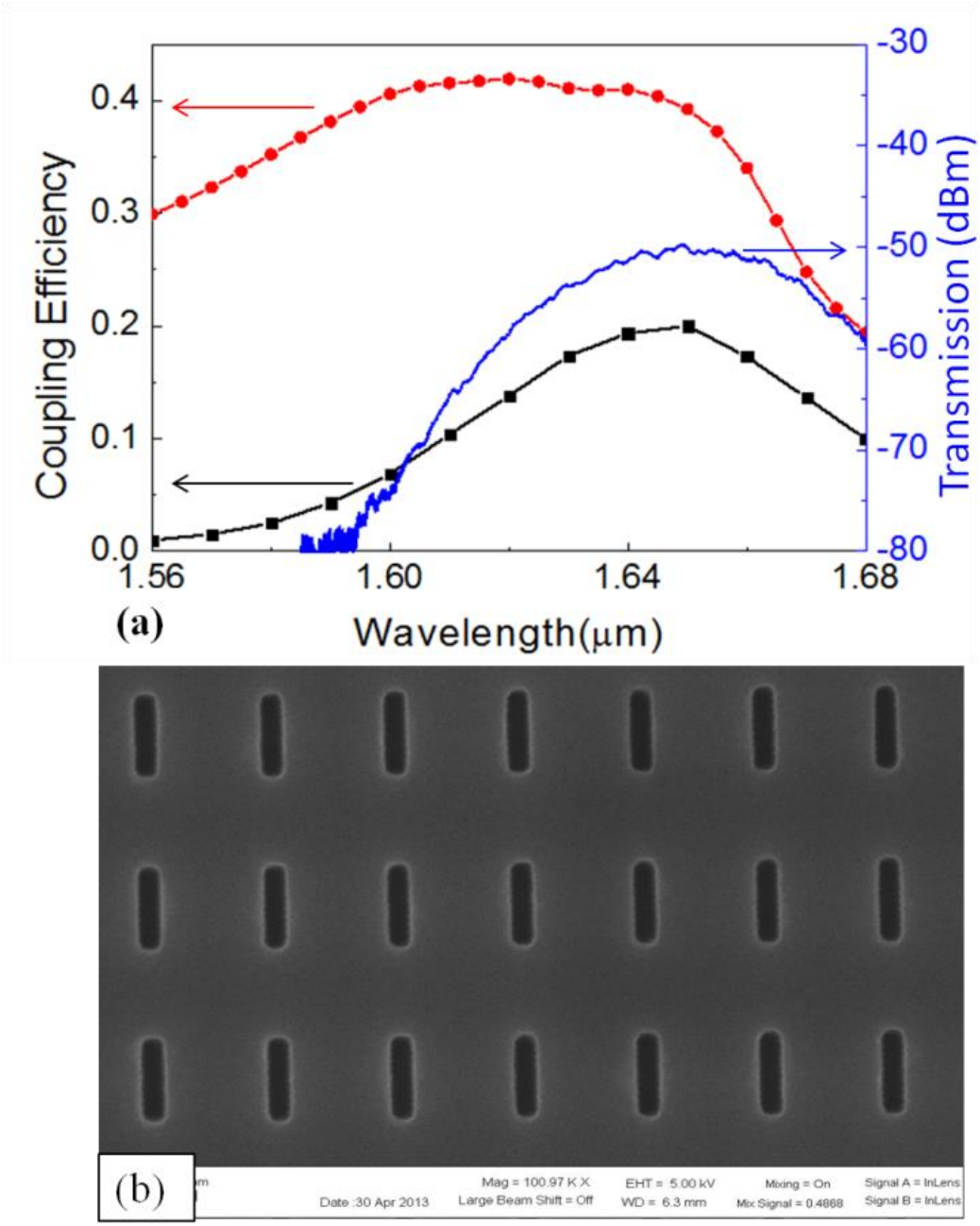

Figure 4.2: (a) Simulated coupling efficiency to air (Red), to the fiber (Black) and the experimental transmission of strip waveguide (Blue) show the coupling peak locates around 1.65μm (b) SEM picture shows the subwavelength grating (SWG) structure

The simulated coupling efficiencies of the SWG to the optical fiber and to air, calculated by eigenmode expansion simulations with CAMFR [20], are shown in Figure 4.2(a). Since a single SWG feeds both W1 PCWs, the SWGs are designed to have the maximum coupling efficiency around 1.65μm so as to cover the absorption spectra of TCE and xylene at 1.644μm and 1.674μm. Figure 4.2 (b) shows the SEM image of the fabricated SWG. The two-dimensional (2-D) SWG periods are chosen as 426 nm and 695 nm along and perpendicular to the waveguide propagation direction. The corresponding trench widths are 79 nm and 340 nm respectively. The design results in an effective sub-wavelength refractive index (n_{sub}) 2.58 in the propagation direction. The general design of SWG is described in Ref. [17]. The resultant transmission spectrum, shown in Figure 4.2(a) by the plot in blue, has a maximum transmission near 1.65 μm.

The MMI is designed with a width of 16 μm and a length of 214 μm to achieve optimum 1×2 optical power splitting as shown by the simulation in Figure 4.3(b). A schematic W1 PCW with lattice constant *a* is shown in Figure 4.3(a), where W1 denotes that the width of the PCW is $\sqrt{3}a$. Since the absorption peaks of TCE and xylene are located at 1.644μm and 1.674μm respectively, devices are designed with band edges adjacent to the absorption peaks. Thus, maximum slow light enhancement can be obtained at the absorbance peaks for maximum sensitivity. For xylene, a=403 nm while for TCE a= 395 nm. The air hole diameter is 0.53a in both PCW arms.

In Figure 4.4, transmission spectrum of the multiplexed PCW device is shown. The design achieves a transmission band with a band edge near 1644nm (in blue) from

one PCW and another band edge near 1674nm (in red) from the second PCW in the other arm of the MMI. The location of the band edges are indicated by the respective arrows. The variation from design is attributed to fabrication induced errors. The theoretical absorbance spectra indicated in dashed and dotted lines for TCE [18] and xylene [19] respectively. Based on previous results which show that guided wave propagation is obtained in PCWs in SOI platform up to n_g ~35 with low loss, at the transmission band edge [21], transmitted light being negligible at higher n_g, it is estimated from simulations, that the group indices of the guided mode at 1644nm and 1674nm for the individual waveguides are 23 and 33 respectively.

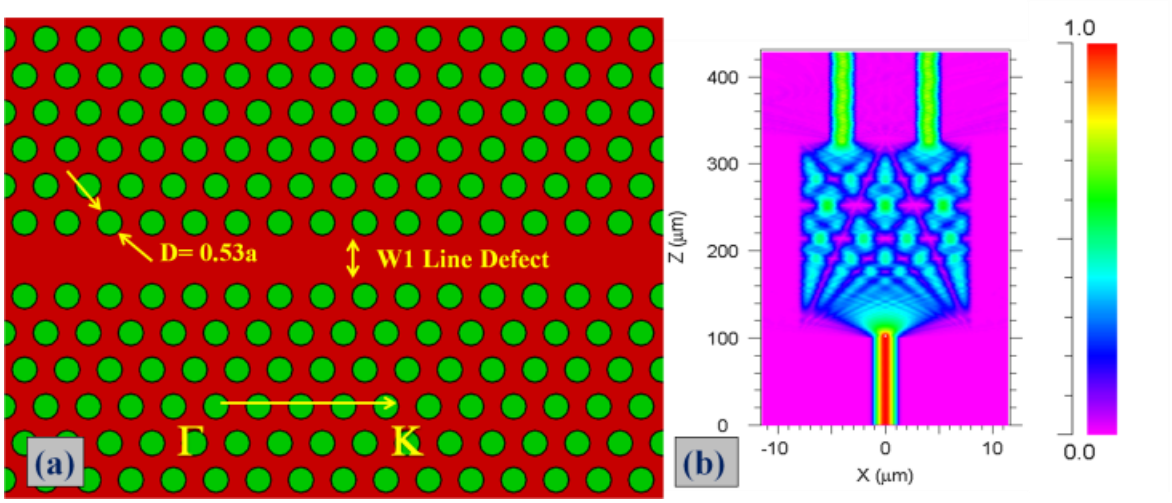

Figure 4.3: (a) Schematic of W1 line defect PCW. (b) Beam propagation simulation of designed 1×2 MMI.

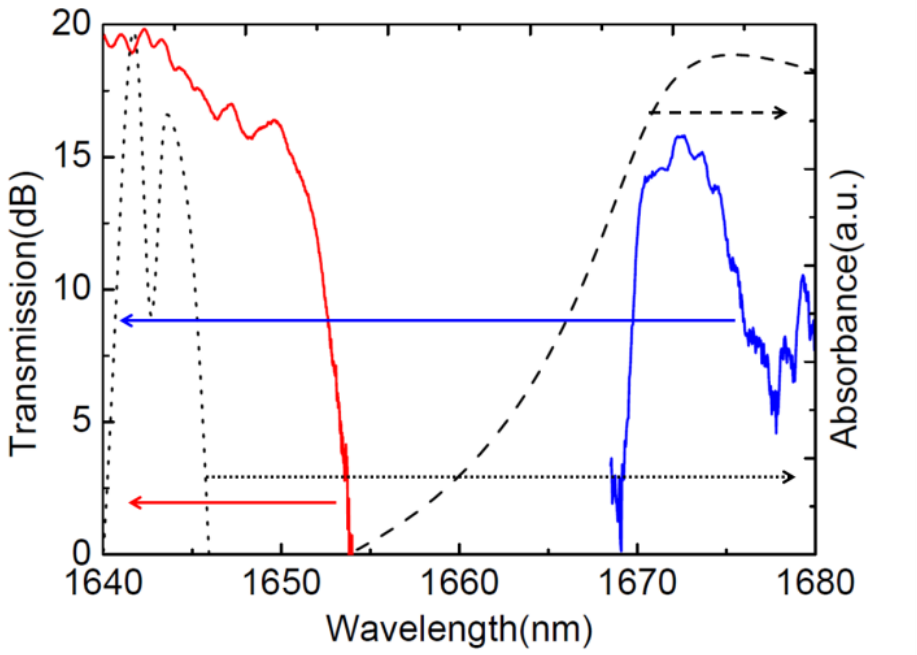

Figure 4.4: Transmission of single PC devices with *a*=395nm (in red) and *a*=403nm (in blue). Theoretical absorbance is shown for TCE with peak at 1644nm (dotted) and xylene with peak at 1674nm (dashed).

4.3. EXPERIMENT

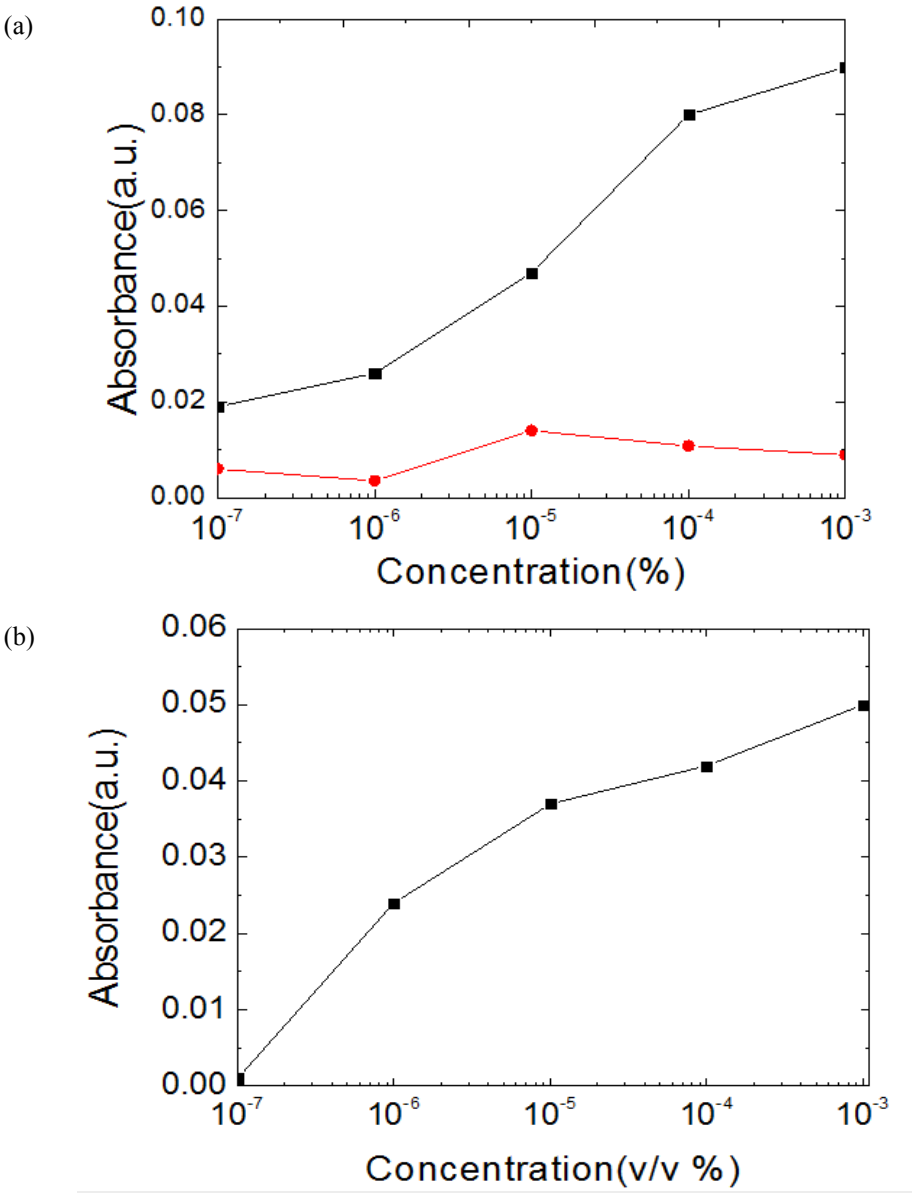

Figure 4.5: (a) Absorbance of xylene measured at 1674nm with PC waveguide (in Black) and strip waveguide (in Red) (b) Absorbance of TCE measured at 1644nm.

Figures 4.5(a) and 4.5(b) show the experimentally determined absorbance of xylene and TCE from the individual PCWs of Figure 4.4 when the device is immersed in water. All measurements are done 10 minutes after sample addition, which is a typical time observed in measurements beyond which no further change in absorbance is observed. The 2μm thick SU-8 ensures negligible overlap of the propagating optical mode with ambient water. Increasing concentrations of xylene and TCE are added separately. Subsequent to each measurement, the solution is removed by suction, and the next solution added after 10 minutes. The absorbance is calculated by comparing the transmitted light output at each concentration to the transmitted light intensity with no VOC. From the absorbance, the detection limit for device for xylene is 10^{-7} % (v/v) in water (~1ppb) and the detection limit for device for TCE is 10^{-6} % (v/v) in water (~10ppb). Measurements in xylene were also done on a ridge waveguide on chip with no PCW. Negligible absorbance was observed as shown in the red plot in Figure 4.5(a).

For multiplexed detection of xylene and TCE, in order to test the selectivity of our device, 10^{-5} % (v/v) xylene in water was added on the multiplexed devices. The transmission is measured from the multiplexed device and the absorbance calculated at 1674nm and 1644nm for xylene and TCE. In Fig. 4.6(a), the multiplexed device shows a flat and almost zero absorbance at 1644nm, but significant absorbance is observed at 1674nm in Figure 4.6(b). Next, a solution of 10^{-5} % TCE in water is added on these two devices. In Figure 4.6(c), the device shows an absorbance near 1644nm; in contrast, there is almost flat absorbance for device designed for xylene in Figure 4.6(d). Finally, a

mixture of 10^{-5} % xylene and 10^{-5} % TCE in water was prepared and the solution added. In Figure 4.6(e) and (f), the absorbance of both xylene and TCE are observed.

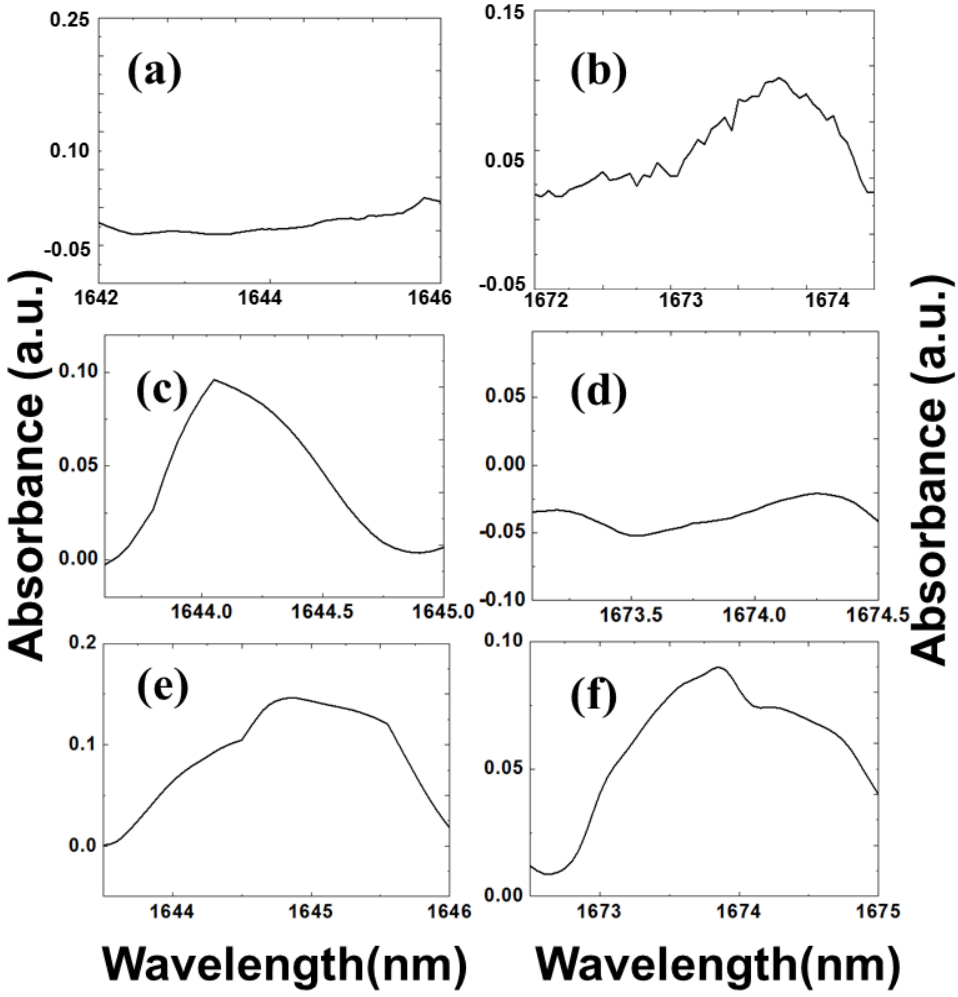

Figure 4.6: Absorbance after sequentially adding (a-b) 10^{-5}% xylene (c-d) 10^{-5} % TCE and (e-f) 10^{-5} % mixture of xylene and TCE. Absorbance of TCE and xylene are measured at 1644nm and 1674nm respectively.

4.4 Discussion and Conclusions

The negligible absorbance observed from ridge waveguides of the same total length between input and output SWGs as the multiplexed device in Figure 4.1 with PCW shows that the increased absorbance is due to the slow light effect in the PCW. Since SU-8 is more transparent optically than PDMS in the near-IR range probed here, by using SU-8 as the hydrophobic layer, the signal-to-noise ratio was effectively enhanced at the measured wavelengths which therefore lowered the detection sensitivity of our device to 1ppb for xylene compared to 100ppb previously [3]. Table 1 compares detection sensitivities experimentally observed in other platforms versus our PCW based on-chip absorption spectroscopy sensor. More than an order of magnitude enhancement in sensitivity is observed.

Table 4.1 Comparison of different methods and detection limits of VOCs in water

Author	***Method***	***Sensitivity***
Lai et al., 2011[3]	PCSW Absorption spectroscopy with PDMS	100ppb (xylene)
Reddy et al., 2012 [7]	Micro-gas chromatography	28 ppb (toluene)
Girschikofsky et al., 2012 [9]	Optical planar Bragg grating	20ppm (xylene), 70ppm (toluene)
St-Gelais et al., 2013 [10]	Fabry-Perot Interferometers	1.6 ppm for (xylene)
Hue et al., 2013 [22]	Nanoporous discs Absorbance	20ppb (benzene), 10ppb for xylene
Lai et al., 2013 (This Work)	**PCW Absorption Spectroscopy with SU-8**	**1ppb (xylene), 10ppb (TCE)**

The lower sensitivity of TCE is due to fabrication induced errors that shifts the transmission band edge from design values and therefore results in a lower group index at 1644nm at the absorbance maxima of TCE. While 10ppb was experimentally measured, based on the absorbance magnitude in Figure 4.5(b), it is estimated that the sensitivity for xylene is better than 10ppb. We demonstrated the highest sensitivity among existing

technologies for the detection of xylene with near-IR absorbance signatures. Since absorbance signatures are larger in the mid-IR, higher sensitivities can be expected if above multiplexed devices are fabricated in the mid-IR. Furthermore, when integrated with a PC slot waveguide with SU-8 as the SPME layer, higher sensitivities will be observed. Higher order multiplexing can be achieved with higher order MMI and Y-junction power splitters and combiners to simultaneously detect more VOCs with selectivity [23].

In summary, we demonstrated multiplexed detection of TCE and xylene in water using PC based chip-integrated optical absorption spectroscopy in a single absorbance measurement. Remote, continuous monitoring is enabled by optical fibers. The authors acknowledge the National Science Foundation for supporting this work. (Contract # IIP-1127251)

4.5 REFERENCES

[1] M. Lackner, Rev. Chem. Eng., 23, 65 (2007).

[2] F. Adler, P. Maslowski, A. Foltynowicz, K. C. Cossel, T. C. Briles, I. Hartl, and J. Ye, Opt. Exp. 18, 218610 (2010).

[3] W.-C. Lai, S. Chakravarty, X. Wang, C. Lin, and R. T. Chen, Appl. Phys. Lett., 98, 023304 (2011).

[4] W.-C. Lai, S. Chakravarty, X. Wang, C. Lin, and R. T. Chen, Optics Lett., 36, 984–6 (2011).

[5] K.M.G. Lima, I.M. Raimundo, and M.F. Pimentel, Sens. & Act. B-Chem., 125, 229 (2007).

[6] J. Buerck, S. Roth, K. Kraemer, M. Scholz, and N. Klaas, J. Hazard. Mater., 83, 11 (2001).

[7] K. Reddy, Y. Guo, J. Liu, W. Lee, M. K. K. Oo, and X. Fan, Lab Chip, 12, 901–5 (2012).

[8] C-J. Lu, W.H. Steinecker, W-C. Tian, M.C. Oborny, J.M. Nichols, M. Agah, J.A. Potkay, H.K.L. Chan, J. Driscoll, R.D. Sacks, K.D. Wise, S.W. Pang, E.T. Zellers, Lab Chip, 5, 1123 (2005).

[9] M. Girschikofsky, M. Rosenberger, S. Belle, M. Brutschy, S. R. Waldvogel, and R. Hellmann, Sens. & Act. B: Chem., 171-172, 338–342 (2012).

[10] R. St-Gelais, G. Mackey, J. Saunders, J. Zhou, A. Leblanc-Hotte, A. Poulin, J. a. Barnes, H.-P. Loock, R. S. Brown, and Y.-A. Peter, Sens. & Act. B: Chem., 182, 45–52 (2013).

[11] M. Deng, C.-P. Tang, T. Zhu, Y.-J. Rao, L.-C. Xu, and M. Han, Appl. Optics, 49, 1593–8 (2010).

[12] Q.-Y. Cai and E. T. Zellers, Anal. Chem., 74, 3533–3539 (2002).

[13] D. Matatagui, J. Marti, M. J. Fernandez, J. L. Fontecha, J. Gutierrez, I. Gracia, C. Cane and M. C. Horrillo, Sens. & Act. B: Chem., 154, 199–205 (2011).

[14] J. Liu, Y. Sun, D. J. Howard, G. Frye-Mason, A. K. Thompson, S.-J. Ja, S.-K. Wang, M. Bai, H. Taub, M. Almasri and X. Fan, Anal. Chem., 82, 4370–4375 (2010).

[15] Mortensen, N.A., and Xiao, S.S., Appl. Phys. Lett., 90(14), 141108 (2007).

[16] M. Notomi, K. Yamada, A. Shinya, J. Takahashi, C. Takahashi, and I. Yokohama, Phys. Rev. Lett., 87, 253902 (2001).

[17] S. H. Tao, Q. Fang, J. F. Song, M. B. Yu, G. Q. Lo, and D. L. Kwong, Opt. Express, 16, 26 (2008).

[18] A.C.R. Pipino, J.P.M. Hoefnagels, and N. Watanabe, J. Chem. Phys., 120, 2879 (2004).

[19] D.A. Burns, Handbook of near-infrared analysis, 3rd Edition, Hoboken: Taylor and Francis Ltd (2007).

[20] X. Xu, H. Subbaraman, J. Covey, D. Kwong, A. Hosseini, and R. T. Chen, Appl. Phys. Lett, 101, 031109 (2012).

[21] C.-Y. Lin, X. Wang, S. Chakravarty, B. S. Lee, W.-C. Lai, and R. T. Chen, Appl. Phys. Lett., 97(18), 183302 (2010).

[22] J. Hue, M. Dupoy, T. Bordy, R. Rousier, S. Vignoud, B. Schaerer, T.-H. Tran-Thi, C. Rivron, L. Mugherli, and P. Karpe, Sens. & Act. B: Chem. (2013); http://dx.doi.org/10.1016/j.snb.2013.03.047

[23] A. Hosseini, D. Kwong, C. Lin, B. S. Lee, and R. T. Chen, IEEE J. Sel. Top. Quant. Electron, 16, 61–69 (2010).

Chapter 5: Slow Light Enhanced Sensitivity of Resonance Modes in Photonic Crystal Biosensors

5.1 INTRODUCTION

Over the past several years, significant research has focused on achieving higher sensitivities in chip-integrated label-free biosensors based on different methods such as ring resonator [1], surface plasmon resonance (SPR) [2], directional coupler [3], Mach-Zehnder interferometer (MZI) [4] and photonic crystal (PC) [5-7]. Amongst all devices in integrated optics, PC devices provide the unique characteristic of slow light in photonic crystal waveguide (PCW) architectures which effectively enhances light-matter interaction [8], thereby leading to high sensitivities in compact device geometries. The advantage of slow light has been proved in several applications such as optical modulator [9], optical infrared absorption sensing on liquid contaminants [10], and optical spectrometry on gaseous contaminants [11]. Highest sensitivity devices on the two-dimensional PC platform have been also been demonstrated by our group as biosensors for chip-integrated microarray applications in proteomics. We demonstrated methods to increase the quality factor (Q) as well as the sensitivity in PC microcavity coupled PC waveguide architectures by tailoring the radiation loss as well as the optical mode volume of PC microcavity resonances [5, 7]. In this chapter, we show experimentally that in PC microcavity coupled waveguide systems, the slow light effect in the coupling waveguide also contributes to enhanced sensor sensitivity.

5.2 DEVICE STRUCTURE

The device investigated is a L13 PC microcavity coupled to a W1 PCW in silicon in a silicon-on-insulator (SOI) platform in which we have previously demonstrated highest biosensing sensitivity among competing optical technologies at a concentration of 0.1μg/ml. The PC consists of a triangular lattice of air holes with lattice constant a=392nm. The air holes have radius r =0.277a and the height of the silicon slab is h=250nm. The W1 PCW is formed by removing a complete row of air holes along the Γ−K direction in a triangular lattice photonic crystal. The L13 PC microcavity is formed by removing 13 air holes in dielectric silicon parallel to the W1 PCW. Figure 5.1(a) shows a scanning electron micrograph (SEM) of the device. Light transmitted down the PCW is dropped at frequencies corresponding to the resonance frequency of the microcavity. A typical transmission spectrum of the L13 PC microcavity is shown in Figure 5.1(b) in water and Figure 5.1(c) in glycerol. The sensor works on the principle that refractive index changes in the vicinity of the PC microcavity leads to a shift in the resonance wavelength, the sensitivity of the sensor determined by the magnitude of the resonance wavelength change for a given change in refractive index in chemical sensing or a given change in biomolecule concentration in biosensing.

Figure 5.1(b) shows that multiple resonances of the L13 PC microcavity are dropped from the transmission spectrum of the W1 PCW. We limit our study to the three modes labeled A, B and C nearest to the W1 PCW transmission band edge at 1568nm. Figure 5.2(a) plots the dispersion diagram that shows the resonance mode of the L13 PC microcavity coupled to the W1 PCW. The resonance mode frequencies of A, B and C are

calculated from the experimental transmission spectrum in Figure 5.1(b). The band edge in Figure 5.1(b) corresponds to approximately to $a/\lambda=0.25$ where the simulated group index $n_g=33$ as seen from Figure 5.2(a). The experimental band edge is offset from the simulated band edge due to high transmission losses at higher n_g values and is consistent with maximum n_g ~35 observed experimentally in air-clad PCW structures demonstrated previously [12]. It is observed that at the coupling frequencies of modes A, B and C, the group velocities of the W1 PCW guided mode are 13.2, 9.8 and 7.9 respectively.

5.3 DEVICE MEASUREMENT AND DISCUSSION

Devices were measured in water (refractive index n=1.33) and glycerol (n=1.46) and the bulk sensitivity in nm/RIU (RIU=refractive index unit) was determined and plotted in Figure 5.2(b) for the individual modes A, B and C. Figure 5.2(b) shows that mode A, has the highest bulk sensitivity of 66nm/RIU. Figure 5.2(b) also plots the Q and the bulk sensitivities of modes A, B and C when the L13 PC microcavity is coupled to wider PCWs W1.025 and W1.05. (W1.05 indicates that the width of the PCW is $1.05\times\sqrt{3}a$ where a is the lattice constant of the PC pattern).

Figure 5.3 plots the sensitivity of the respective modes A, B and C as a function of concentration of the biomolecule avidin which binds to its conjugate specific biotin that is immobilized on the L13 PC microcavity when coupled to a W1 PCW. The procedure of surface functionalization, target antibody (biotin) immobilization and subsequent biosensing has been described in detail in Ref. [7] and is not repeated here. The surface sensitivity to biosensing is determined by the magnitude of the resonance wavelength shift when a specific concentration of probe biomolecule avidin is introduced in solution and binds to its conjugate specific biomolecule biotin. It is observed from Figure 5.3 that mode A shows the highest sensitivity. The difference in wavelength shifts of the resonance modes is much larger than the 0.02nm wavelength accuracy of our optical spectrum analyzer.

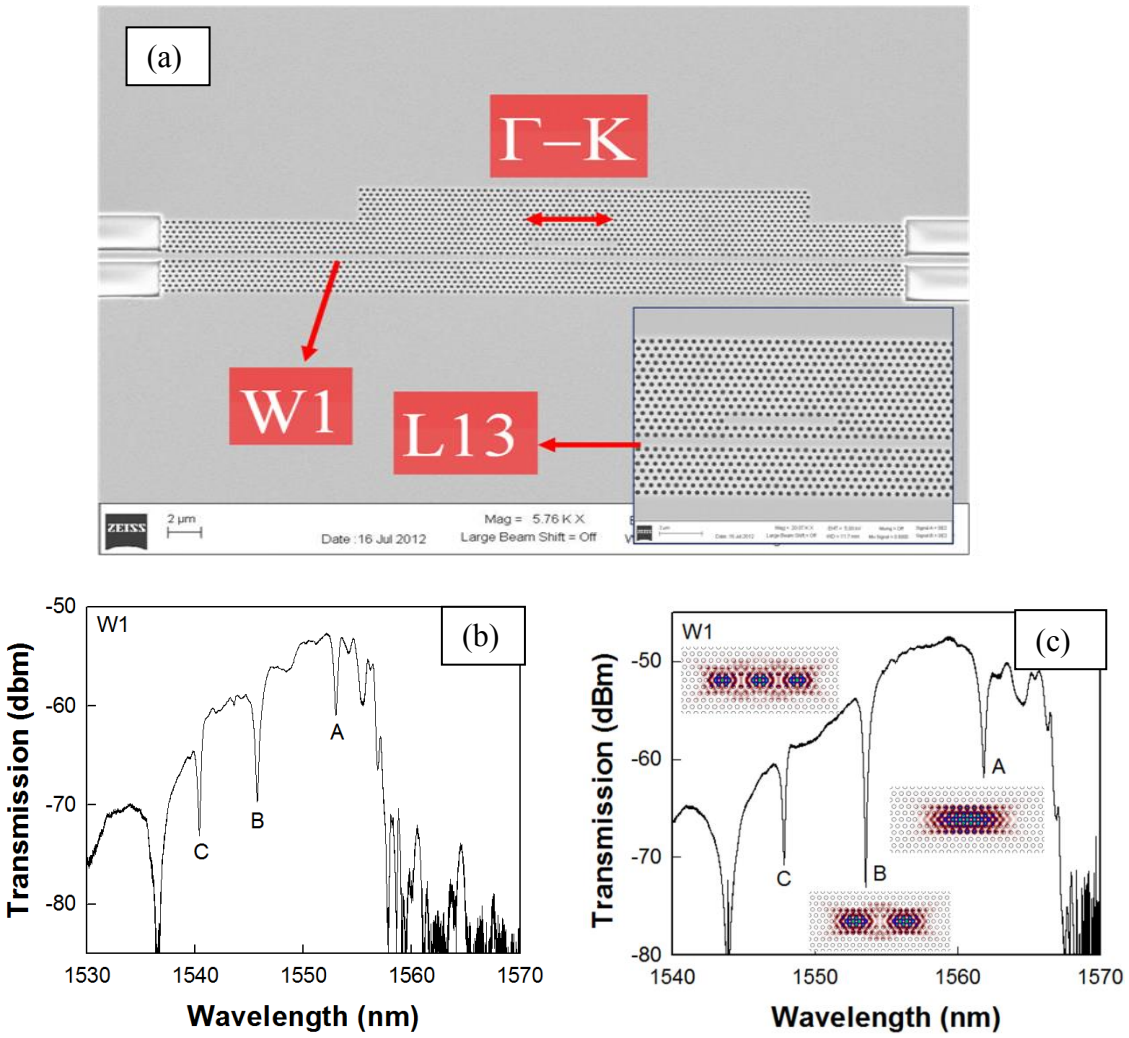

Figure 5.1: (a) SEM of L13 PC microcavity and W1 waveguide. Inset shows the magnified picture on L13 PC microcavity. (b) Experimental transmission spectrum of device in (b) water and (c) glycerol, showing the resonance modes and mode profiles in the insets

With respect to the modes A, B and C, it is expected that the sensitivity is determined by the mode Q as well as the optical overlap of the mode with the analyte near the surface of the PC microcavity and the holes in the vicinity of the PC

microcavity. The total quality factor (Q) of a resonance mode in the side-coupled cavity-waveguide architectures is given by:

$$\frac{1}{Q} = \frac{1}{Q_i} + \frac{1}{Q_R} + \frac{1}{Q_{WG}} \tag{1}$$

$Q_i = \omega\tau_i$, τ_i denotes the intrinsic cavity loss time constant which includes surface roughness and material absorption losses, $Q_R = \omega\tau_R$, τ_R denotes the radiation loss time constant from the microcavity and $Q_{WG} = \omega\tau_{WG}$, τ_{WG} denotes the leakage loss time constant from the microcavity to the waveguide.

$$\frac{1}{\tau_R} = \frac{P_R}{W_E} \tag{2}$$

where P_R denotes the total power radiated by the cavity and W_E denotes the stored energy in the cavity which is proportional to the cavity mode volume. We have shown previously that lower P_R and higher W_E decreases the net radiation loss rate from the cavity and hence increases the effective Q [5, 7]. Higher Q results in light being trapped in the microcavity for a longer duration at the particular resonance frequency which results in enhanced light-matter interaction and thus higher sensitivity. Q of the modes A and B are nearly the same within the range of experimental variation. The optical overlap of modes A and B, estimated from the mode profile by integrating over an area where the E-field intensity is more than 50% of the maximum value [13] and including the entire internal surface area of the holes along the periphery of the PC microcavity, is nearly the same. However, the optical coupling efficiency from the W1 PCW of

resonance mode A is much higher than that of B. The coupling efficiency η between the cavity and the waveguide is described by

$$\eta \propto \frac{L}{v_g} \tag{3}$$

where L denotes the interaction length between the cavity mode and the waveguide, and v_g denotes the group velocity at the resonance frequency of the corresponding optical mode. v_g is inversely proportional to n_g. Since the coupling strength is inversely proportional to v_g, farther away from the band edge, where v_g is high, the coupling strength is low. As a result of the lower optical coupling of incident light into the optical cavity for mode B compared to mode A, light-matter interaction inside the cavity is also reduced which contributes to the lower sensitivity of B compared to A. Similarly, resonance modes A, B and C have decreasing sensitivity in order, when the L13 PC microcavity is coupled to the wider PCWs W1.025 and W1.05.

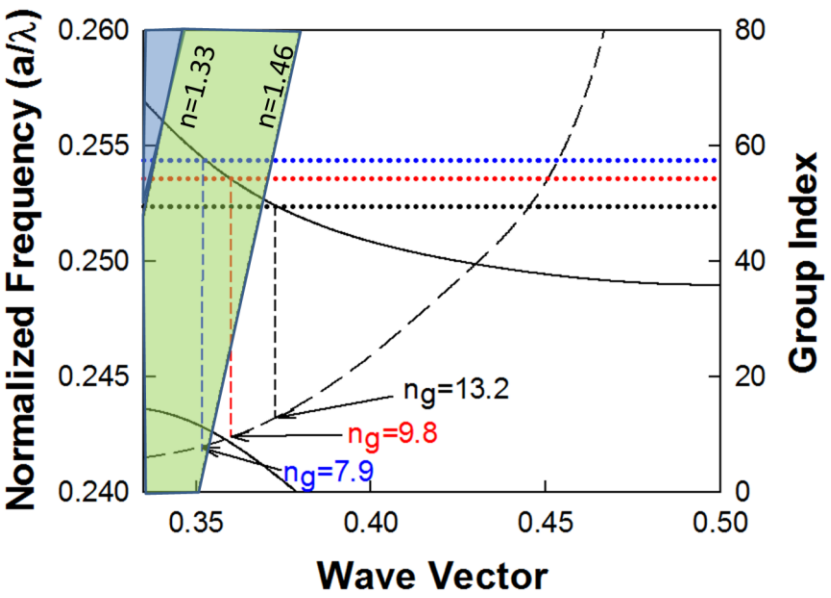

(a)

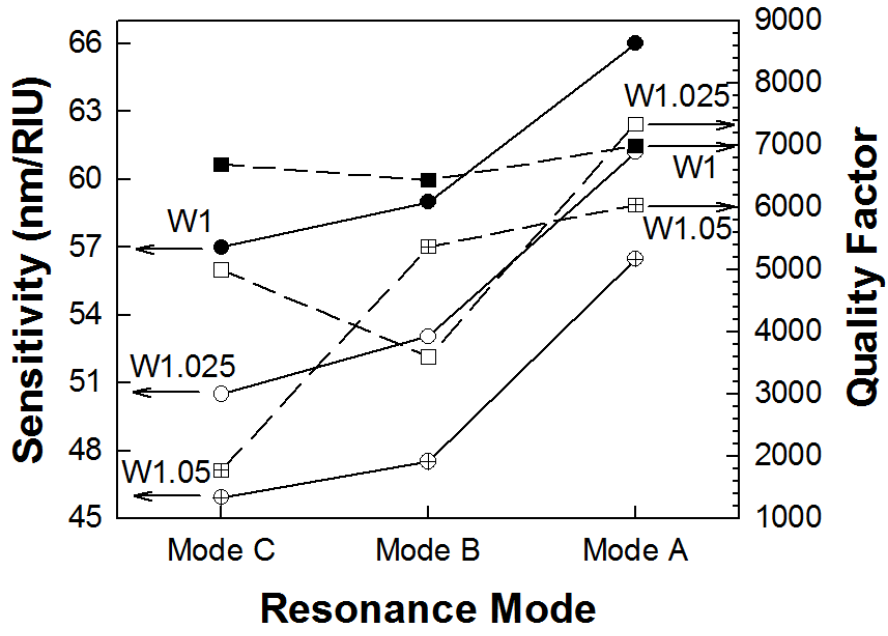

(b)

Figure 5.2: (a) Dispersion diagram of the W1 PCW with the coupled L13 PC microcavity mode frequencies A, B, C shown in black, red, blue dotted lines respectively. Simulated group index of the W1 PCW is shown on the right axis. (b) Sensitivity values and Q-factors in water of resonance modes A, B and C are shown for W1 as filled circles and filled squares respectively, for W1.025 as open circles and open squares and for W1.05 as crossed circle and crossed squares respectively.

In order to separate the effects of Q_R and Q_{WG}, the coupling of the resonance mode A only to the PCW is studied at different propagation group velocities of the PCW. Figure 5.4 shows the dispersion diagrams of the W1, W1.025 and W1.05 PCWs. The coupling frequency of the L13 resonance mode is shown. The mode A moves to lower frequencies with increasing width of the PCW due to increased dielectric fraction in the vicinity of the L13 PC microcavity. The simulated group index values at the coupling frequencies are indicated. The group indices of the W1, W1.025 and W1.05 PCW at the coupling frequency of the resonance mode A of the L13 PCW are 13.2, 12.7 and 10.2 respectively. Figures 5.5(a) and (b) show the experimental transmission spectra of W1.025 and W1.05 PCWs. Figure 5.6 shows the results of the sensing experiments for the three waveguides with coupled L13 PC microcavity resonance A, when the device is measured in water and glycerol. In an uncoupled cavity, Q_R of the resonance mode A would increase from W1 to W1.05 due to the reduced radiation loss P_R as the mode moves towards the dielectric band in the band diagram. Q_i can also be expected to increase from W1 to W1.05 as the air holes on the opposite side of the W1 PCW as the PC microcavity move farther away. Furthermore, optical mode overlap of the resonance modes A with the analyte primarily occurs in the first two rows of holes along the periphery of the L13 PC microcavity which is unchanged from W1 to W1.025 and W1.05 since the L13 PC microcavity is located two periods away from the PCW in each case. Hence the additional factor that results in higher sensitivity of W1 compared to W1.05 PCW is η.

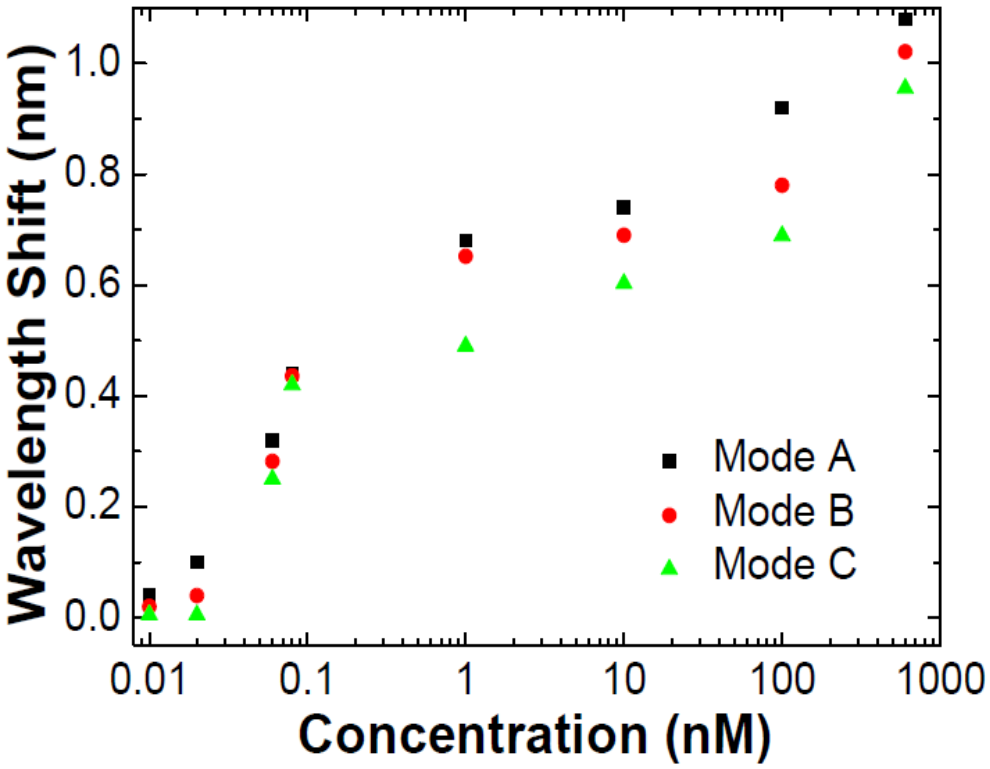

Figure 5.3: The wavelength shift of each resonance modes at different concentration. Solid square dots denote the resonance Mode A. Solid circle dots denote Mode B, and the solid triangle dots are Mode C.

As expected from Equation 3, a lower τ_{WG} leads to higher coupling efficiency of light from the W1 PCW to the L13 PC microcavity resonance mode A, leading to more light-matter interaction in the case of the W1 PCW versus the W1.05 PCW. Similarly, the sensitivity of the resonant mode A for W1 PCW is higher than W1.025 PCW as observed from Figure 5.6 due to the higher group index of W1 at the coupling frequency with the L13 PC microcavity resonance A. Previously we have shown that increased Q_R increases device sensitivity. [7] Both control experiments in this chapter confirm that, in addition to

Q and optical mode overlap with analyte, slow group velocities of light propagating in the PCW contribute to the enhanced light-matter interaction and thus the enhanced sensitivities of resonance modes in PC microcavities. Similar trends are observed for modes B and C from Figure 5.2(b).

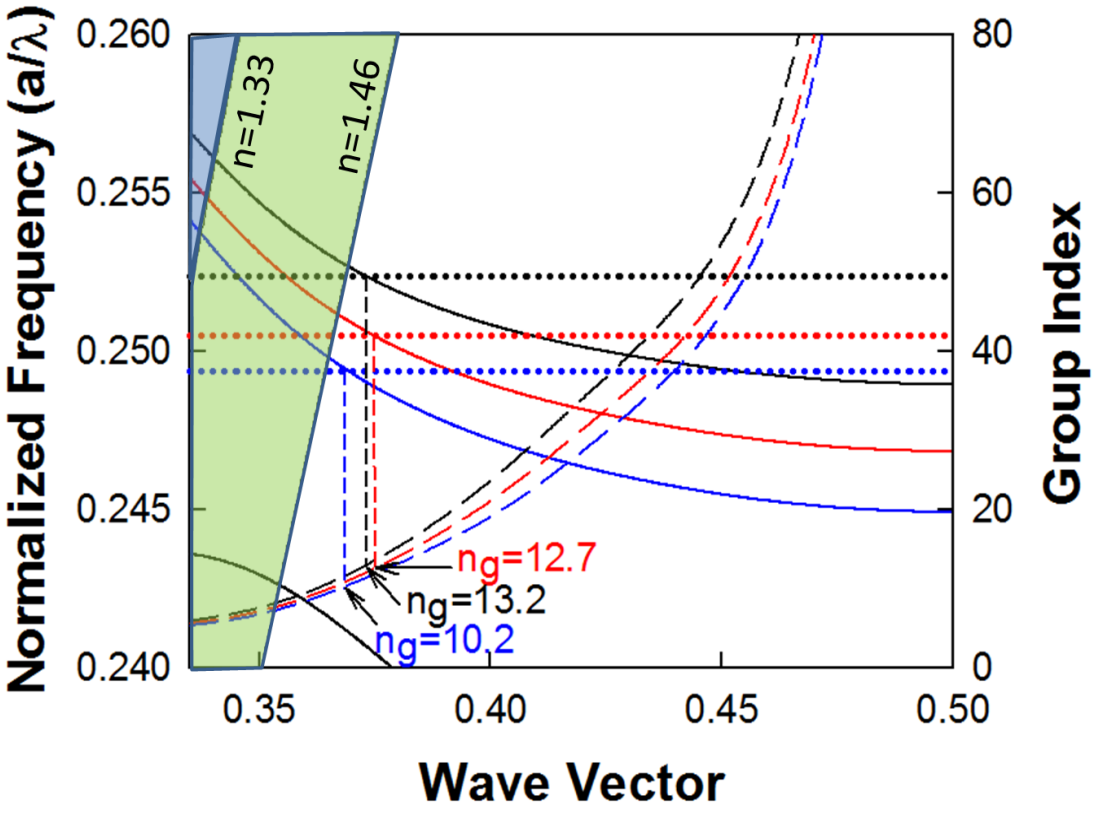

(a)

Figure 5.4: Dispersion diagrams of W1 (black), W1.025 (red) and W1.05 (blue) PCWs with coupled L13 PC microcavity. Resonant mode A in each case is indicated by dotted lines. Group index is plotted and magnitude at the coupling frequency indicated in respective colors

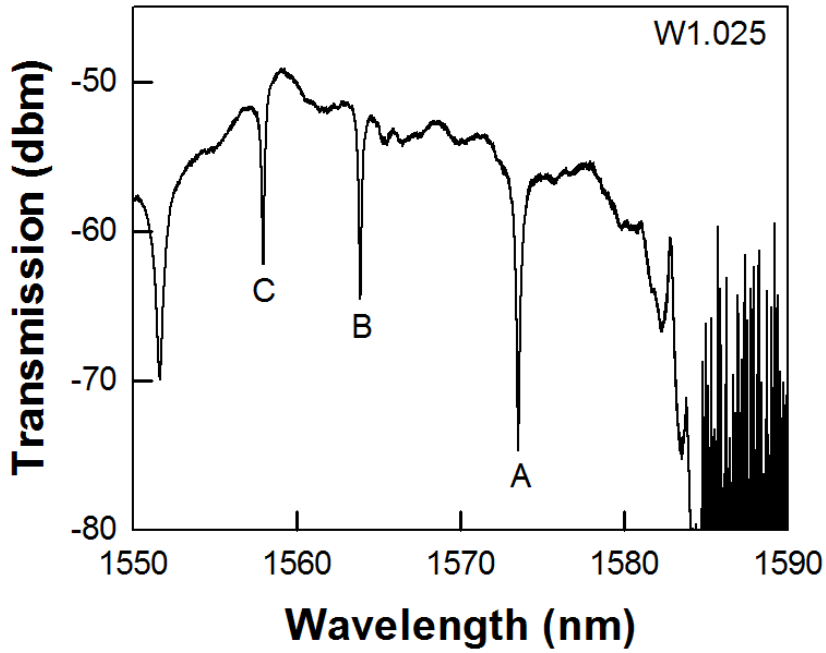

(a)

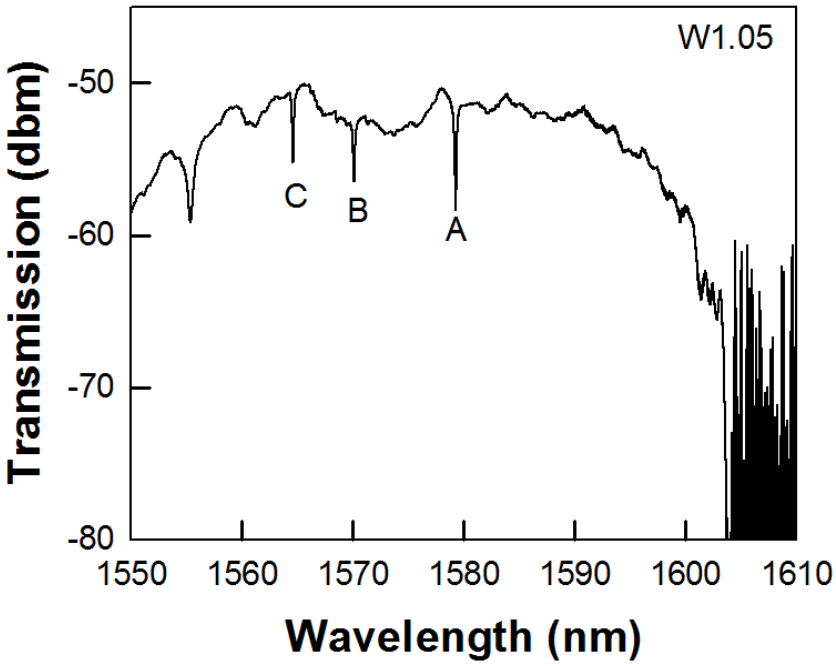

(b)

Figure 5.5: (a) W1.025 and (b) W1.05 PCW experimental transmission spectra with coupled L13 PC microcavity

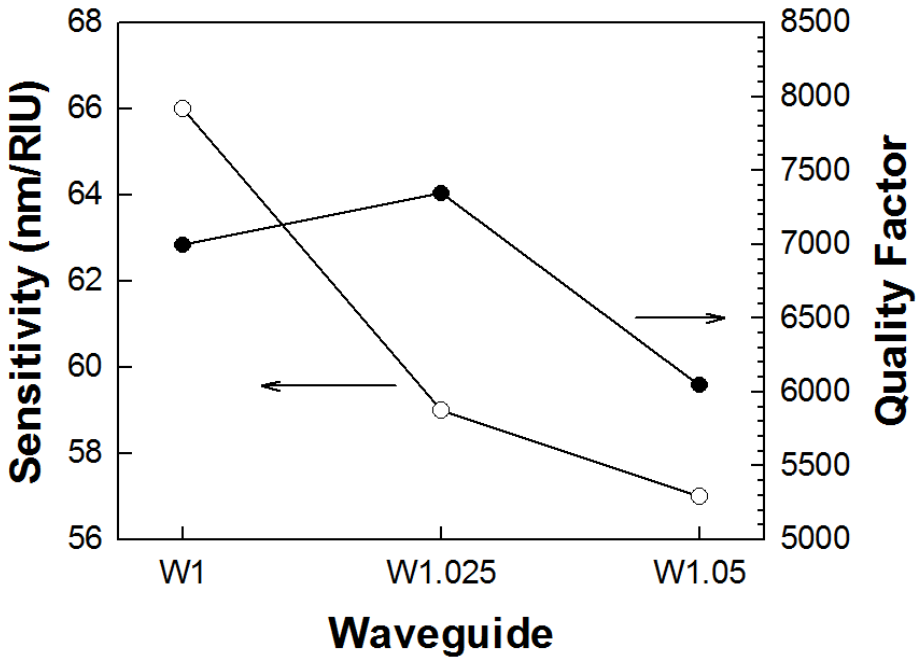

Figure 5.6: Q-factor in water and bulk sensitivity comparison of resonance mode A in each PCW in Figure 5.4.

Of course, a higher η leads to lower Q_{WG}. A lower Q_{WG} would reduce the effective Q, which would reduce the sensitivity to detect small changes in concentrations due to the broader linewidth of the resonance mode. Hence, methods to improve Q_{WG} include moving the resonance cavity farther away from the W1 PCW while at the same time, balancing the sensitivity to arrive at an optimized design with maximum slow light contribution. We also note that increasing slow light contribution to sensitivity also requires that slow light engineering minimizing reflection losses be performed at input

and output interfaces of the PCW with ridge waveguides for high signal-to-noise ratio in measurements as we have demonstrated earlier [7].

5.4 SUMMARY

In summary, we demonstrated that in side coupled PC cavity-waveguide sensors, in addition to the Q of the uncoupled PC microcavity and optical mode overlap with analyte, slow light in the coupled PCW also contributes to the enhanced sensitivities of resonance modes. The authors acknowledge the National Cancer Institute for supporting this work under the SBIR program (Contract # HHSN261201000085C). WCL, YZ and RTC acknowledge AFOSR MURI (Contract # FA9550-08-1-0394).

5.5 REFERENCES

[1] M. Iqbal, M.A. Gleeson, B. Spaugh, F. Tybor, W.G. Gunn, M. Hochberg, T. Baehr-Jones, R.C. Bailey, L.C. Gunn, IEEE J. Sel. Top. Quant. Electron., 16(3), 654 (2010).

[2] H. Sipova, S. Zhang, A.M. Dudley, D. Galas, K. Wang, J. Homola, Anal. Chem., 82, 10110 (2010).

[3] V. M. N. Passaro, F. Dell'olio, C. Ciminelli, M. N. Armenise, Sensors, 9, 1012-32 (2009)

[4] A. Densmore, M. Vachon, D.X. Xu, S. Janz, R. Ma, Y.H. Li, G. Lopinski, A. Delage, J. Lapointe, C.C. Luebbert, Q.Y. Liu, P. Cheben, J.H. Schmid, Opt. Lett., 34(23), 3598 (2009).

[5] W.-C. Lai, S. Chakravarty, Y. Zou, R. T. Chen, Opt. Lett, 37, 1208-10 (2012)

[6] Y. Zou, S. Chakravarty, W.-C. Lai, C.-Y. Lin, R. T. Chen, Lab on a chip, 12, 2309-12 (2012)

[7] S. Chakravarty, Y. Zou, W-C. Lai, R. T. Chen, Biosens. and Bioelectron, 38(1), 170-176 (2012).

[8] T. F. Krauss, Journal of Physics D: Appl. Phys. Lett, 40, 2666-2670 (2007)

[9] X. Wang, C.-Y. Lin, S. Chakravarty, J. Luo, A. K.-Y. Jen, R. T. Chen, Opt. Lett., 36, 882-884 (2011)

[10] W.-C. Lai, S. Chakravarty, X. Wang, C. Lin, R. T. Chen, Appli. Phys. Lett. ,98, 023304 (2011).

[11] W.-C. Lai, S. Chakravarty, X. Wang, C. Lin, R. T. Chen, Opti. let., 36, 984-6 (2011).

[12] S. Rahimi, A. Hosseini, X. Xu, H. Subbaraman, R.T. Chen, Opt. Express, 19(22), 21832 (2011).

[13] D. Dorfner, T. Zabel, T. Hurlimann, N. Hauke, L. Frandsen, U. Rant, G. Abstreiter, J. Finley, Biosens. and Bioelectron., 24, 2688 (2009).

Chapter 6: Photonic Crystal Microcavity Structure Waveguide for Bio-sensing

6.1 INTRODUCTION

In recent years, integrated optical devices are being developed to function as microarrays for chemical and biological assays. Platforms based on ring resonators [1], wire waveguides [2] and surface plasmon resonance (SPR) [3] have been investigated. The detection principle in all instances is based on the specific binding of the biomolecule of interest to its specific conjugate biomolecule receptor bound to the optical device substrate, which causes a change in the refractive index and hence a change in the transduced signal. While it is possible to design sensors with ultra-small mode volumes [4], current bio-molecule patterning technologies limit the minimum spacing between resonators in an array when each sensor is coated with a unique biomolecule receptor. Ink-jet printing techniques [5] enable denser integration than methods using microfluidic channels where laminar flow considerations make miniaturization challenging below 100μm for effective biomolecule patterning [2].

Photonic crystals (PCs) are a relatively new platform that have generated significant interest over the last decade due to their ability to confine light to ultra-small mode volumes and their high sensitivity to changes in refractive index of the ambient that promises the potential for creating high-density microarrays. Various designs of PC microcavities have been proposed for chemical [6] and bio-sensing [7] using microcavities with small mode volumes. Radiation losses, however, increase with

increasing refractive index of the ambient that significantly reduces the resonance quality (Q) factor due to reduced out-of-plane confinement in two-dimensional PCs. Thus, although high Q-factors have been demonstrated in freely suspended PC membranes in air [4], which promises the potential for highly sensitive sensing in air, when such membranes are suspended in phosphate buffered saline (PBS) (refractive index n = 1.334), a typical ambient for bio-molecules, Q-factors deteriorate by orders of magnitude. Hence researchers have attempted optimum designs balancing two contradictory requirements: increasing the Q-factor of the resonance versus increasing the wavelength shift due to change in refractive index. In passive silicon PC nanostructures, the transmission drop-resonance architecture has been used predominantly with hexagonal [7] and linear PC microcavity coupled to a W1 photonic crystal waveguide (PCW). The best results have been achieved in freely suspended membranes, [8] which are fragile structures. In this chapter, we present high-Q PC microcavities in silicon nano-membrane on insulator structures for bio-sensing microarray applications. Since radiation losses are inversely proportional to the cavity size and due to fundamental biomolecule patterning limitations in microarrays, we investigate methods to increase device sensitivity by increasing the size of the PC microcavity while still retaining the compactness of PC structures.

6.2 DEVICE STRUCTURE

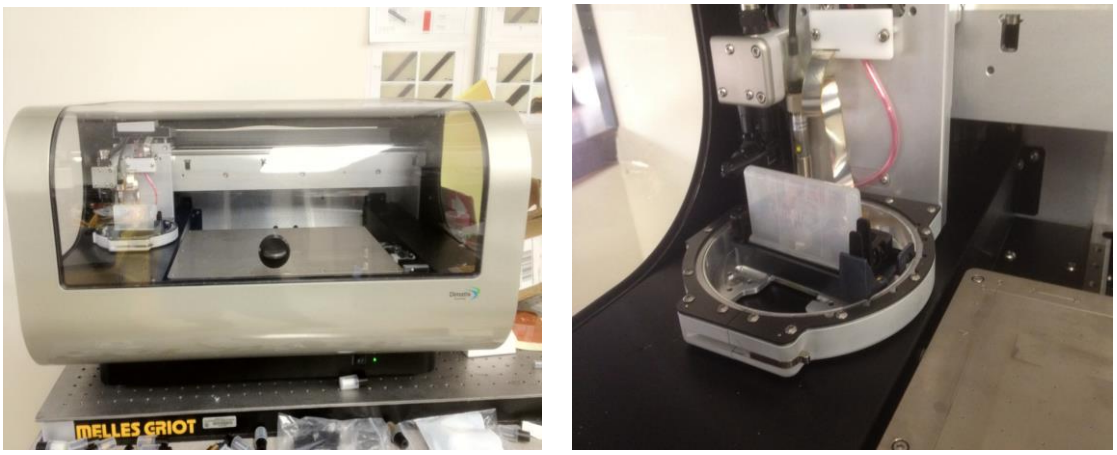

Figure 6.1: Ink jet printer and its cartridge. We can replace the cartridges with the different biomaterials that we need.

The PCW is a hexagonal structure with a W1 line defect waveguide with uniform lattice constant a=400nm, where W1 denotes that width of the PCW is $\sqrt{3}a$. Silicon slab thickness and air hole diameter are h=0.58a and d=0.54a as shown in Figure 6.2 (a).A microscope image of a patterned device with an array of two PC microcavities is shown in Figure 6.2(b). Detailed characteristics of the arrayed device are under evaluation and will be covered in another publication. In this chapter, we consider single PC microcavity sensors only. In Figure 6.2(b), we note that by ink-jet patterning, the minimum dispensed spot size of biomolecules is $\sim 35\mu m$. The ink-jet dispensed spot size determines the minimum spacing between adjacent sensors, and is different from the device surface area that can be functionalized by combining lithographic patterning with ink-jet printing as in Figure 6.1 [5]. PC microcavities of gradually increasing length were thus investigated to characterize resonance line-widths and sensitivity.

Linear PC microcavities L_n where n presents the number of missing holes along Γ–K direction, are fabricated two periods away from the PCW. The edge air holes are shifted in the Γ–K direction by 0.15*a* [4]. Figure 6.2(c) shows a band structure obtained by three-dimensional plane-wave expansion simulations of the W1 PCW, considering water (*n*=1.33) as the ambient. The normalized resonance frequencies of different PC microcavities of increasing lengths obtained by 3D finite-difference time domain simulations are indicated by dotted lines in Figure 6.2(b). The resonant mode profiles are shown in the insets.

6.3 MEASUREMENT RESULTS

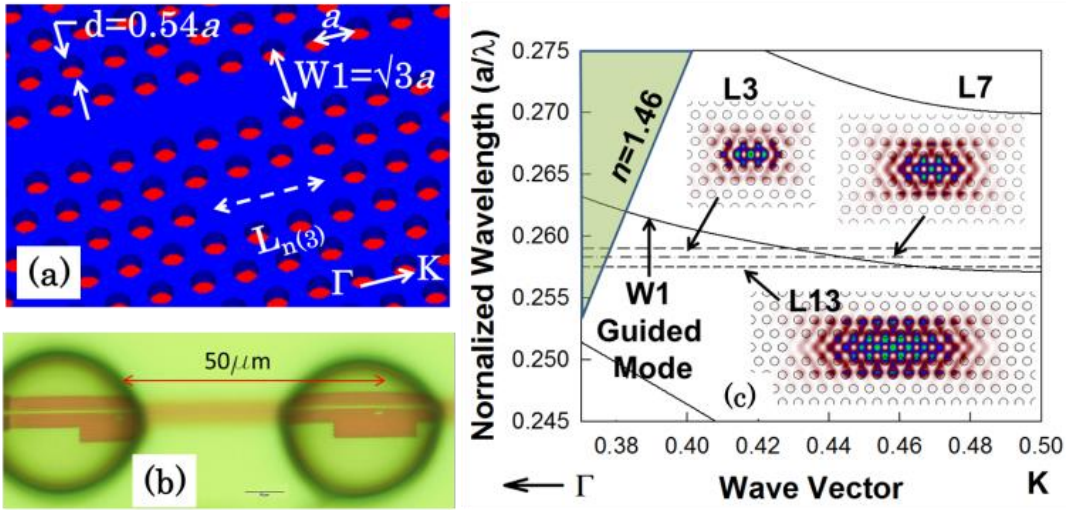

Figure 6.2: (a) Device schematic (b) Ink-jet printed biomolecules on PC devices showing spacing between printed spots (scale bar is 10μm) (c) Dispersion diagram of W1 PCW in water. The W1 guided mode is shown together with frequencies of resonant modes for L3, L7 and L13 PC microcavities by dashed lines. Respective mode profiles are shown in insets.

Light is guided in and out of the PCW by ridge waveguides with PC group index taper to enable high coupling efficiency into the slow light guided mode [9]. Devices were fabricated on silicon-on-insulator (SOI) wafer using established methods [9]. The bottom cladding of silicon dioxide (n=1.46) is kept intact to enable robust devices with high yield. Devices were tested with TE-polarized light by end-fire coupling method with polarization maintaining single mode tapered lensed fibers. The transmission drop resonance Q and sensitivity to bulk refractive index changes are analyzed with water and isopropyl alcohol (IPA) (n=1.377) as the ambient medium. Figures 6.3 (a)-(c) show experimental transmission spectra from W1 PCWs with coupled L3, L7 and L13 PC microcavities in water. In Figures 6.3 (d)-(f), drop transmission of the resonance closest

to the band edge, as in insets of Figure 6.2(b), for L3, L7 and L13 PC microcavities in water and IPA are shown.

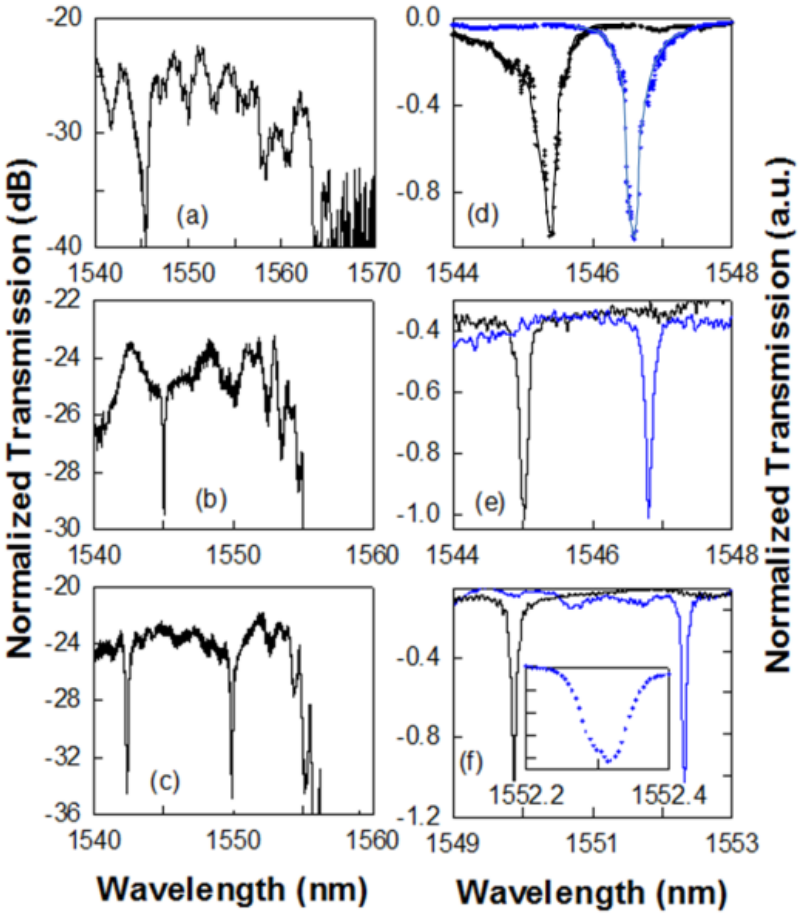

Figure 6.3: Experimental W1 PCW transmission spectrum in water with coupled (a) L3 (b) L7 and (c) L13 microcavities. Experimental spectra showing shift of resonance mode closest to the band edge in (a), (b) and (c) in (d), (e) and (f) respectively in water (black) versus IPA (blue). (inset (e)) magnifies the wavelength range.

Figure 6.4 shows resonance shifts $\Delta\lambda$ observed experimentally with the device in water versus in IPA. Figure 6.4 also plots experimental Q $(=\lambda/\Delta\lambda)$ in water and IPA, at the center frequency, and the approximate resonance offset $\Delta\Lambda$ from the W1 transmission

band edge. It is observed from Figure 6.4 that as the resonance moves closer to the band edge of the W1 PCW, Q and $\Delta\lambda$ increase. Since IPA does not absorb in the wavelength range studied, Q in IPA is higher than in water.

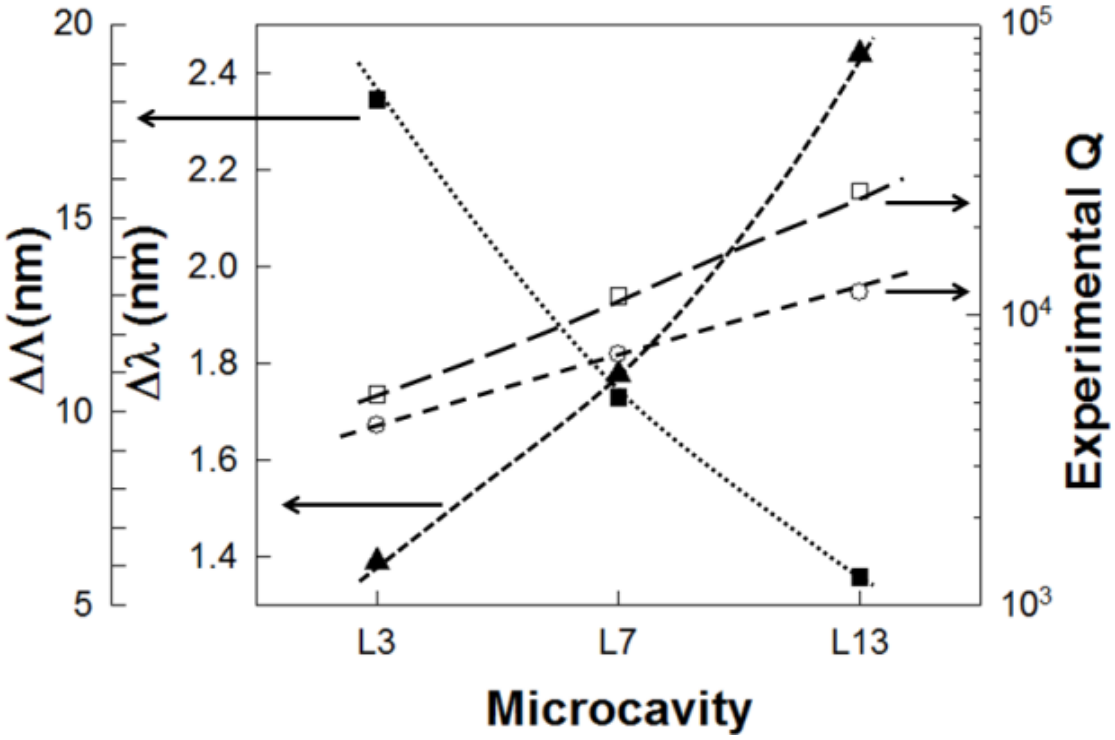

Figure 6.4: Plots showing trends in L3, L7 and L13 PC microcavities for resonant mode (a) quality factor in water (open circle) (b) quality factor in IPA (open square) (c) approximate mode offset from the transmission band edge (filled square, left offset axis) and (d) wavelength shift from water to IPA (filled triangle, left axis).

The increase in Q as the resonance approaches increasing group index near the band edge, is due to the combined effect of cold cavity Q, due to the inverse dependence of radiation loss on cavity size, and the diverging waveguide density of states [10] in the coupled cavity-waveguide system as the resonance moves deeper into the photonic band gap. Due to increase in mode volume, the resonance mode overlaps with more air holes along the borders of the cavity, leading to higher $\Delta\lambda$. By microcavity engineering, the highest Q~26760 was observed in a L13 PC microcavity in a SOI device with sensitivity

S ~52nm/RIU (RIU=refractive index unit). S is calculated as $S=\Delta\lambda/\Delta\nu$ from values in water and IPA. Similar sensitivities were achieved in single-period resonators in SOI with Q ~450 [11]. The high Q in our device improves measurement resolution for the detection of smaller changes in concentration.

The enhanced sensitivity and resolution is next applied to bio-sensing. Wafers were functionalized by treating with 1mg/mL poly-L-lysine in water, followed by washing 3 times in PBS. Wafers are next incubated in 1% glutaraldehyde in PBS for 5 minutes, ink-jet printed with target antibodies (Abs) and washed 3 times in PBS. 60μl of probe Ab was directly dispensed from a micro-pipette. The diameter of the dispensed spot on silicon is ~8mm.

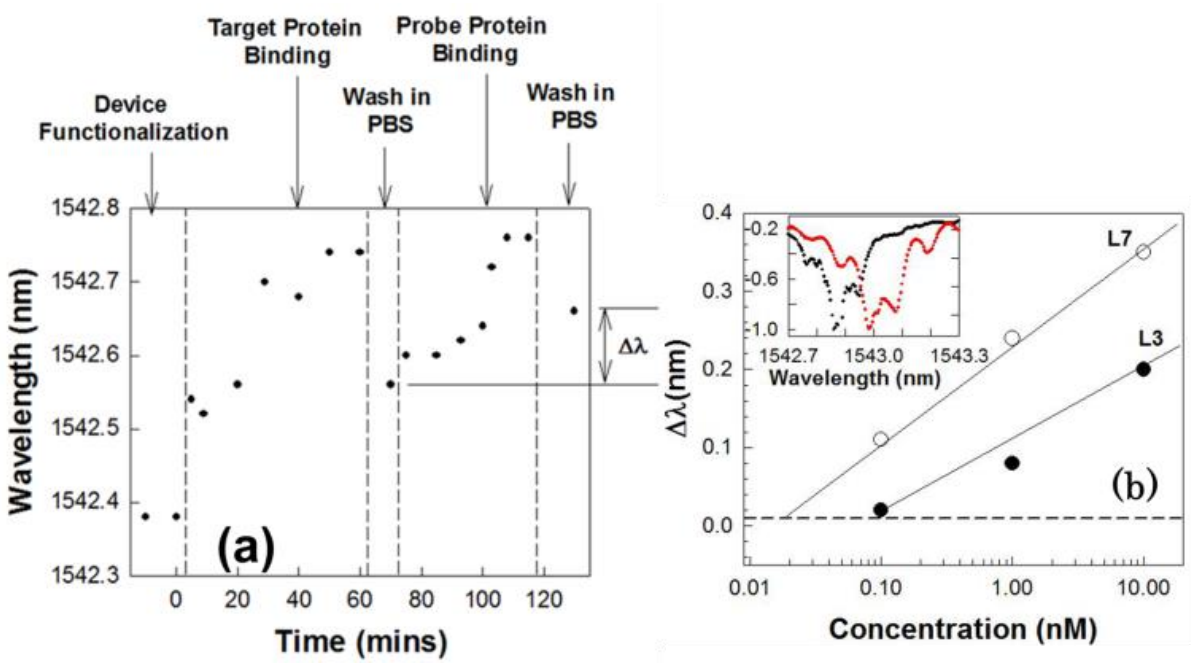

Figure 6.5: (a) Resonance wavelength of L3 PC microcavity at different steps in the binding sequence. The resonant wavelength shift of interest is denoted by $\Delta\lambda$. (b) Resonance shift of L3 (filled circles) and L7 PC microcavities (open circles) with probe antibody binding. Dashed line indicates the detection limit. Inset shows peak wavelength shift on binding. (inset) Normalized intensity data shows shift in L7 microcavity resonance from black to red curve upon addition of 0.1nM probe antibodies.

Instead of the final resonance shift as in Ref. [12], after each new concentration of probe Ab, the devices are washed in PBS and the resonance wavelength measured. While surface binding of target Ab can also be used to characterize device sensitivity, the resonance wavelength shift of interest for such hybrid assays is shown by $\Delta\lambda$ in Figure 6.5(a) which measures the probe antigen containing the predefined spectral response that is specifically bound to the target Ab. In Figure 6.5(b), the magnitude of resonance shift

as a function of rabbit anti-goat (molecular weight MW=150kDa) binding to goat Abs and Rat monoclonal Ab (MW=150kDa) binding to Human IL-10 Abs is plotted for L3 and L7 microcavities respectively. As in chemical sensing, higher Q ~7300 and larger sensitivity is observed for L7 than L3 PC microcavities. This represents the highest Q reported for bio-sensing in SOI PC devices. The spectral shift when 0.1nM of Rat monoclonal Ab is added is shown in the inset. We experimentally detected binding of 0.1nM or 15ng/ml of probe Ab with L7 devices. Since $dn/dT=1.87\times10^{-4}$ at 295K for silicon, if we consider a maximum variation of 1K in temperature, the biomolecule sensing measurement limit of the shift $\Delta\lambda$ is 0.01nm from the measured bulk sensitivity. The extrapolated concentration detection limit with L7 devices is thus ~20pM. In Figure 6.2(c) inset, with a sensing area ~6.2μm^2, (integrating over an area where the E-field intensity is more than 50% of maximum value and including the internal surface area of holes) [13], dispensed probe Ab volume of 60μl over a diameter 8mm, and assuming uniform surface coverage, the estimated mass detection limit, without considering unbound Abs that are washed away, in L7 devices is ~10.6 atto-grams. The detection limit for surface density is ~22pg/mm^2 which compares quite favorably with detection limits of 1pg/mm^2 in SPR, on more than 4 orders of magnitude smaller area [3]. The detection limit also compares favorably with 60pg/mm^2 estimated in Ref. [12]. Experimentally, we detected 110pg/mm^2 of bound antibody. Actual bound mass will be much lower since a significant fraction is washed away. It is also expected that L13 devices will show higher sensitivity to bound antibody due to the larger mode overlap with surrounding air holes. Further measurements are in progress.

6.4 SUMMARY

In summary, we demonstrated a method for bio-sensing coupling high quality factor resonance and high sensitivity in SOI PC devices. The wave-guiding nature of our device enables denser chip-scale miniaturization than SPR microarrays, and the ability to probe multiple devices simultaneously for high throughput measurements.

6.5 REFERENCES

[1] M. Iqbal, M.A. Gleeson, B. Spaugh, F. Tybor, W.G. Gunn, M. Hochberg, T. Baehr-Jones, R.C. Bailey, L.C. Gunn, IEEE J. Sel. Top. Quant. Electron., 16(3), 654 (2010).

[2] A. Densmore, M. Vachon, D.X. Xu, S. Janz, R. Ma, Y.H. Li, G. Lopinski, A. Delage, J. Lapointe, C.C. Luebbert, Q.Y. Liu, P. Cheben, J.H. Schmid, Opt. Lett., 34(23), 3598 (2009).

[3] H. Sipova, S. Zhang, A.M. Dudley, D. Galas, K. Wang, J. Homola, Anal. Chem., 82, 10110 (2010).

[4] Y. Akahane, T. Asano, B-S. Song, S. Noda, Nature, 425, 944 (2003).

[5] C.P. Tan, B.R. Cipriany, D.M. Lin, H.G. Craighead, Nano Lett, 10, 719-725 (2010).

[6] S. Chakravarty, J. Topoľančik, P. Bhattacharya, S. Chakrabarti, Y. Kang, M.E. Meyerhoff, Opt. Lett., 30, 2578 (2005).

[7] M. Lee, P.M. Fauchet, Opt. Express, 15, 4530-4535 (2007).

[8] C. Kang, C.T. Phare, Y.A. Vlasov, S. Assefa, S. M. Weiss, Opt. Express, 18(26), 27930 (2010).

[9] C-Y. Lin, X. Wang, S. Chakravarty, B-S. Lee, W-C. Lai, R.T. Chen, Appl. Phys. Lett., 97 (18), 183302 (2010)

[10] E. Waks, and J. Vuckovic, Opt. Express 13(13), 5064 (2005).

[11] S. Pal, E. Guillermain, R. Sriram, B.L. Miller, P.M. Fauchet, Biosens. and Bioelectron., 26, 4024 (2011).

[12] M.G. Scullion, A. Di Falco, T.F. Krauss, Biosens. and Bioelectron., 27, 101 (2011).

[13] D. Dorfner, T. Zabel, T. Hurlimann, N. Hauke, L. Frandsen, U. Rant, G. Abstreiter, J. Finley, Biosens. and Bioelectron., 24, 2688 (2009).

Chapter 7: Photonic Crystal Microcavity Structure Waveguide for Cancer Cell Detection with Sandwich Assay

7.1 INTRODUCTION

Microarrays based on label-free on-chip optical biosensors [1-4] are very attractive since they avoid complex chemistries caused by steric hindrance of labels. In addition, another driving factor of chip-integrated technologies is the miniaturization that can be achieved towards the ultimate goal of personalized diagnostic assays for the detection of various toxins or biomarkers of disease, in particular, for cancers and allergens in the field of medicine. Surface plasmon resonance (SPR) biosensors by Biacore[3], and the BIND platform from SRU Biosystems [4] based on one-dimensional gratings in polymer substrates represent two technologies that have achieved commercial success. However, the size of the sensors in each case provides room for significant miniaturization. In recent years, devices based on two-dimensional photonic crystals in silicon[5-9], have shown the ability to confine and guide slow light on length scales of the wavelength of light leading to high sensitivity as well as miniaturization into compact sensors for chemical[9] and bio-sensing[5-8]. A concern still remains regarding the specificity of the label-free interaction that is transduced into an optical signal. The specificity can be achieved by a statistical determination based on the results from multiple sensor spots as well as via sandwich assays. We have recently demonstrated that high sensitivity photonic crystal microcavity sensors can be arrayed on a chip and all sensors can be interrogated simultaneously by a single measurement using interconnecting on-chip

waveguides that enables redundant measurements in multiple locations to be performed at the same instant of time[10]. In addition, in this chapter we present, to our knowledge, the first demonstration of nanophotonic sandwich assays on the photonic crystal biosensor platform for the detection of a biomarker from cancer cell lysates, in this case, from lung cancer. Both methods can then be combined to verify the specificity of label-free binding interactions in a high-sensitivity silicon photonic crystal platform.

Primary lung cancer develops from epithelial cells lining the airways of the lung. Normal epithelial cells form a crucial barrier between the internal and external environments that prevents potentially dangerous materials (such as gut contents) from intruding into vital tissues. In the lung, the epithelial lining of airways prevents leakage and loss of blood while assisting with diffusion and exchange of O_2 and CO_2. Exposure to airborne particles and toxins, especially those found in cigarette smoke, leads to genetic changes in lung epithelial cells. Accumulating genetic changes underlie pathological alterations in the lung epithelium that are believed to progress from hyperplasia and dysplasia to carcinoma *in situ* and frank cancer. As such tumors grow, they outstrip supplies of blood and oxygen and become stressed. Stress along with additional host factors induce the epithelial-mesenchymal transition (EMT), a process by which cells switch their epithelial gene expression patterns to a mesenchymal phenotype with increased migratory and invasive properties. Junctional complexes are suppressed by the EMT, and the well behaved epithelial cell sheet falls apart. A facile method for detection of the EMT state of any tumor sample would have major importance both clinically and for basic science investigations. We and others have shown that ZEB1 and ZEB2 have a

prominent role in controlling the EMT process in lung cancer[11-12]. In this chapter, we present proof-of-concept data that validate the ability of photonic crystal microcavity sensors to detect ZEB1 specifically via sandwich assays with high sensitivity.

7.2 DEVICE STRUCTURE

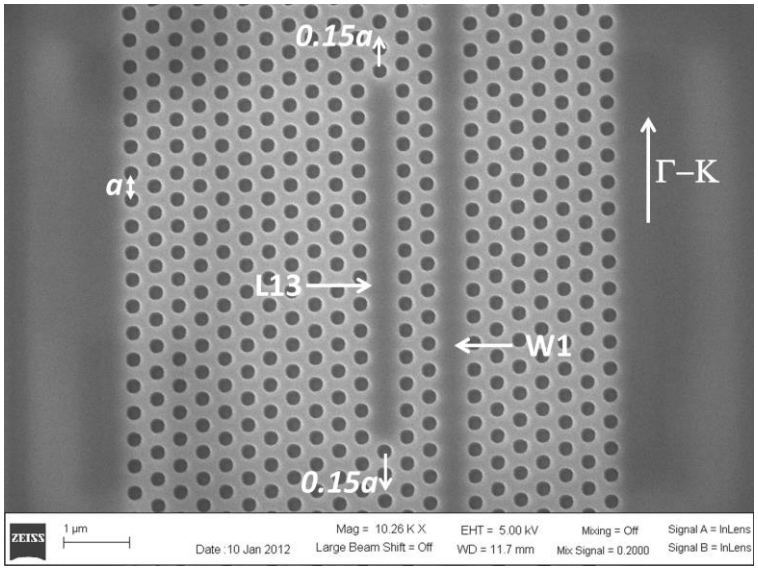

(a)

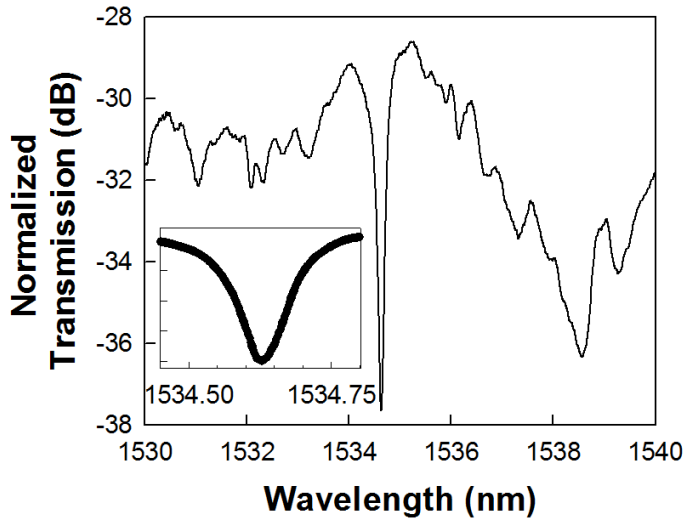

(b)

Figure 7.1: (a) Scanning electron micrograph (SEM) image showing L13 PC microcavity coupled to a W1 PC waveguide. (b) Fiber-to-fiber normalized experimental output transmission spectrum of W1 PCW in (a) showing band edge at 1538nm and L13 PC microcavity resonance mode at 1534nm. (inset) magnifies the resonance frequency range.

The device is a photonic crystal waveguide formed by removing a complete row of air holes in a uniform triangular lattice of air holes in silicon on a silicon-on-insulator (SOI) substrate. The photonic crystal waveguide (PCW) is a W1 line defect waveguide with uniform lattice constant a=400nm, where W1 denotes that the width of the photonic crystal waveguide is $\sqrt{3}a$. Silicon slab thickness and air hole diameter are h=0.58a (232nm) and d=0.5775a (231nm). Linear L13 PC microcavities with 13 missing holes along Γ–K direction, as shown in Figure 7.1(a), are fabricated two periods away from the photonic crystal waveguide. The edge air holes, as indicated in the figure, are shifted outward[13] in the Γ–K direction by 0.15a (60nm). A thin layer (~5-10nm) of silicon dioxide remains on silicon during device fabrication, which is functionalized to bind probe capture biomolecules to the device surface. For initial characterization, the probe capture biomolecules are dispensed on top of the functionalized photonic crystal microcavity with a micro-pipette. Details of the device simulation including the PC microcavity, PC waveguide, methods to enhance wideband coupling efficiency to access ridge waveguides and silicon device fabrication have been covered elsewhere[14]. Our PC microcavity sensor was designed considering that eventually, in the biomolecule microarray, the probe capture biomolecules will be dispensed by ink-jet printing. In ink-jet printing, the diameter of the ink-jet dispensed spot, which is approximately 35μm as we have demonstrated earlier, and not the size of the sensor and nor the size of the lithographically patterned biomolecule spot after ink-jet printing[7], determines the minimum spacing between adjacent unique sensors that can be achieved in a microarray. Resonances in L13 PC microcavities such as the high Q~26,760 in SOI structures[8] have

been characterized previously. We experimentally demonstrated bio-sensing sensitivity down to 0.67nanograms/ml, surface mass sensitivity of 0.8picograms/mm^2 on a sensing surface area of 11μm^2, that compares extremely favorably with 1pg/mm^2 sensitivity in SPR devices [14].

Due to the aforementioned practical engineering limitation as well as the physical advantages of higher Q possible in longer PC microcavities due to the combined effects of lower radiation loss as well as higher stored energy due to larger mode volume, we went counter to current trends in photonic crystal sensor research, and designed photonic crystal microcavities that were slightly larger than L3-type usually studied. In addition, the larger optical mode volume of the resonance mode enables larger overlap of the optical mode with analytes that fill the 216nm holes and above the silicon surface enables higher sensitivity. Highest sensitivity[14] was achieved in silicon-on-insulator (SOI) structures at a biomolecule concentration of 0.1μg/ml.

A typical transmission spectrum of the W1 PCW studied here with coupled L13 PC microcavity covered with probe capture antibody, the device being immersed in phosphate buffered saline (PBS), is shown in Figure 7.1(b). The transmission spectrum is normalized to the fiber-to-fiber transmission data. The resonance mode is at 1534.6nm with ~8dB extinction ratio and is offset 8nm from the band edge at 1542nm. The experimentally confirmed Q-factor in SOI is approximately 13,000 as obtained as $\lambda/\Delta\lambda$ from Figure 7.1(b) inset.

The items we acquired for lung cancer cell lysate detection are as follows: anti-MYC 9E10 (Sigma Aldrich, Cat #: A3833 MYC – tag 9E10), anti-ZEB1 (Santa Cruz,

Cat #: sc-25388), bovine serum albumin (Invitrogen, Cat #: 15561-020), 3-aminopropyl-triethoxy-silane (3-APTES) (Acros, CAS #:919-30-2), glutaraldehyde (Fischer Scientific, CAS#111-30-8).

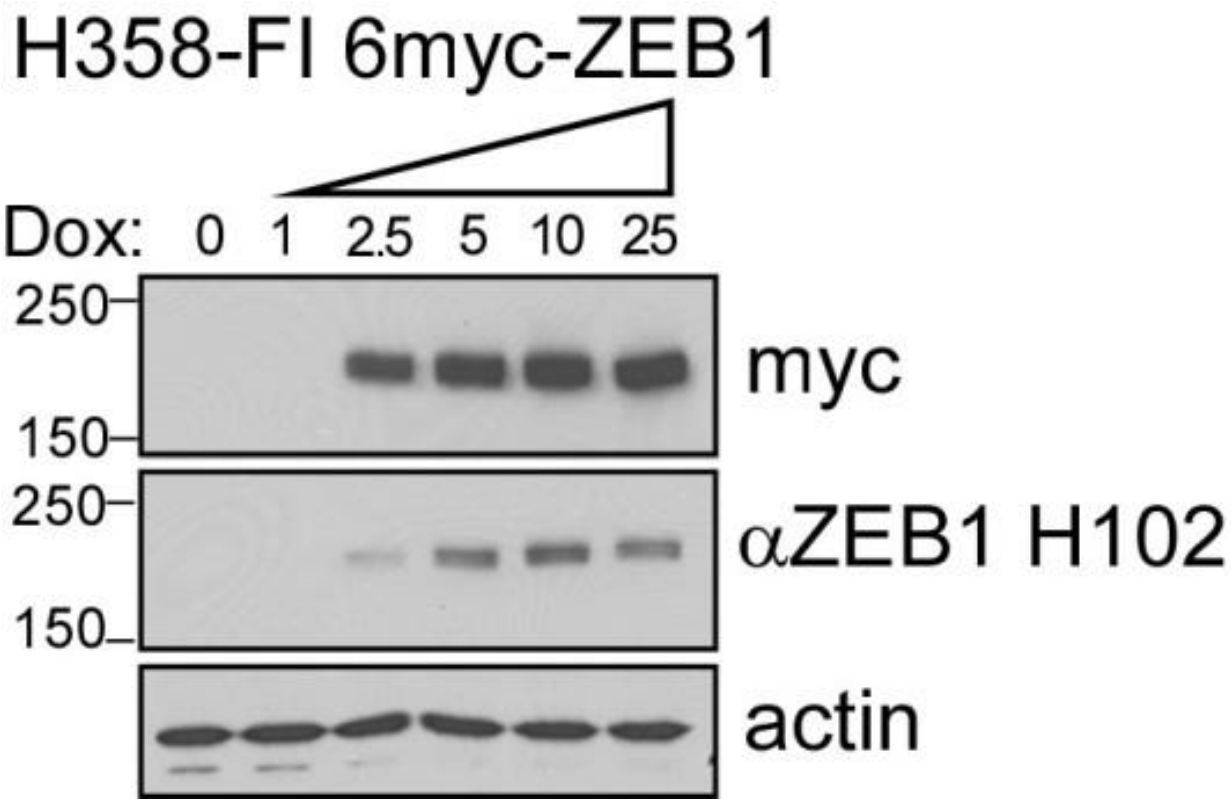

Figure 7.2: Western blot analysis of doxycycline-induced 6-myc-ZEB1 expressed in NCI-H358 cells. Cultures were treated for 3 days prior to harvest with increasing doses of dox (ng/ml), as indicated. Protein lysates (10 ug/lane) were electrophoretically separated on 4-15% gradient SDS-PAGE gels and resulting blots were probed with 9E10 to detect the 6-myc tag and H102 to detect ZEB1 epitopes. Actin showed equal loading.

The silicon surface is functionalized with 3-APTES and glutaraldehyde[10, 14-15]. Target samples were prepared from NCI-H358 lung cancer cells carrying doxycycline-

inducible 6myc-tagged ZEB1. Sample A was not induced and is henceforth called a 0-day lysate. Sample B was induced to express 6myc-ZEB1 for 3 days and is referred to as a 3-day lysate. The specific protein manipulated is ZEB1 – which has a molecular weight of about 180 KDa. For these proof-of-principle experiments, we utilized the lung cancer cell line NCI- H358, stably transfected with inducible ZEB1 whose expression is controlled with the tetraycycline derivative, doxycycline. Exogenous ZEB1 was tagged at the N-terminus with 6 copies of the MYC epitope recognized by the anti-myc antibody, 9E10. Thus 6myc-ZEB1 can be detected using either the 9E10 antibody or an antibody that binds to native ZEB1, as shown by the Western blot in Figure 2. This analysis verified that ZEB1 was strongly expressed in the dox-induced lysate and was absent from the control lysate (0 dox).

Anti-ZEB1 antibodies (H102, Santa Cruz Biotechnology) were diluted 1:1000 in PBS and dispensed above the functionalized PC microcavity. The dilution was chosen similar to that used in Western Blot studies[11-12]. After printing the anti-ZEB1 antibody, the device was washed three times in PBS to remove any unbound antibody. The device was then coated in BSA to prevent any non-specific surface adsorption and subsequently washed three times in PBS to remove unbound BSA.

7.3 MEASUREMENT RESULTS

Devices were tested with TE-polarized light by the end-fire coupling method with polarization maintaining single mode tapered lensed fibers. The target lysates were introduced in PBS which forms the top cladding. When lysates with induced ZEB1 bind to anti-ZEB1 probe capture antibodies on the PC microcavity, the conjugate specific binding causes a change in the refractive index in the immediate vicinity of the PC microcavity leading to a change in resonance frequency and hence a shift in wavelength of the dropped resonance from the transmission spectrum of the PCW. The magnitude of the shift gives a precise interpretation of the concentration of ZEB1 in the probe lysates. The resonance spectrum of the L13 PC microcavity was first measured in PBS, functionalized with probe capture anti-ZEB1. The target sample B with 3-day induced lysates made from a concentration of 10,000 cells per micro-liter was diluted to different volume concentrations in PBS to test the sensitivity of our device.

Before a new addition of sample lysate solution carrying a different concentration of target protein, the resonance wavelength was measured (λ_1). For each concentration of newly added concentration of sample lysate solution, the device was incubated in the sample lysate solution and the resonance wavelength monitored as a function of time. No resonance wavelength shift was observed for 20 minutes. After 20 minutes, the resonance wavelength increased as a function of time, until the shift saturated after another 20 minutes at λ_2. The chip was next washed 3 times in PBS to remove unbound biomolecules and the resonance wavelength λ_3 ($< \lambda_2$) measured again. The final resonance wavelength shift $\Delta\lambda$, is plotted in Fig. 3(a) given by $\Delta\lambda=\lambda_3-\lambda_1$. The same

diffusion limited time dependence of binding has been observed in previous measurements [8,10,14]. The same measurements as the sample lysates was repeated with a control PC microcavity that was covered with BSA.

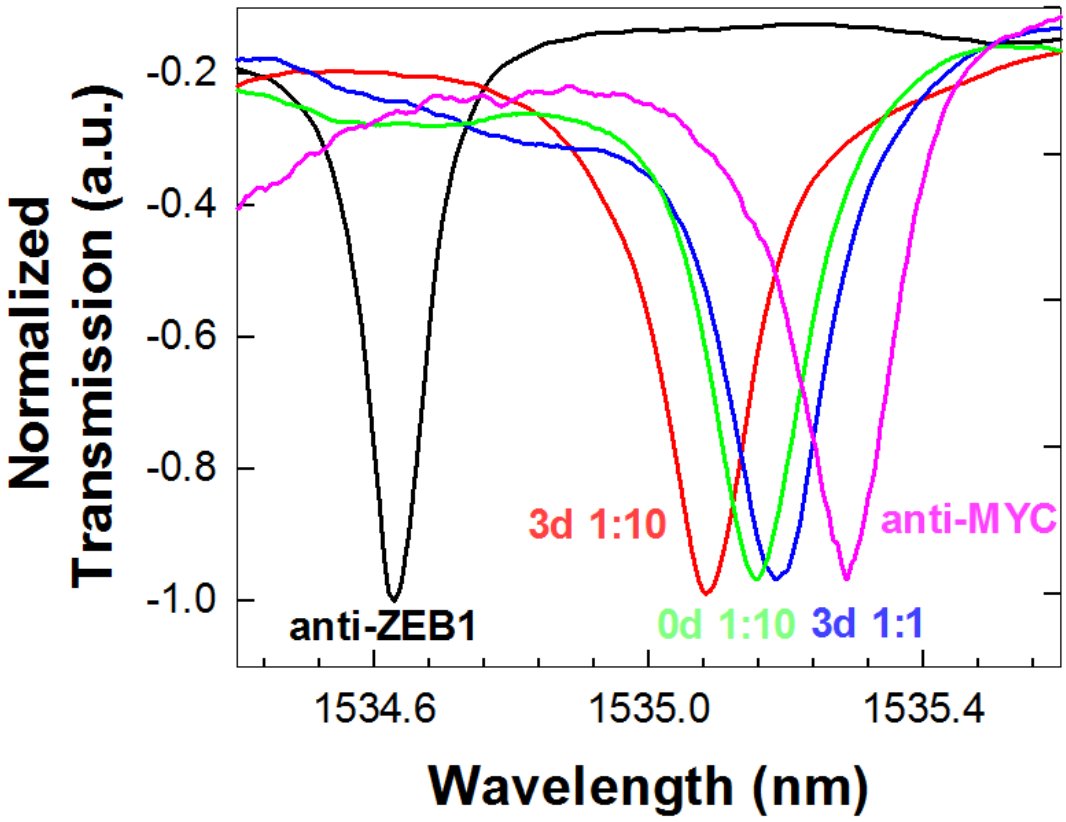

Figure 7.3: Experimental transmission spectra as a function of added sample type/concentration. The respective sample legends are color coded according to the color of the experimental spectrum. The baseline transmission spectrum with probe capture anti-ZEB1in PBS is indicated in black.

Figure 7.3 plots the experimental transmission spectra observed when 60µl volume of different concentrations of the 3-day induced target lysates were added. A resonance

wavelength shift from the anti-ZEB1 baseline (at 1543.6 nm, black trace) was observed when the 3-day induced 1:10 lysate was added (red trace). Further resonance wavelength shift was observed when a higher concentration of 3-day induced 1:1 probe lysate was added. After adding the least diluted 1:1 concentration of probe lysates, the 0-day induced lysate diluted 1:10 was added. A small negative shift was observed which was within the range of wavelength accuracy of our optical spectrum analyzer and also the range of error observed from our control experiment. Finally, to confirm that the resonance shift being observed was due to the conjugate specific binding of the induced ZEB1 in the probe sample lysate solutions and not through non-specific interactions, the secondary antibody (T2) of anti-MYC 9E10 diluted 1:1000 in PBS was added. A secondary resonance wavelength shift was observed, as shown by the pink trace in Figure 7.3. The resonance wavelength shift observed over the entire sequence of sample additions for the control PC microcavity coated with BSA is within 0.02nm which thus determines the error margin of our device. The binding specificity was thus confirmed by the control experiment combined with the sandwich assay measurement.

The BSA does show there is no detectable background of lysate proteins binding to the chip, however, it does not replace a non-specific antibody control. This is because antibodies bind to other proteins besides their antigenic target, for example, complement, which binds the Fc portion of the heavy chain. If any complement were present in the sample, there would be a binding reaction that could be difficult to distinguish from the real interaction of interest. There can also be non-specific interactions, for example, antibodies are glycoproteins and other proteins bind to glycoproteins. So while BSA is a

good control, the non-specific antibody is another important control and BSA does not replace the need for an antibody control.

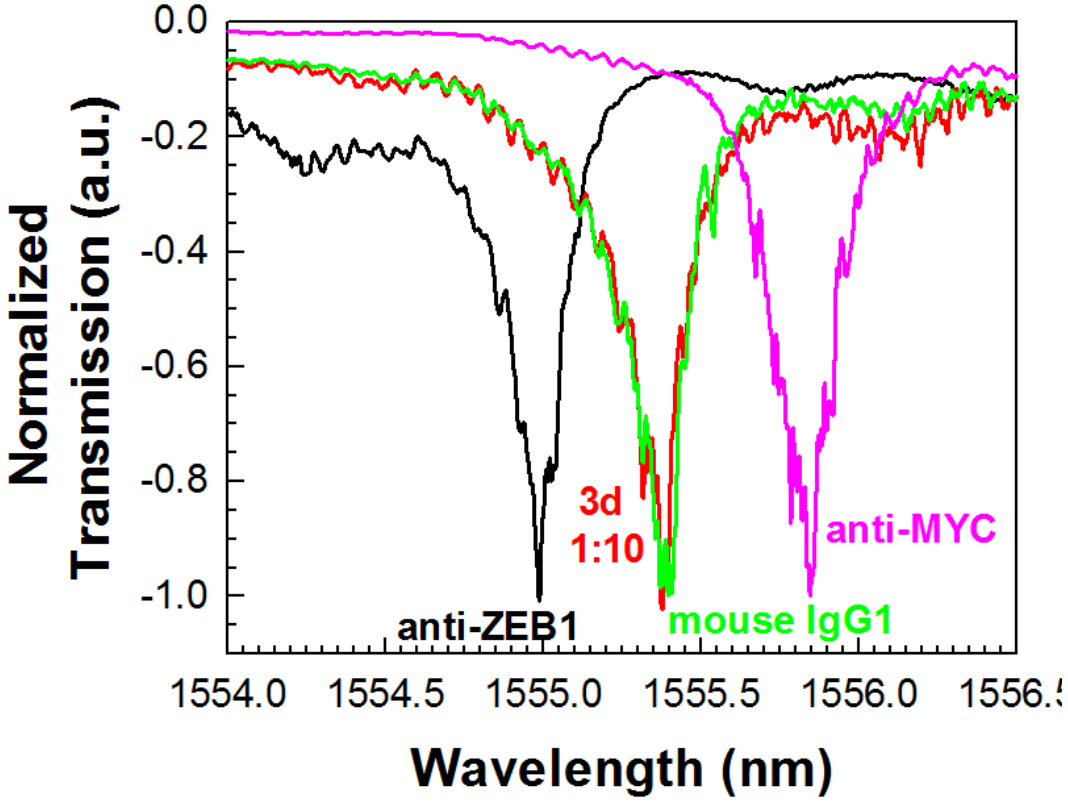

Figure 7.4: Experimental transmission spectra as a function of added sample. Sample legends are color coded according to the color of the experimental spectrum. The baseline transmission spectrum with probe capture anti-ZEB1 in PBS is indicated in black. The isotype matched comtol mouse IgG1 is in green.

Figure 7.4 shows the experimental resonance spectra for another L13 PC microcavity coated with the probe capture antibody anti-ZEB1 (diluted 1:1000 in PBS) (black trace with resonance at 1555nm). Upon addition of a 3-day 1:10 sample lysate, a resonance wavelength shift of ~0.4nm is observed (red trace) similar to Figure 7.3. An

isotype matched mouse IgG1 second antibody control (diluted 1:10 in PBS) was next added (green trace). No resonance wavelength shift is observed. The specific secondary antibody anti-MYC 9E10 (diluted 1:1000 in PBS) generates a secondary shift (pink trace) thus successfully validating the specificity of the assay.

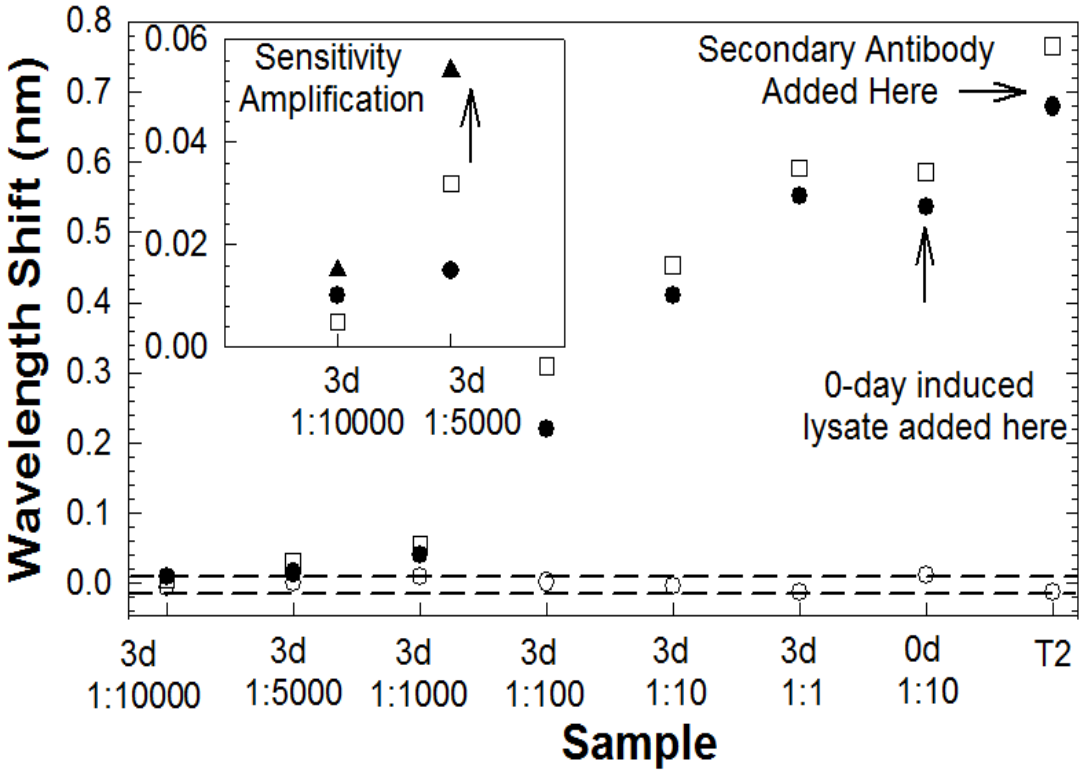

Figure 7.5: L13 PC microcavity resonance wavelength shift as a function of concentration with anti-ZEB1 primary probe capture (filled circles) and anti-MYC 9E10 primary probe capture (open squares) antibodies. The secondary antibody T2 is anti-MYC 9E10 and anti-ZEB1 respectively for data plotted with filled circles and open squares. Control BSA coated L13 PC microcavity resonance position as a function of position is plotted with open circles. (inset) Sandwich assay experiment at lowest concentration enables binding specificity verification and sensitivity amplification. Secondary anti-ZEB1 induced resonance shift indicated by filled triangles.

Figure 7.5 plots the resonance wavelength shifts as a function of concentration or type of target sample solution. To further characterize sensitivity, the probe capture and secondary antibodies were switched and the resonant wavelength shifts plotted again as a function of concentration. A larger wavelength shift is observed in each case upon

addition of the 3-day induced lysate solutions in PBS of different concentrations, when the primary probe capture antibody bound to the silicon surface is anti-MYC 9E10 versus when the primary probe capture antibody is anti-ZEB1 as in Figure 7.3. Similar higher sensitivities were observed in Western blot studies when anti-MYC 9E10 was used as the primary antibody instead of anti-ZEB1 (Figure 7.2).

In the L13 PC microcavity[14], the optical mode overlaps a surface area on the chip of 11μm^2. The dispensed 60μl probe lysate occupies a circular area with diameter 8mm. Hence, a significant fraction of the dispensed lysates are washed away and thus do not contribute to the detection. The probe lysates were prepared from 10,000 cells per microliter of NCI-H358 cells. The 1:1000 concentration at which we observed a wavelength shift of 0.07nm was prepared by mixing 60μl of the lysate solution with 60ml of PBS. 60μl of the 1:1000 lysate solution was subsequently dispensed on top of the PC microcavity. By ratio, our device detected target proteins in lysates equivalent to 10 ZEB-induced NCI-H358 cells. At the lowest concentration of 1:10,000, the wavelength shift observed was within the range of wavelength accuracy of our OSA, indicated by the dashed line in Figure 7.5 and the device was considered unresponsive to the dilution 1:10,000.

The sandwich assay technique offers the potential to further amplify the resonance wavelength shift for small concentrations. Anti-ZEB1 and anti-MYC 9E10 antibodies recognize different epitopes of the induced NCI-H358 cell lysates, but do not bind to each other. After addition of the concentration of 1:5,000 of the 3-day induced target

lysate diluted with PBS onto the functionalized silicon surface with bound primary probe capture anti-MYC 9E10, the secondary antibody anti-ZEB1 was added. The devices were washed 3 times in PBS before each addition. A resonance wavelength shift of 0.032nm was observed upon primary antibody binding with an additional wavelength shift when the secondary anti-ZEB1 antibody was added. An additional resonance wavelength shift of 0.022nm was thus observed, amplified from 0.032nm, to a total shift of 0.055nm as observed in Fig. 5 inset. When the same measurement was done with the 1:10000 dilution of 3-day induced target lysates, the total resonance wavelength shift was 0.015nm which is within the range of wavelength error 0.02nm of our measurements. The two concentrations of 1:10,000 and 1:5,000 correspond to 1 cell and 5 cells per micro-liter respectively.

The PC device comprising the L13 PC microcavity coupled to the W1 PC waveguide, with the sandwich assay, thus demonstrated the capability to specifically detect ZEB1 in 5 cells per microliter of induced NCI-H358 cell lysates.

In some respects, the biomarkers used to demonstrate the sandwich assay technique in the proof-of-concept experiments here may be considered as a type of labeling, since we have incorporated a MYC epitope which can be recognized by the anti-MYC antibody 9E10 in Western Blot tests. However, unlike sandwich ELISA methods, in which enzyme-linked antibodies are required that will bind to the detection antibody (secondary antibody as defined here) to elicit a signal for specificity confirmation, no such requirement exists in our method. Users can simply design biomarkers/antibodies, which can be secondary, tertiary or quaternary antibodies that

recognize different specific epitopes of the target cancer cell lysate, while the signal transduction is performed by the photonic crystal device. Such biomarkers are available and will be studied in the future for lung cancer detection[16-22].

7.4 SUMMARY

In summary, we have demonstrated experimentally the detection of lung cancer cell lysates with sensitivity down to 5 cells per micro-liter with photonic crystal microcavity biosensors in SOI devices. Methods to further increase the sensitivity, including optimization of the microcavity length and resonance mode quality factors, are currently being investigated. Specific detection and signal amplification was achieved by the sandwich assay principle. To our knowledge, this is the first demonstration of specific detection of lung cancer cell lysates in the label-free two-dimensional silicon photonic crystal platform using sandwich assay methods to achieve specificity as well as sensitivity amplification at low concentrations. When combined with the capabilities of multiplexed simultaneous detection enabled by chip-integrated waveguide connected layout, as we have demonstrated elsewhere[10], the device enables a significant advantage over existing technologies working towards personalized diagnostic assays, by combining multiplexing capability with sensitivity and specificity.

7.5 REFERENCES

[1] M. Iqbal., M.A. Gleeson, B. Spaugh, F. Tybor, W.G. Gunn, M. Hochberg, T. Baehr-Jones, R.C. Bailey, L.C. Gunn, IEEE J. Sel. Top. Quant. Electron. 16, 654 (2010).

[2] A. Densmore, M. Vachon, D.X. Xu, S. Janz, R. Ma, Y.H. Li, G. Lopinski, A. Delage, J. Lapointe, C.C. Luebbert, Q.Y. Liu, P. Cheben, J.H. Schmid, Optics Lett. 34, 3598 (2009).

[3] H. Sipova, S. Zhang, A.M. Dudley, D. Galas, K. Wang, J. Homola, Anal. Chem. 82, 10110 (2010).

[4] B.T. Cunningham, P. Li, S. Schulz, B. Lin, C. Baird, J. Gerstenmaier, C. Genick, F. Wang, E. Fine, L. Laing, J. Biomolecular Screening, 9(6), 481(2004).

[5] M. Lee, P.M. Fauchet, Opt. Express, 15, 4530 (2007).

[6] S. Zlatanovic, L.W. Mirkarimi, M.M. Sigalas, M.A. Bynum, E. Chow, K.M. Robotti, G.W. Burr, S. Esener, A. Grot, Sens.and Actuators. B, 13, 141 (2009).

[7] W-C., Lai, S. Chakravarty, X. Wang, C-Y Lin, R.T. Chen, Appl. Phys. Lett., 98 (2), 023304 (2011).

[8] W-C Lai, S. Chakravarty, Y Zou, R.T. Chen, Optics Lett. 37(8), Opt Lett, 37, 1208-1210 (2012).

[9] S. Chakravarty, J. Topoľančik, P. Bhattacharya, S. Chakrabarti, Y. Kang, M.E. Meyerhoff, Opt. Lett., 30, 2578 (2005).

[10] Y Zou, S. Chakravarty, W-C. Lai, C-Y. Lin, R.T. Chen, Lab-on-a-Chip, 12,2309-2312 (2012)

[11] R.M. Gemmill, J. Roche, V.A. Potiron, P. Nasarre, M. Mitas, C.D. Coldren, B.A. Helfrich, E. Garrrett-Mayer, P.A. Bunn, H.A. Drabkin, Cancer Lett. 300 (1), 66 (2011).

[12] Y. Takeyama, M. Sato, M. Horio, T. Hase, K. Yoshida, T. Yokoyama, H. Nakashima, N. Hashimoto, Y. Sekido, A.F. Gazdar, Cancer letters, 296, 216-224 (2010).

[13] Y. Akahane, T. Asano, B-S. Song, S. Noda, Nature, 425, 944 (2003).

[14] S. Chakravarty, Y. Zou,, W-C. Lai, R.T. Chen, Biosensors and Bioelectron, 43, 50-55 (2013)

[15] A. Subramanian, S.J. Kennel, P.I. Oden, K.B. Jacobson, J. Woodward, M.J. Doktycz, Enzyme and Microbial Technology, 24, 26 (1999).

[16] C.M. Choi, S.C. Yang, H.J. Jo, S.Y. Song, Y.J. Jeon, T.W. Jang, D.J. Kim, S.H. Jang, S.H. Yang, Y.D. Kim, Ann Oncol. (2012)

[17] M. Takenaka, T. Hanagiri, S. Shinohara, T. Kuwata, Y. Chikaishi, S. Oka, Y. Shigematsu, Y. Nagata, H. Shimokawa, M. Nakagawa, Anticancer Res, 31, 4631-4636 (2011).

[18] M. Tretiakova, A.K. Salama, T. Karrison, M.K. Ferguson, A.N. Husain, E.E. Vokes, and R. Salgia, J Environ Pathol Toxicol Oncol, 30, 341-354 (2011).

[19] M. Pesta, V. Kulda, R.Kucera, M. Pesek, J. Vrzalova, V. Liska, L. Pecen, V. Treska, J. Safranek, M. Prazakova, Anticancer Res 31, 4031-4038 (2011).

[20] H.J. Lee, Y.T. Kim, P.J. Park, Y.S. Shin, K.N. Kang, Y. Kim, C.W. Kim, J Thorac Cardiovasc Surg, 143, 421-427 (2012).

[21] B.C. Tong, D.H. Harpole, Jr.. Surg Oncol Clin N Am, 21, 161-175 (2012).

[22] T. Ohira, R.M. Gemmill, K. Ferguson, S. Kusy, J. Roche, E. Brambilla, C. Zeng, A. Baron, L. Bemis, P. Erickson, Proceedings of the National Academy of Sciences of the United States of America, 100, 10429-10434(2003).

Chapter 8: Summary

This doctoral dissertation describes the work in our group about the sensor projects. There are two main focuses in this dissertation: (1) Chemical sensing by using photonic crystal waveguide (PCW) structure. (2) Biological sensing by using photonic crystal microcavities structure.

We first present the PC slot waveguide structure to successfully detect the xylene in water and methane in nitrogen as examples of VOC detections, which are very important for engineers to correctly detect the contaminants in our environment. Our sensitivity of detecting xylene in water is down to 1 ppb, which is better compared to several publications in other groups. Our sensitivity of methane in nitrogen experiment also shows better sensitivity than the commercially available methane detection system, TDLAS. After we successfully detected these two chemicals, we further integrate two PC waveguides together on a single chip to detect xylene and TCE, which demonstrates the ability of multiplexed detection of two chemicals on a single chip in our system. With the using of grating couplers as our method to couple light into our multiplexed devices, we are able to achieve higher signal-to-noise ratio and detect lower sensitivity for xylene and TCE. In the future, we are going to present the packaging setup of our chip in our group, so we should be able to present a system to detect the underground water and contaminated air in our environment using the packaged chip.

Next, we present the application of PC microcavities structure in the next part of this dissertation. The resonance mode of PC microcavities structure has its significant property for detecting the interested analytes. We first investigate the quality factor and

slow light effect of these resonance modes and compare which one has the largest biological sensitivity. After the selection of the modes, we choose the mode with highest sensitivity to do the sensing for antibodies and cancer cells. In addition, we are able to detect the multiple biomaterials on a single chip by using ink-jet printer. Thus, multiple detections of biomaterials on a chip at the same time are enabled by this method.

We also present the investigation of the relation between the quality factor of resonance mode and the sensitivity for biosensing. We found the higher the quality factor, the higher the sensitivity. We also discuss the relation between slow light affected modes and sensitivity, and the higher the slow light effect, the sensitivity will be higher too.

In chapter 7, we are able to detect the different antibodies using the high sensitivity L13 mode, and we achieve a relatively high sensitivity. We also continue to use L13 PC microcavity device to do the cancer cell lysate detection and we are able to detect down to 2 cell lysates/ μl. In the future, we will work on achieving the higher sensitivity for different antibodies and cancer cell lysates. Multiplexed detection of different cancer cell lysates will also be presented and investigated in the future.

Appendix

PUBLICATIONS

[1] W.-C. Lai, S. Chakravarty, X. Wang, C. Lin, and R. T. Chen, "On-chip methane sensing by near-IR absorption signatures in a photonic crystal slot waveguide.," *Optics letters* **36**(6), 984–986 (2011).

[2] W.-C. Lai, S. Chakravarty, X. Wang, C. Lin, and R. T. Chen, "Photonic crystal slot waveguide absorption spectrometer for on-chip near-infrared spectroscopy of xylene in water," *Applied Physics Letters* **98**(2), 023304 (2011).

[3] W.-C. Lai, S. Chakravarty, Y. Zou, and R. T. Chen, "Silicon nano-membrane based photonic crystal microcavities for high sensitivity bio-sensing.," *Optics letters* **37**(7), 1208–1210 (2012).

[4] W.-C. Lai, S. Chakravarty, Y. Zou, Y. Guo, and R. T. Chen, "Slow light enhanced sensitivity of resonance modes in photonic crystal biosensors.," *Applied physics letters* **102**, 041111 (2013).

[5] W. Lai, S. Chakravarty, Y. Zou, and R. T. Chen, "Loss Engineered High Sensitivity Photonic Crystal Microcavities for Multiplexed Detection of Biomolecules," *Frontier in Optics* (2012).

[6] W.-C. Lai, S. Chakravarty, Y. Zou, and R. T. Chen, “Multiplexed selective detection and identification of TCE and xylene in water by on-chip absorption spectroscopy,” *Photonic West*,. (2013) .

[7] W.-C. Lai, S. Chakravarty, Y. Zou, H. a. Drabkin, R. M. Gemmill, G. R. Simon, S. H. Chin, and R. T. Chen, “Silicon photonic crystal microcavity biosensors for label free highly sensitive and specific lung cancer detection,” *IEEE Photonics Conference 2012* **2**, 443–444, (2012).

[8] W. Lai, K. Moncivais, S. Chakravarty, X. Wang, C. Lin, Z. J. Zhang, and R. T. Chen, “High Density Ink Jet Printing of Bio-molecules for Photonic Crystal-based Microarray Applications,” *Sensors*, 4535 (2010).

[9] S. Chakravarty, W.-C. Lai, Y. Zou, H. a Drabkin, R. M. Gemmill, G. R. Simon, S. H. Chin, and R. T. Chen, “Multiplexed specific label-free detection of NCI-H358 lung cancer cell line lysates with silicon based photonic crystal microcavity biosensors.,” *Biosensors & bioelectronics* **43**, 50–55 (2013).

[10] S. Chakravarty, W.-C. Lai, Y. Zou, R. M. Gemmill, and R. T. Chen, “Silicon photonic crystal microarrays for high throughput label-free detection of lung cancer cell line lysates with sensitivity and specificity,” *Photonic West*, (2013).

[11] Y. Zou, S. Chakravarty, W.-C. Lai, C.-Y. Lin, and R. T. Chen, "Methods to array photonic crystal microcavities for high throughput high sensitivity biosensing on a silicon-chip based platform," *Lab on a Chip* **12**, 2309–2312 (2012).

[12] Y. Zou, S. Chakravarty, W.-C. Lai, C.-C. Hsieh, and R. T. Chen, "High yield silicon photonic crystal microcavity biosensors with 100fM detection limit," *Photonic West*,B. L. Miller and P. M. Fauchet, Eds. (2013).

[13] Y. Zou, S. Chakravarty, W.-C. Lai, and R. T. Chen, "Experimental detection of 1pico-molar concentration from high-Q photonic crystal microcavity biosensors," *IEEE Photonics Conference*, Ieee (2012).

[14] L. Zhu, S. Chakravarty, C.-C. Hsieh, W.-C. Lai, and R. T. Chen, "Slow Light Waveguide and Enhanced Area Microcavity Engineering for High Sensitivity Photonic Crystal Sensors," *CLEO*, OSA, Washington, D.C. (2013).

[15] S. Chakravarty, Y. Zou, W.-C. Lai, and R. T. Chen, "Slow light engineering for high Q high sensitivity photonic crystal microcavity biosensors in silicon.," *Biosensors & bioelectronics* **38**(1), 170–176, (2012).

[16] C.-Y. Lin, B. Lee, A. X. Wang, W.-C. Lai, S. Chakravarty, Y. Liu, D. Kwong, R. T. Chen, J. Luo, et al., "Ultra-compact silicon nanophotonic modulator based on electro-optic polymer infiltrated slot photonic crystal waveguide," *Photonic West* (2010).

[17] C.-Y. Lin, A. X. Wang, W.-C. Lai, J. L. Covey, S. Chakravarty, and R. T. Chen, "Coupling loss minimization of slow light slotted photonic crystal waveguides using mode matching with continuous group index perturbation," *Optics Letters* **37**(2), 232 (2012).

[18] C.-Y. Lin, X. Wang, S. Chakravarty, B. S. Lee, W.-C. Lai, and R. T. Chen, "Wideband group velocity independent coupling into slow light silicon photonic crystal waveguide," *Applied Physics Letters* **97**(18), 183302 (2010).

[19] C.-Y. Lin, X. Wang, S. Chakravarty, B. S. Lee, W. Lai, J. Luo, A. K.-Y. Jen, and R. T. Chen, "Electro-optic polymer infiltrated silicon photonic crystal slot waveguide modulator with 23 dB slow light enhancement," *Applied Physics Letters* **97**(9), 093304 (2010).

[20] X. Wang, C.-Y. Lin, S. Chakravarty, J. Luo, A. K.-Y. Jen, and R. T. Chen, "Effective in-device r33 of 735 pm/V on electro-optic polymer infiltrated silicon photonic crystal slot waveguides.," *Optics letters* **36**(6), 882–884 (2011).

Bibliography

Chapter 1

[1] M.J. Thorpe, K.D. Moll, R.J. Jones, B. Safdi, and J.Ye, Science 311, 1595 (2006) , URL: http://www.tigeroptics.com/

[2] M. Lackner, Rev. in Chem. Engg. 23, 65 (2007).

[3] F. Adler, P. Maslowski, A. Foltynowicz, K.C. Cossel, T.C. Briles, I. Hartl, and J. Ye, Opt. Express 18, 21861 (2010).

[4] URL: http://www.tdlas.com/products/

[5] N.A. Mortensen, S.S. Xiao, Appl. Phys. Lett 90(14), 141108 (2007).

Chapter 2

[1] N.A. Mortensen, S.S. Xiao, Appl. Phys. Lett., 90(14), 141108 (2007).

[2] E. Yablonovitch, Phys. Rev. Lett., 58, 1059 (1987).

[3] S. John, Phys. Rev. Lett., 58, 2486 (1987).

[4] S.Chakravarty, P.Bhattacharya, and Z.Mi, IEEE Photon. Tech. Lett., 18, 2665 (2006).

[5] O. Painter, R.K. Lee, A. Scherer, A. Yariv, J.D. O'Brien, P.D. Dapkus, and I. Kim, Science, 284 (5421), 1819 (1999).

[6] J. Vuckovic, and Y. Yamamoto, Appl. Phys. Lett. ,82 (15), 2374 (2003).

[7] C-Y. Lin, X. Wang, S. Chakravarty, B-S. Lee, W-C. Lai, J. Luo, A. K-Y. Jen, and R.T. Chen, Appl. Phys. Lett., 97, 093304 (2010).

[8] S.Chakravarty, J.Topoľančik, P.Bhattacharya, S.Chakrabarti, Y. Kang, and M.E. Meyerhoff, Opt. Lett., 30, 2578 (2005).

[9] M. Loncar, A. Scherer, and Y.M. Qiu, Appl. Phys. Lett., 82 (26), 4648 (2003).

[10] M.R. Lee, and P.M. Fauchet, Optics Lett., 32 (22), 3284 (2007).

[11] M. Notomi, Phys. Rev. Lett., 87, 253902 (2001).

[12] A. Wang, S. Chakravarty, B-S. Lee, C. Lin, and R.T. Chen, Opt. Lett., 34(20), 3202 (2009).

[13] D.A. Burns, "Handbook of near-infrared analysis," 3rd Edition, Hoboken: Taylor and Francis Ltd (2007).

[14] J.S. Albuquerque, M.F. Pimentel, V.L. Silva, M. Raimundo, J.J.R. Rohwedder, and C. Pasquini, Anal. Chem., 77 (1), 72 (2005).

[15] K.M.G. Lima, I.M. Raimundo, and M.F. Pimentel, Sens. & Act. B-Chem., 125(1), 229 (2007).

[16] J. Burck, S. Roth, K. Kraemer, M. Scholz, N. Klaas, J. Hazard. Mater., 83, 11 (2001)

[17] A.M.F. Silva, M.F. Pimentel, I.M. Raimundo, and Y.M.B. Almeida, Vibration. Spectros., 46 (1), 39 (2008).

Chapter 3

[1] N.A. Mortensen, and S.S. Xiao, Appl. Phys. Lett, 90, 141108 (2007).

[2] E. Yablonovitch, Phys. Rev. Lett. 58, 1059 (1987); S. John, Phys. Rev. Lett., 58, 2486 (1987).

[3] S. Chakravarty, P. Bhattacharya, and Z. Mi, IEEE Photon. Tech. Lett., 18, 2665 (2006).

[4] S.Chakravarty, J.Topoľančik, P.Bhattacharya, S.Chakrabarti, Y. Kang, and M.E. Meyerhoff, Opt. Lett., 30, 2578 (2005).

[5] C-Y. Lin, X. Wang, S. Chakravarty, B-S. Lee, W-C. Lai, J. Luo, A. K-Y. Jen, and R.T. Chen, Appl. Phys. Lett., 97, 093304 (2010).

[6] M. Notomi, Phys. Rev. Lett., 87, 253902 (2001).

[7] X. Chen, W. Jiang, J. Chen, L. Gu, and R.T. Chen, Appl. Phys. Lett., 91, 091111 (2007).

[8] A. Nitkowski, L. Chen, and M. Lipson, Opt. Express., 16, 11930 (2008).

[9] W-C. Lai, S. Chakravarty, X. Wang, C. Lin, and R.T. Chen, Appl. Phys. Lett., 98, 023304 (2011).

[10] X. Wang, S. Chakravarty, B-S. Lee, C. Lin, and R.T. Chen, Opt. Lett., 34, 3202 (2009).

[11] L.S. Rothman et al, Journal of Quantitative Spectroscopy and Radiative Transfer, 110, 533 (2009).

[12] W-B. Yan, Gases and Technology, 1(4), 21 (2002).

[13] J.T. Robinson, L. Chen, and M. Lipson, Opt. Express, 16, 4296 (2008).

[14] N.A. Yebo, P. Lommens, Z. Hens, and R. Baets, Opt. Express, 18, 11859 (2010).

[15] URL: http://www.tdlas.com/products/

[16] A. Karpf, and G.N. Rao, Appl. Optics, 49, 1406 (2010).

Chapter 4

[1] M. Lackner, Rev. Chem. Eng., 23, 65 (2007).

[2] F. Adler, P. Maslowski, A. Foltynowicz, K. C. Cossel, T. C. Briles, I. Hartl, and J. Ye, Opt. Exp. 18, 218610 (2010).

[3] W.-C. Lai, S. Chakravarty, X. Wang, C. Lin, and R. T. Chen, Appl. Phys. Lett., 98, 023304 (2011).

[4] W.-C. Lai, S. Chakravarty, X. Wang, C. Lin, and R. T. Chen, Optics Lett., 36, 984–6 (2011).

[5] K.M.G. Lima, I.M. Raimundo, and M.F. Pimentel, Sens. & Act. B-Chem., 125, 229 (2007).

[6] J. Buerck, S. Roth, K. Kraemer, M. Scholz, and N. Klaas, J. Hazard. Mater., 83, 11 (2001).

[7] K. Reddy, Y. Guo, J. Liu, W. Lee, M. K. K. Oo, and X. Fan, Lab Chip, 12, 901–5 (2012).

[8] C-J. Lu, W.H. Steinecker, W-C. Tian, M.C. Oborny, J.M. Nichols, M. Agah, J.A. Potkay, H.K.L. Chan, J. Driscoll, R.D. Sacks, K.D. Wise, S.W. Pang, E.T. Zellers, Lab Chip, 5, 1123 (2005).

[9] M. Girschikofsky, M. Rosenberger, S. Belle, M. Brutschy, S. R. Waldvogel, and R. Hellmann, Sens. & Act. B: Chem., 171-172, 338–342 (2012).

[10] R. St-Gelais, G. Mackey, J. Saunders, J. Zhou, A. Leblanc-Hotte, A. Poulin, J. a. Barnes, H.-P. Loock, R. S. Brown, and Y.-A. Peter, Sens. & Act. B: Chem., 182, 45–52 (2013).

[11] M. Deng, C.-P. Tang, T. Zhu, Y.-J. Rao, L.-C. Xu, and M. Han, Appl. Optics, 49, 1593–8 (2010).

[12] Q.-Y. Cai and E. T. Zellers, Anal. Chem., 74, 3533–3539 (2002).

[13] D. Matatagui, J. Marti, M. J. Fernandez, J. L. Fontecha, J. Gutierrez, I. Gracia, C. Cane and M. C. Horrillo, Sens. & Act. B: Chem., 154, 199–205 (2011).

[14] J. Liu, Y. Sun, D. J. Howard, G. Frye-Mason, A. K. Thompson, S.-J. Ja, S.-K. Wang, M. Bai, H. Taub, M. Almasri and X. Fan, Anal. Chem., 82, 4370–4375 (2010).

[15] Mortensen, N.A., and Xiao, S.S., Appl. Phys. Lett., 90(14), 141108 (2007).

[16] M. Notomi, K. Yamada, A. Shinya, J. Takahashi, C. Takahashi, and I. Yokohama, Phys. Rev. Lett., 87, 253902 (2001).

[17] S. H. Tao, Q. Fang, J. F. Song, M. B. Yu, G. Q. Lo, and D. L. Kwong, Opt. Express, 16, 26 (2008).

[18] A.C.R. Pipino, J.P.M. Hoefnagels, and N. Watanabe, J. Chem. Phys., 120, 2879 (2004).

[19] D.A. Burns, Handbook of near-infrared analysis, 3rd Edition, Hoboken: Taylor and Francis Ltd (2007).

[20] X. Xu, H. Subbaraman, J. Covey, D. Kwong, A. Hosseini, and R. T. Chen, Appl. Phys. Lett, 101, 031109 (2012).

[21] C.-Y. Lin, X. Wang, S. Chakravarty, B. S. Lee, W.-C. Lai, and R. T. Chen, Appl. Phys. Lett., 97(18), 183302 (2010).

[22] J. Hue, M. Dupoy, T. Bordy, R. Rousier, S. Vignoud, B. Schaerer, T.-H. Tran-Thi, C. Rivron, L. Mugherli, and P. Karpe, Sens. & Act. B: Chem. (2013); http://dx.doi.org/10.1016/j.snb.2013.03.047

[23] A. Hosseini, D. Kwong, C. Lin, B. S. Lee, and R. T. Chen, IEEE J. Sel. Top. Quant. Electron, 16, 61–69 (2010).

Chapter 5

[1] M. Iqbal, M.A. Gleeson, B. Spaugh, F. Tybor, W.G. Gunn, M. Hochberg, T. Baehr-Jones, R.C. Bailey, L.C. Gunn, IEEE J. Sel. Top. Quant. Electron., 16(3), 654 (2010).

[2] H. Sipova, S. Zhang, A.M. Dudley, D. Galas, K. Wang, J. Homola, Anal. Chem., 82, 10110 (2010).

[3] V. M. N. Passaro, F. Dell'olio, C. Ciminelli, M. N. Armenise, Sensors, 9, 1012-32 (2009)

[4] A. Densmore, M. Vachon, D.X. Xu, S. Janz, R. Ma, Y.H. Li, G. Lopinski, A. Delage, J. Lapointe, C.C. Luebbert, Q.Y. Liu, P. Cheben, J.H. Schmid, Opt. Lett., 34(23), 3598 (2009).

[5] W.-C. Lai, S. Chakravarty, Y. Zou, R. T. Chen, Opt. Lett, 37, 1208-10 (2012)

[6] Y. Zou, S. Chakravarty, W.-C. Lai, C.-Y. Lin, R. T. Chen, Lab on a chip, 12, 2309-12 (2012)

[7] S. Chakravarty, Y. Zou, W-C. Lai, R. T. Chen, Biosens. and Bioelectron, 38(1), 170-176 (2012).

[8] T. F. Krauss, Journal of Physics D: Appl. Phys. Lett, 40, 2666-2670 (2007)

[9] X. Wang, C.-Y. Lin, S. Chakravarty, J. Luo, A. K.-Y. Jen, R. T. Chen, Opt. Lett., 36, 882-884 (2011)

[10] W.-C. Lai, S. Chakravarty, X. Wang, C. Lin, R. T. Chen, Appli. Phys. Lett. ,98, 023304 (2011).

[11] W.-C. Lai, S. Chakravarty, X. Wang, C. Lin, R. T. Chen, Opti. let., 36, 984-6 (2011).

[12] S. Rahimi, A. Hosseini, X. Xu, H. Subbaraman, R.T. Chen, Opt. Express, 19(22), 21832 (2011).

[13] D. Dorfner, T. Zabel, T. Hurlimann, N. Hauke, L. Frandsen, U. Rant, G. Abstreiter, J. Finley, Biosens. and Bioelectron., 24, 2688 (2009).

Chapter 6

[1] M. Iqbal, M.A. Gleeson, B. Spaugh, F. Tybor, W.G. Gunn, M. Hochberg, T. Baehr-Jones, R.C. Bailey, L.C. Gunn, IEEE J. Sel. Top. Quant. Electron., 16(3), 654 (2010).

[2] A. Densmore, M. Vachon, D.X. Xu, S. Janz, R. Ma, Y.H. Li, G. Lopinski, A. Delage, J. Lapointe, C.C. Luebbert, Q.Y. Liu, P. Cheben, J.H. Schmid, Opt. Lett., 34(23), 3598 (2009).

[3] H. Sipova, S. Zhang, A.M. Dudley, D. Galas, K. Wang, J. Homola, Anal. Chem., 82, 10110 (2010).

[4] Y. Akahane, T. Asano, B-S. Song, S. Noda, Nature, 425, 944 (2003).

[5] C.P. Tan, B.R. Cipriany, D.M. Lin, H.G. Craighead, Nano Lett, 10, 719-725 (2010).

[6] S. Chakravarty, J. Topoľančik, P. Bhattacharya, S. Chakrabarti, Y. Kang, M.E. Meyerhoff, Opt. Lett., 30, 2578 (2005).

[7] M. Lee, P.M. Fauchet, Opt. Express, 15, 4530-4535 (2007).

[8] C. Kang, C.T. Phare, Y.A. Vlasov, S. Assefa, S. M. Weiss, Opt. Express, 18(26), 27930 (2010).

[9] C-Y. Lin, X. Wang, S. Chakravarty, B-S. Lee, W-C. Lai, R.T. Chen, Appl. Phys. Lett., 97 (18), 183302 (2010)

[10] E. Waks, and J. Vuckovic, Opt. Express 13(13), 5064 (2005).

[11] S. Pal, E. Guillermain, R. Sriram, B.L. Miller, P.M. Fauchet, Biosens. and Bioelectron., 26, 4024 (2011).

[12] M.G. Scullion, A. Di Falco, T.F. Krauss, Biosens. and Bioelectron., 27, 101 (2011).

[13] D. Dorfner, T. Zabel, T. Hurlimann, N. Hauke, L. Frandsen, U. Rant, G. Abstreiter, J. Finley, Biosens. and Bioelectron., 24, 2688 (2009).

Chapter 7

[1] M. Iqbal., M.A. Gleeson, B. Spaugh, F. Tybor, W.G. Gunn, M. Hochberg, T. Baehr-Jones, R.C. Bailey, L.C. Gunn, IEEE J. Sel. Top. Quant. Electron. 16, 654 (2010).

[2] A. Densmore, M. Vachon, D.X. Xu, S. Janz, R. Ma, Y.H. Li, G. Lopinski, A. Delage, J. Lapointe, C.C. Luebbert, Q.Y. Liu, P. Cheben, J.H. Schmid, Optics Lett. 34, 3598 (2009).

[3] H. Sipova, S. Zhang, A.M. Dudley, D. Galas, K. Wang, J. Homola, Anal. Chem. 82, 10110 (2010).

[4] B.T. Cunningham, P. Li, S. Schulz, B. Lin, C. Baird, J. Gerstenmaier, C. Genick, F. Wang, E. Fine, L. Laing, J. Biomolecular Screening, 9(6), 481(2004).

[5] M. Lee, P.M. Fauchet, Opt. Express, 15, 4530 (2007).

[6] S. Zlatanovic, L.W. Mirkarimi, M.M. Sigalas, M.A. Bynum, E. Chow, K.M. Robotti, G.W. Burr, S. Esener, A. Grot, Sens.and Actuators. B, 13, 141 (2009).

[7] W-C., Lai, S. Chakravarty, X. Wang, C-Y Lin, R.T. Chen, Appl. Phys. Lett., 98 (2), 023304 (2011).

[8] W-C Lai, S. Chakravarty, Y Zou, R.T. Chen, Optics Lett. 37(8), Opt Lett, 37, 1208-1210 (2012).

[9] S. Chakravarty, J. Topoľančik, P. Bhattacharya, S. Chakrabarti, Y. Kang, M.E. Meyerhoff, Opt. Lett., 30, 2578 (2005).

[10] Y Zou, S. Chakravarty, W-C. Lai, C-Y. Lin, R.T. Chen, Lab-on-a-Chip, 12,2309-2312 (2012)

[11] R.M. Gemmill, J. Roche, V.A. Potiron, P. Nasarre, M. Mitas, C.D. Coldren, B.A. Helfrich, E. Garrrett-Mayer, P.A. Bunn, H.A. Drabkin, Cancer Lett. 300 (1), 66 (2011).

[12] Y. Takeyama, M. Sato, M. Horio, T. Hase, K. Yoshida, T. Yokoyama, H. Nakashima, N. Hashimoto, Y. Sekido, A.F. Gazdar, Cancer letters, 296, 216-224 (2010).

[13] Y. Akahane, T. Asano, B-S. Song, S. Noda, Nature, 425, 944 (2003).

[14] S. Chakravarty, Y. Zou,, W-C. Lai, R.T. Chen, Biosensors and Bioelectron, 43, 50-55 (2013)

[15] A. Subramanian, S.J. Kennel, P.I. Oden, K.B. Jacobson, J. Woodward, M.J. Doktycz, Enzyme and Microbial Technology, 24, 26 (1999).

[16] C.M. Choi, S.C. Yang, H.J. Jo, S.Y. Song, Y.J. Jeon, T.W. Jang, D.J. Kim, S.H. Jang, S.H. Yang, Y.D. Kim, Ann Oncol. (2012)

[17] M. Takenaka, T. Hanagiri, S. Shinohara, T. Kuwata, Y. Chikaishi, S. Oka, Y. Shigematsu, Y. Nagata, H. Shimokawa, M. Nakagawa, Anticancer Res, 31, 4631-4636 (2011).

[18] M. Tretiakova, A.K. Salama, T. Karrison, M.K. Ferguson, A.N. Husain, E.E. Vokes, and R. Salgia, J Environ Pathol Toxicol Oncol, 30, 341-354 (2011).

[19] M. Pesta, V. Kulda, R.Kucera, M. Pesek, J. Vrzalova, V. Liska, L. Pecen, V. Treska, J. Safranek, M. Prazakova, Anticancer Res 31, 4031-4038 (2011).

[20] H.J. Lee, Y.T. Kim, P.J. Park, Y.S. Shin, K.N. Kang, Y. Kim, C.W. Kim, J Thorac Cardiovasc Surg, 143, 421-427 (2012).

[21] B.C. Tong, D.H. Harpole, Jr.. Surg Oncol Clin N Am, 21, 161-175 (2012).

[22] T. Ohira, R.M. Gemmill, K. Ferguson, S. Kusy, J. Roche, E. Brambilla, C. Zeng, A. Baron, L. Bemis, P. Erickson, Proceedings of the National Academy of Sciences of the United States of America, 100, 10429-10434(2003).